UNIVERSITY OF CAPE TOWN
IYUNIVESITHI YASEKAPA • UNIVERSITEIT VAN KAAPSTAD

BLAST IMPACT & SURVIVABILITY RESEARCH UNIT

BISRU

The development and validation of a geometrically simplified and an accurate finite element model of the wrist joint

Yolande-Leigh Iyer

A Dissertation Submitted in Fulfilment of the Requirements for the Degree MSc (Applied Science)

Department of Mechanical Engineering
University of the Cape Town
December 2009

Abstract

The injury to the wrist joint resulting from a fall onto the outstretched hand was simulated using two models. The two validated three-dimensional wrist joint models were created using the general purpose finite element software, ABAQUS. The first model, a Geometrically Simplified half symmetry Model (GSM), was created using an approximation of real bone geometry, with material properties that could be varied. The second an Accurate Bone Geometry Model (ABGM) was created using geometry and material properties acquired from a volunteer's CT scan (Appendix D). The bones modelled in both these models were; the proximal portion of the metacarpals, the carpals and the distal portion of the radius bones. The GSM and the ABGM were development to be used to predict if a Colles' fracture (a fracture of the distal region of the radius bone) would occur if fall related loads were applied.

The models behaviour was validated at physiological loads (0-400N) by comparison of the contact stress and contact area of the radio-carpal joint with cadaveric experimental results presented in the literature. The force transmission through the radio-carpal and mid-carpal joints was also used as a validation criteria. A parametric study was undertaken for the GSM, where the effect of linear and non-linear material properties, carpal confinement methods and ligament stiffness definitions was studied. The parameters that lead to the GSM results falling within the most validation boundaries was implemented into the ABGM.

There was found to be satisfactory correlation between the location and magnitude of Contact, von Mises and Maximum principal stress between the GSM and the ABGM. The location of Maximum principal stress in both (GSM and ABGM) correlated to the region of the radius where a Colles' fracture would typically occur. Therefore know loads can be applied to the ABGM and the distribution of stress and pressure can be seen in a subject's actual bone geometry and material property distribution. The GSM however can be used in cases where a CT scan is unattainable and the overall material properties

of the subjects joint are known, allowing the prediction of the magnitude of maximum stress within the joint, for a given set of material properties.

Declaration

I, Yolande-Leigh Iyer, hereby:

(a)Grant the University free licence to reproduce this dissertation, entitled "The development and validation of both a geometrically simplified and an accurate finite element models of the wrist joint" , in whole or in part, for the purpose of research ;

(b)Declare that this dissertation contains my own work, except where reference and acknowlegdement is made to contributions by others. I declare that this material has not been submitted for any other purpose or examination to any other Department or University.

Yolande-Leigh Iyer

December 2009

Acknowledgements

I would like to thank the following for their contributions thereby ensuring the successful completion of my thesis:

- Professor G.N. Nurick who supervised the thesis - for his guidance and support both academically and financially.
- Blast Impact Survivability Research Unit (BISRU) and the Department of Mechanical Engineering for the use of their facilities.
- The members of BISRU for providing an enjoyable and stimulating work enviroment.
- My family, Logan, Saras, Cheri-lee, Geraint, Marlene, Viloshni, Clinton, Gregory and my Grandmother for their constant support.
- My friends and office mates; Viloshni, Natasha, Sankeshan, Abhi, Carlo, Andrew and Patrick for helping throughout this year.

Contents

List of Figures

List of Tables

Nomenclature

E	Young's Modulus
G	Shear Modulus
HU	Hounsfield units
ε	Normal strain
ρ	Apparent density
μ	Friction coeficient
σ	Normal stress
W	Mooney-Rivlin strain energy potential
C_1	Mooney-Rivlin constant
C_2	Mooney-Rivlin constant
D_1	Mooney-Rivlin material incompressibility constant
f	force
ε_{ref}	Reference strain
a, b	Ligament stress-strain definition constants
k	Stiffness
l_o	Original length
l	Length
P	Contact Pressure
h	Clearance
P_o	Pressure at zero clearance
h_o	Clearance at zero pressure
τ_{crit}	Critical shear stress
Δx	Change in length
A	Area
ν	Poisson's ratio
K_{equ}	Equivalent spring stiffness

τ	Shear stress
σ_c	Cauchy stress tensor
σ_m	von Mises stress
σ_x, σ_y, σ_z	Principal stress
σ_H	Hydrostatic stress

Abbreviations

CT	Computer Tomography
RBSM	Rigid Body Spring Model
MRI	Magnetic Resonance Imaging
FEM	Finite Element Model
GSM	Geometrically Simplified Model
ABGM	Accurate Bone Geometry Model
S	Scaphoid
L	Lunate
Mc	Metacarpal

Units

N	Newton
m	Meter
mm	Millimeter
sec	Second
kg	Kilogram
Pa	Pascal
MPa	MegaPascal

Chapter 1

Introduction

The forearm and hand give humans the defining ability to manipulate the environment. These appendages are necessary for vital daily activities. When a person falls, reflex reactions cause them to make instinctive use of their hands to protect the body and head from injury. In the process they are often subject to injurious forces, therefore inhibiting their use for necessary activities.

Figure 1.1: Bones of the hand and wrist [1].

Fracture of the radius bone has been found statistically to be the most common injury, after a fall onto an outstretched hand. This has been found to be the case in children [2, 3, 4], the elderly [5, 6, 7, 8] and during sport [2, 9, 10]. Radius fractures following falls have also linked to a decreased bone mineral density in Osteoporotic women [5, 7]and young girls [2, 4]. The radius is attached to the hand through the wrist joint (figure 1.1). The wrist joint is composed of two joints; the mid-carpal and the radio-carpal. The bones involved are the radius, the ulna, the carpals and metacarpals. This study, aimed to create a validated finite element model of the wrist joint. This model was developed to simulate the force transmission to the radius bone and give insight into the contact stress distributions within the wrist joint.

The forces applied to the hand and wrist have been studied experimentally by having subjects fall onto force plates [11, 12, 13, 14, 15, 16]. Such studies have been conducted to determine possible preventative methods to decrease the load applied to the wrist during a fall. These studies can only be used to simulate falls that do not cause injury. Injury causing loads have to be studied using cadaveric specimens. The fracture load of individual cadaveric radius bones has been studied through compression testing [17]. The pressure and force transfer through the wrist joint has also been studied through various loading methods of cadaveric wrist joints [18, 19, 20, 21]. Various loading conditions cannot be studied in these manners without the use of numerous cadaver arms. Therefore mathematical models (Finite Element [22, 23, 24, 25, 26, 27, 28, 29] and Rigid Body Spring Models [11, 14, 30, 31, 32, 33, 34]) are used to simulate these various loading conditions and to study the effect of injurious loading conditions [26, 35, 36, 37]. None of the previous 3-d Finite Element models involved simulating the load transmission pathway from the metacarpals to the radius, for simulating the injuries occurring after a fall onto the outstretched hand.

This work entailed the creation of two Finite Element models of the wrist joint. The first model was created from the geometric approximation of the bones of the wrist. The material properties of this model can be varied, therefore enabling the simulation of different subject's material properties for each material modelled or to investigate the effects of a diminished bone mineral density on radius fracture. The simplicity and short run time of this model allowed it to be used to conduct a parametric study investigating the effects of varying the material property parameters and the effect of various carpal bone movement constraint methods on the outputs. The model was validated by a qualitative and quantitative comparison with various cadaveric experimental and Rigid Body Spring Model results in the literature. A geometrically accurate bone model was created, using

the modelling parameters that caused the geometrically simplified model to best simulate the experimental work. This geometrically accurate model's bone geometry and material properties were attained from a volunteer's CT scan (Appendix D). Therefore enabling these modelling parameters to be used for a volunteer's case study.

The objectives of this thesis were therefore to:

1. Conduct research into the anatomy of the wrist joint.
2. Research data relating to the material properties of the biological tissue, present within and making up the joint.
3. Research data relating to hand and wrist injures during fall events and experimental work relating to the wrist joint loading conditions. This experimental data was used as a verification method for the Finite Element model.
4. A geometrically simplified model was developed to study the effect of different bone constraint methods and material property definitions on the result.
5. This model was validated by loading it under known conditions of forces and comparing the results to the known results from experimental work. The carpal motion constraint methods that yield the results closest to the validation experiment results were chosen.
6. Accurate bone geometry and material properties were obtained from a volunteer's CT-scan (Appendix D) and implemented into the geometrically simplified model with parameters that best fit the known experimental work.
7. The results of these simulations were analysed to see if both models results fell within the validation result boundaries.
8. Conclusions were drawn for the analysis work and recommendations were made.

Chapter 2

Literature Review

This study involves simulating the injury that occurs to the wrist joint during a fall onto the outstretched hand, using two Finite Element models of the wrist joint. The literature review begins with definitions of anatomical terms, followed by an overview of the anatomy of the hand and forearm. Fall related statistics and previous biomechanical models are then discussed. The final section contains details of material properties of the materials used within the model development and the final model.

2.1 Anatomical terms

The standard anatomical position, by which anatomical terms are defined, is shown in figure 2.1. The positions are defined along the three major planes [38]:

1. **Frontal**, observing the body from the front.
2. **Sagittal**, observing the body from the side.
3. **Transverse**, observing the body from directly above the head.

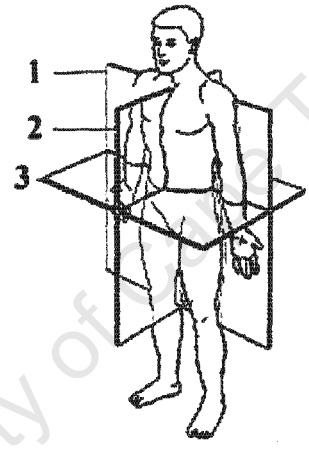

Figure 2.1: The standard anatomical position [38].

Other anatomical terms include:

- **Distal**, toward the finger.
- **Proximal**, toward the attachment of the limb.
- **Medial**, toward the midline of the body.
- **Lateral**, away from the midline of the body.

2.2 Bones of the wrist

The human hand has twenty seven bones as shown in figure 2.2. The *radius* (number 1 in the diagram) and the *ulna* (2) are forearm bones and are joined to the hand via the wrist joint [39, 40]. The bones of the hand are divided into three groups; eight *carpal* bones (3-10) in the wrist, five *metacarpal* bones (11) and fourteen *phalanges* (12-14) of the fingers. The metacarpal bones were defined as follows:

A metacarpal 1 or thumb

B metacarpal 2 or index

C metacarpal 3 or middle

D metacarpal 4 or ring

E metacarpal 5 or pinky

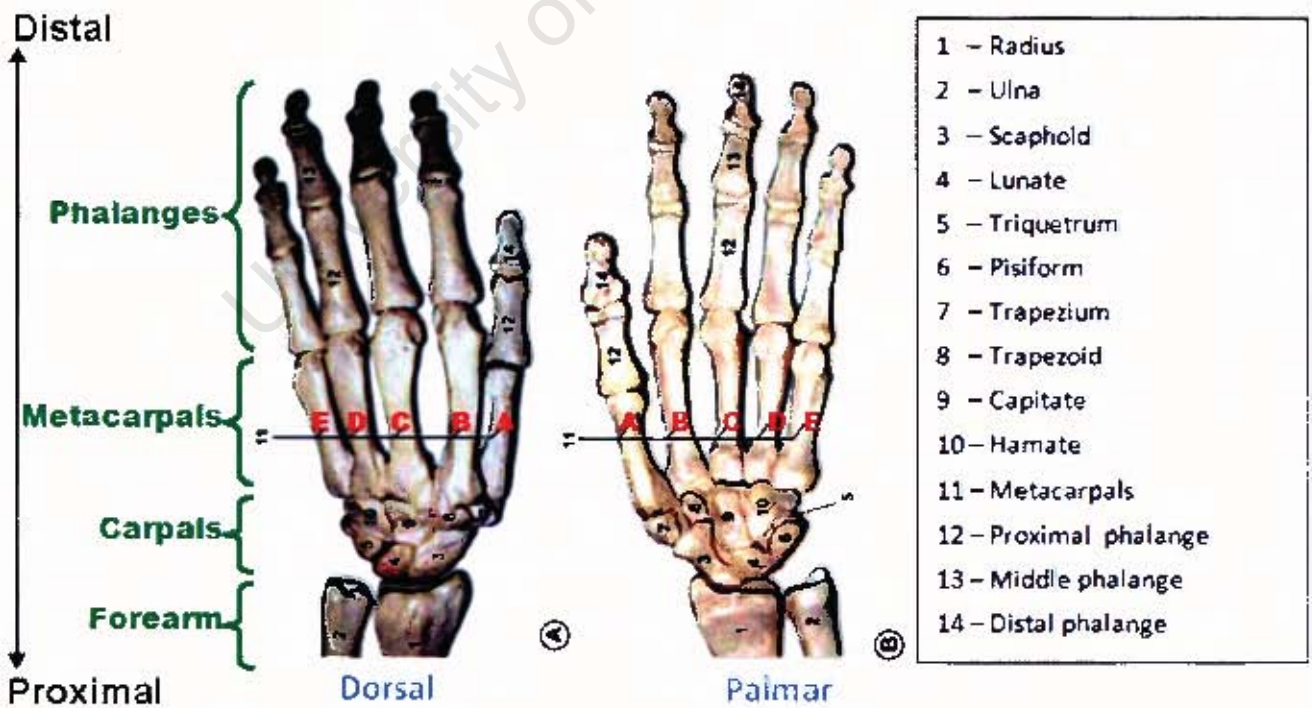

Figure 2.2: Bones of the hand and wrist [41].

The carpal bones are arranged in two rows; the distal row, number 7-10 in the figure 2.2, and the proximal row, number 3-6. The bones of the distal row, from the lateral side to the medial side are; the *trapezium, trapezoid, capitate and hamate.* The bones of the proximal carpal row are; *scaphoid, lunate, triquetrum and pisiform.* The hand has two surfaces; the dorsal (A) and the volar or palmar surface (B). The dorsal surface is the back of the hand and the palmar surface is the palm or grasping side of the hand.

The phalanges bones make up the fingers of the hand. There are three types of phalanges, namely the *proximal* (12), *middle* (13) and *distal* (14) phalanges. Fingers are composed of three phalanges; the proximal, middle and distal phalange. The thumb contains only two phalanges, namely the proximal and distal phalange.

The carpus

The carpus is composed of the carpal bones. The carpus connects the bones of the forearm with the metacarpals. These bone to bone connections occur via articular joints, which are discussed in more detail in section 2.3.1. The connection between the metacarpals and the distal carpal row is known as the carpo-metacarpal joint. The one between the distal and proximal carpal rows is the mid-carpal joint. The final joint is the radio-carpal joint. These joints make up the wrist joint, discussed in more detail in section 2.3.1.

The carpus is not entirely rigid because each of the eight bones has different degrees of movement. There are two groups of bones in the hand. The fixed group and the mobile group. The fixed group is comprised of the distal row of carpal bones, the second and third metacarpals bones. The joints between these bones are capable of limited movement. The mobile group is made up of the phalanges, the thumb and fifth metacarpal. These two groups work together to allow the hand to close [39]. Therefore, the distal carpal row is semi-rigid and the proximal carpal row is semi-mobile [42].

Carpal bones share common characteristics, with the exception of the pisiform. The pisiform bone is a sesamoid bone that lies within the flexor carpi ulnaris tendon [43]. Each of the other carpal bones has six surfaces (figure 2.4). Of these six surfaces four of them are articular. These are the proximal, distal, medial and lateral articular surfaces. The proximal surfaces are convex and the distal surfaces are concave. The properties of the carpal bones are summarised in table 2.1. The remaining two surfaces, the volar and palmar surfaces are ligament attachment sights. These surfaces (tubercles) are rough in

texture in order to give ligaments a larger surface area for attachment. Carpal bones are all short bones [44], further discussed in section 2.9.1.

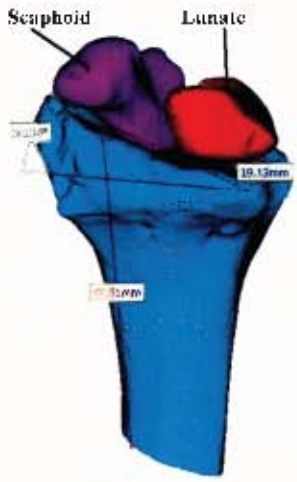

Figure 2.3: The distal portion of the radius, scaphoid and lunate derived from a volunteer's CT-scan (Appendix D).

The scaphoid and lunate make up the articular surface of the carpal row and the radius. The distal articular surface of the radius has a double obliquity, 12-15 degrees in the lateral view and 15-20 degrees in the anteroposterior view [39]. These geometry angles of the radius can be seen in figure 2.3 from bones extracted from a volunteer's CT scan (Appendix D) during this study.

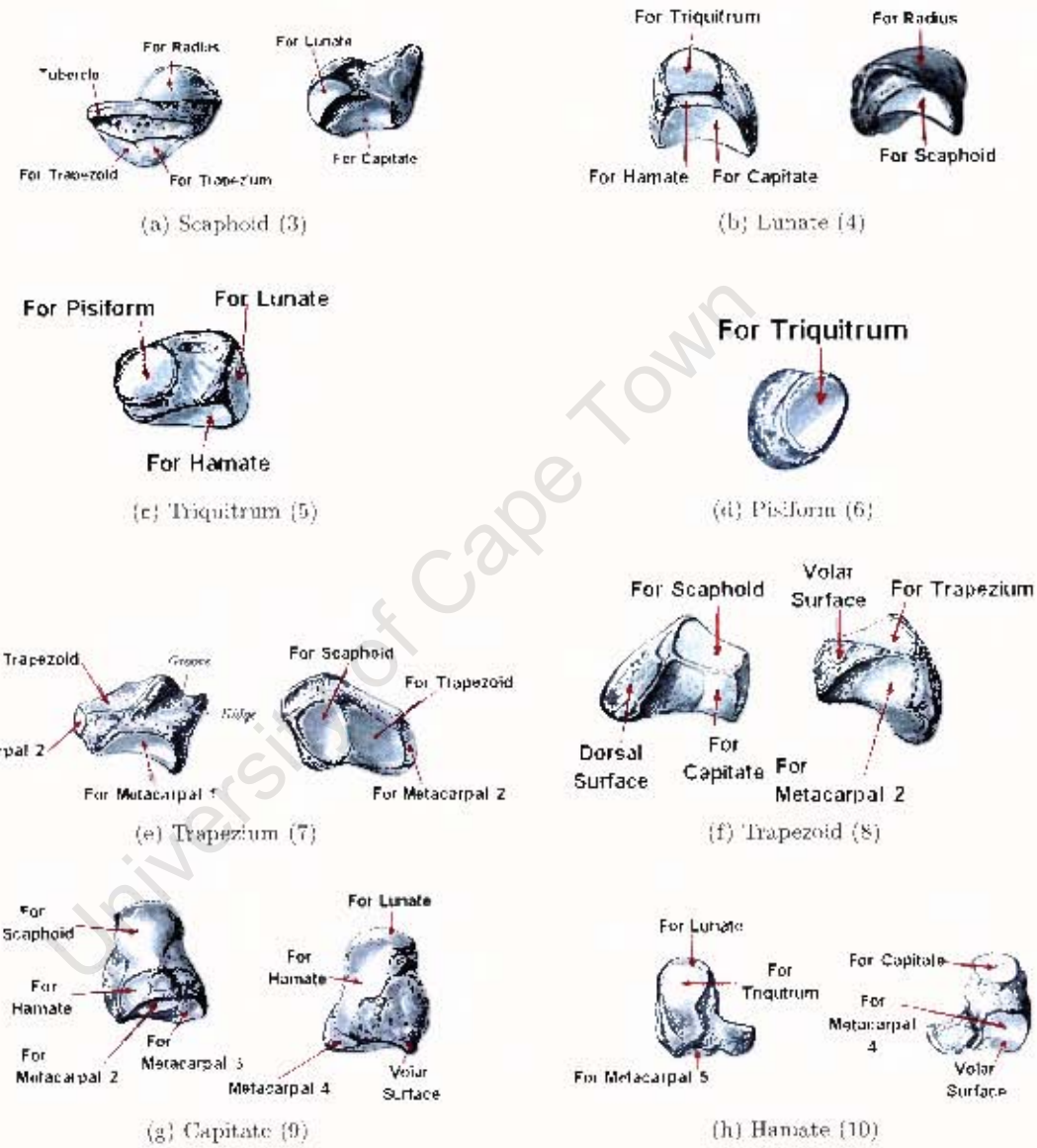

Figure 2.4: Articular surfaces of the carpal bones of the left hand [43]. The number corresponding to their position in figure 2.2 is included in brackets.

Bone	Shape	Articulations					Number in Figure 2.4 & 2.2
		Proximal	Distal	Lateral	Medial	Other	
Proximal carpal row							
Scaphoid	Boat	Radius	Trapezium &trapezoid	- -	Capitate & lunate	-	3
Lunate	Crescent	Radius	Capitate &hamate	Scaphoid	Triquetrum	-	4
Triquetrum	Pyramid	Hamate	-	Lunate	-	Anteriorly pisiform	5
Pisiform	Small & oval	-	-	-	-	Posteriorly triquetrum	6
Distal carpal row							
Trapezium	-	Scaphoid	Metacarpal 1	- -	Trapezoid & metacarpal 2	-	7
Trapezoid	Wedge	Scaphoid	Metacarpal 2	Trapezium	Capitate	-	8
Capitate	Largest carpal	Scaphoid & lunate	Metacarpals 2, 3, 4	Hamate	Trapezoid	-	9
Hamate	Wedge	Lunate	Metacarpals 4,5	Triquetrum & capitate	-	-	10

Table 2.1: Summary of carpal bone properties.

The forearm

The bones that make up the forearm are the radius and the ulna, as shown in figure 2.2 and in more detail in figure 2.6. Both bones are long bones [45, 44]. The ulna lies on the medial side of the forearm (closest to the body) and the radius lies on the lateral side. The distal end of the ulna articulates with the radius via the ulna notch. The proximal end articulates with humerus at the elbow joint [38].

The radius is larger than the ulna in length and size. It articulates proximally with the humerus at the elbow joint and distally with the scaphoid, lunate and ulna, as shown in figure 2.2 and 2.5. Therefore, making it the main load-bearing bone of the forearm and the ulna to function mainly for muscular attachment [43].

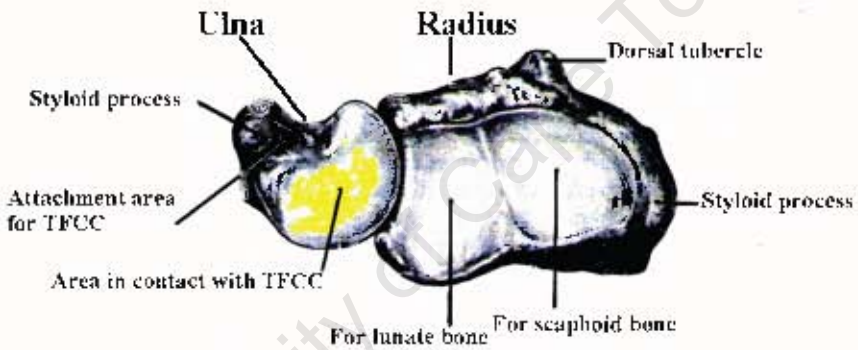

Figure 2.5: The distal articular surfaces of the radius and ulna [43].

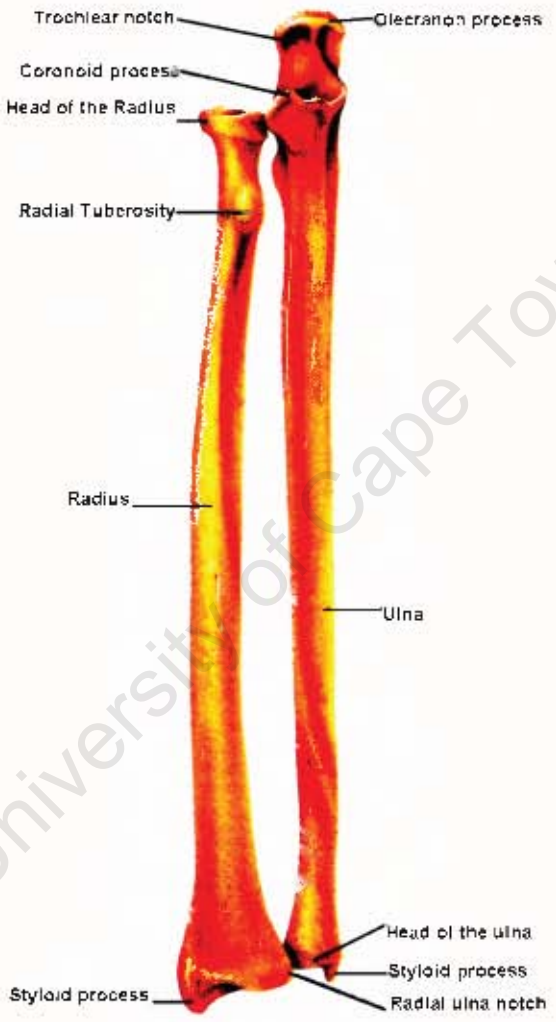

Figure 2.6: The radius and ulna of the right forearm [38].

2.3 The motor mechanics of the hand

The hand and wrist are controlled and moved by muscle exertion. This muscle force is transmitted through the transmission system of the hand and wrist; namely the joints, the bones and tendons. Any external force that is applied to the hand and wrist is also transmitted through this transmission system. The bones of the hand and forearm involved in this transmission system have been discussed already (section 2.2). A description of the joints and tendons will be given in the following section.

2.3.1 Joints of the hand and wrist

Joints occur at the point where two bones or a bone and cartilage come into contact. There are three types of joints present in a human body. These joints are [40]:

1. **Fibrous joints** do not permit any movement. They have no joint cavity and are connected by fibrous connective tissue. Examples of these are the joints between the bones of the skull.
2. **Cartilaginous joints** have no joint cavity and are connected with cartilage. They allow minimal movement. This type of joint is present between the vertebrae.
3. **Synovial joints** allow movement. They are surrounded by an articular capsule, containing synovial fluid. The synovial fluid lubricates the joints during movement.

Synovial joints are the most common type of joint in the body [43]. The movements permitted by these joints are:

Flexion involves increasing the joint angle.

Extension involves deceasing the joint angle.

Abduction involves movement away from the body centerline.

Adduction involves movement toward the body centerline.

Rotation is the movement around an axis.

Circumduction is a 360^0 rotation.

There are many types of synovial joints that exist in the human body. Simplified diagrams of these joints are shown in figure 2.7. These joints are [46]:

Ball and socket joint the bone that lies distally in the joint can move around in an indefinite number of axes. Main movements are flexion-extension, adduction-abduction, axial rotation and circumduction. An example of this type of joint is the hip joint.

Condyloid joint the bone that lies distally in the joint has an oval articular surface and is received into an elliptical cavity, this makes it impossible for these bones to rotate around their axes. So main movements here are flexion-extension, adduction-abduction and circumduction. An example of this type of joint is between the radius and carpal bones.

Hinge joint the distal bone can move only in one plane. Only flexion and extension movements are allowed. An example of such a joint is the elbow joint.

Flat joint have articulating surfaces that are almost flat. They can only undergo movement in one direction, i.e. flexion-extension movement. An example of such a joint is the carpo-metacarpal joint between the carpals and the metacarpals.

Saddle joint consists of two opposing surfaces that are reciprocally concave-convex. The movements allowed are flexion, extension, adduction, abduction and circumduction. But no rotations of the bones along their axes can occur, the carpo-metacarpal joint of the thumb is one such example.

Pivot joint these joints only allow rotation. An example of such a joint is the joint that allows the head to be rotated on the neck.

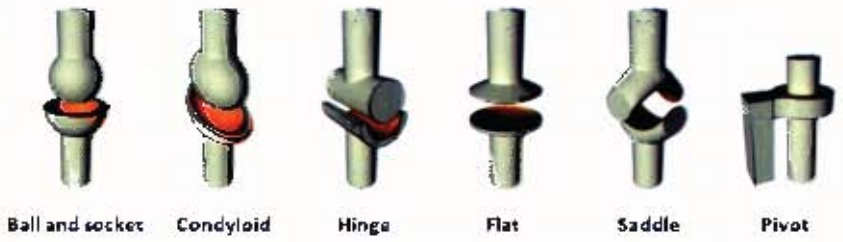

Figure 2.7: Simplified diagrams showing the classification of joints of the body [46].

Wrist Joint

The overall motion of the wrist is a result of numerous bone interactions. The numerous bone interactions (figure 2.8) are made up of; interactions between individual carpal bones, distal interactions of carpal bones with the bases of the metacarpals, proximal interactions between carpal bones and the articular surface of the radius and TFCC. Therefore, the wrist joint is composed of three synovial joints; the distal radio-ulna joint, the radio-carpal joint and the mid-carpal joint.

The **radio-carpal joint** is a condyloid joint [46]. It is the articulation between the proximal surfaces of the scaphoid, lunate and triquetrum bones and the distal articular surface of the radius and an articular fibrocartilage disk. This fibrocartilage disc is called the *triangular fibrocartilage complex (TFCC)*. The joint is shown in figure 2.8. The proximal articulating surfaces form a biconvex surface that articulates with the biconcave distal articular surface [43]. The TFCC forms a quarter of the joints articular surface [44], as seen in figure 2.9. The proximal carpal row therefore does not contact the head of the ulna directly, but rather through the TFCC. Therefore, the ulna head does not directly affect the stability of the wrist [42].

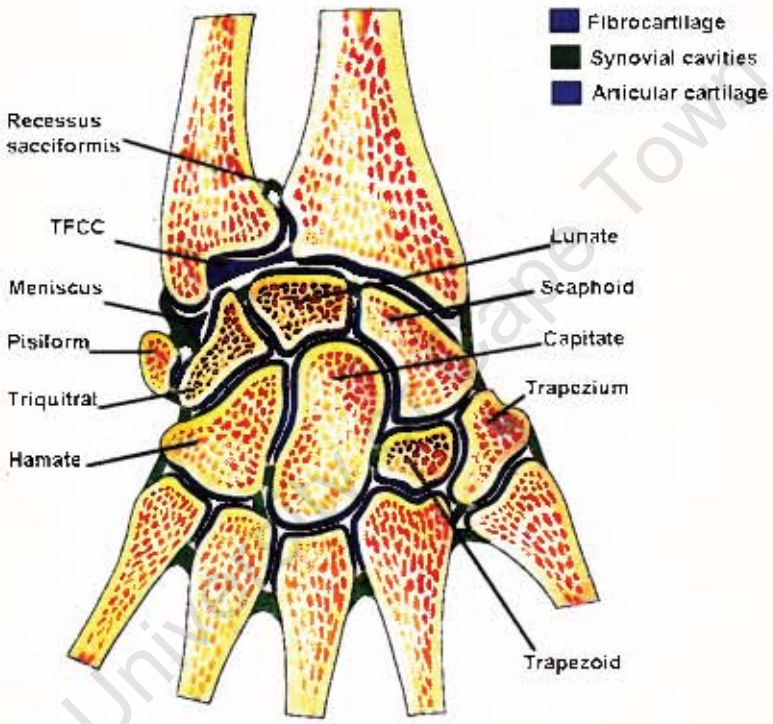

Figure 2.8: Cross section through the wrist [43].

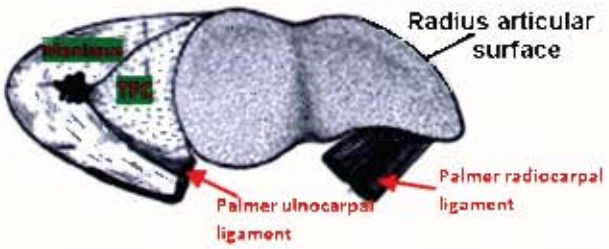

Figure 2.9: The proximal articular surface of the radio-carpal joint [44].

The mid-carpal joint occurs between the proximal and distal carpal rows, shown in figure 2.8. It is a ball and socket joint [46]. The bones of the distal carpal row tend to act as a functional unit due to the dense ligamentous connections, thereby only allowing for minimal joint movement [18].

The distal radio-ulna joint is a pivot joint that is made up of the convex distal articular surface of the ulna and the concave sigmoid notch of the radius [46]. The joint is separated from the wrist by the TFCC. This joint facilities pronation and supination of the forearm.

Movements of the wrist joint

Movements of the wrist joint , shown in figure 2.10 are defined as [46], [44]:

In the sagittal plane

Flexion bending the palm upwards or closer to the forearm.

Extension is bending the palm back or away from the forearm.

In the frontal plane

Radial deviation or abduction is moving the hand away from the trunk and closer to the radius bone of the forearm.

Ulna deviation or adduction is moving the hand closer to the trunk and closer to the ulna in the forearm.

Movement in the forearm is caused by the radius and ulna rotating with respect to each other along the long axis, these movements are:

Supination is rotation of the forearm in the palm up position.

Pronation is rotation to the palm down position.

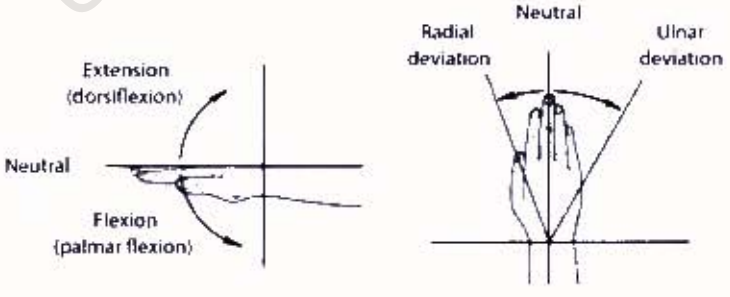

Figure 2.10: Movements of the wrist joint [47].

2.3.2 The tendons of the hand

The tendons attach the muscles to the bones, transmitting the muscle forces to the bones which allows for hand and wrist movement. The tendons are surrounded by the *bursae* and the *tendon sheaths* allowing them to move in a frictionless environment [43].

Flexor tendons of the hand and wrist

The carpal tunnel is found on the palmar side of the hand and it houses the flexor tendons [39]. These tendons allow the digits and the thumb to flex and the wrist to flex, abduct and adduct. There are nine of these tendons, the four Flexor digitorum superficialis tendons, the four Flexor digitorum profundus tendons and the Flexor pollicis longus [44].

Extensor tendons of the hand and wrist

The twelve extensor tendons pass through the wrist and are on the dorsal side of the hand [44]. They allow the digits and the wrist to extend and the thumb to extend and abduct. These tendons pass smoothly through six compartments, similar to the carpal tunnel.

The first compartment houses the Abductor pollicis longus and the Extensor pollicis brevis that control the thumb. The second compartment contains the Extensor carpi radialis brevis and the Extensor carpi radialis longus that allows for wrist extension. The third compartment contains the Extensor pollicis longus that controls the extension of the thumb. The fourth compartment contains the Extensor digitorum that extends the digits and the Extensor indicis that extends the thumb. The fifth compartment contains the Extensor digiti minimi that controls the extension of the little finger. The sixth compartment contains the Extensor carpi ulnaris that controls wrist extension [45].

2.3.3 Ligaments of the wrist

Ligaments connect bones[47]. The composition of ligaments are further discussed in section 2.9.4. The wrist joint is surrounded by a capsule that is strengthened by ligaments. The capsule is lined with a synovial membrane, shown in figure 2.8. This synovial membrane extends from the distal end of the radius and the articular disk to the articular surfaces of the proximal carpal bones. Ligaments of the wrist can be defined on the basis of the course that they transverse or their origin and insertion points [45].

The classification of the ligaments based on the course they transverse is:

- **Interosseous ligaments** travel deeply in a transverse course.
- **V-ligaments** travel superficially in oblique courses.

The classification of ligaments based on their origin and insertion points is described below and summarised in figure 2.11 and table 2.2:

- **Extrinsic** ligaments originate from the radius, ulna or metacarpal bones and insert onto one or more carpal bones. They are classified into proximal or radio-carpal and distal ligaments.
- **Intrinsic** ligaments originate and insert onto the carpus. They are grouped into three groups based on their length. These groups are; short, long and intermediate ligaments [42].The short ligaments bind the bones of the distal carpal row into a single functional unit.

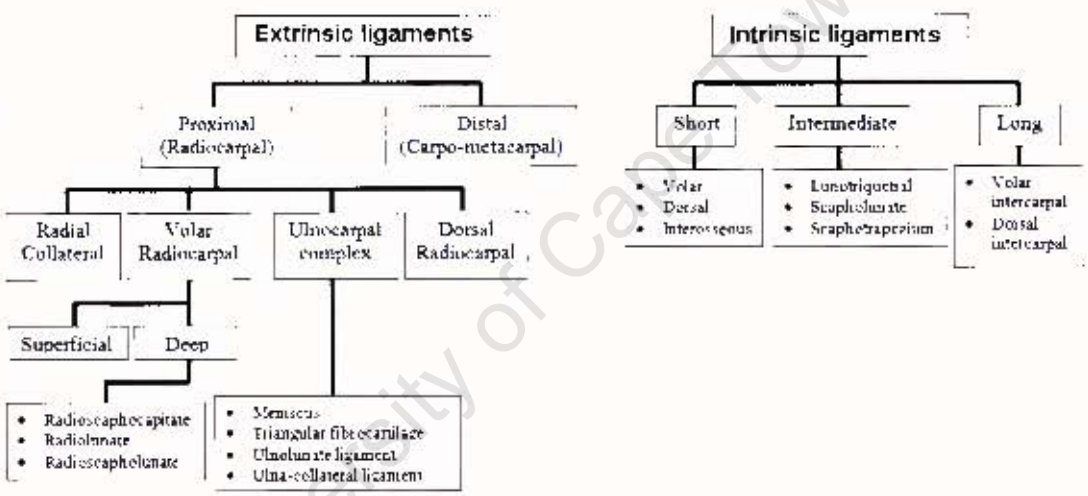

Figure 2.11: Classification of wrist ligaments

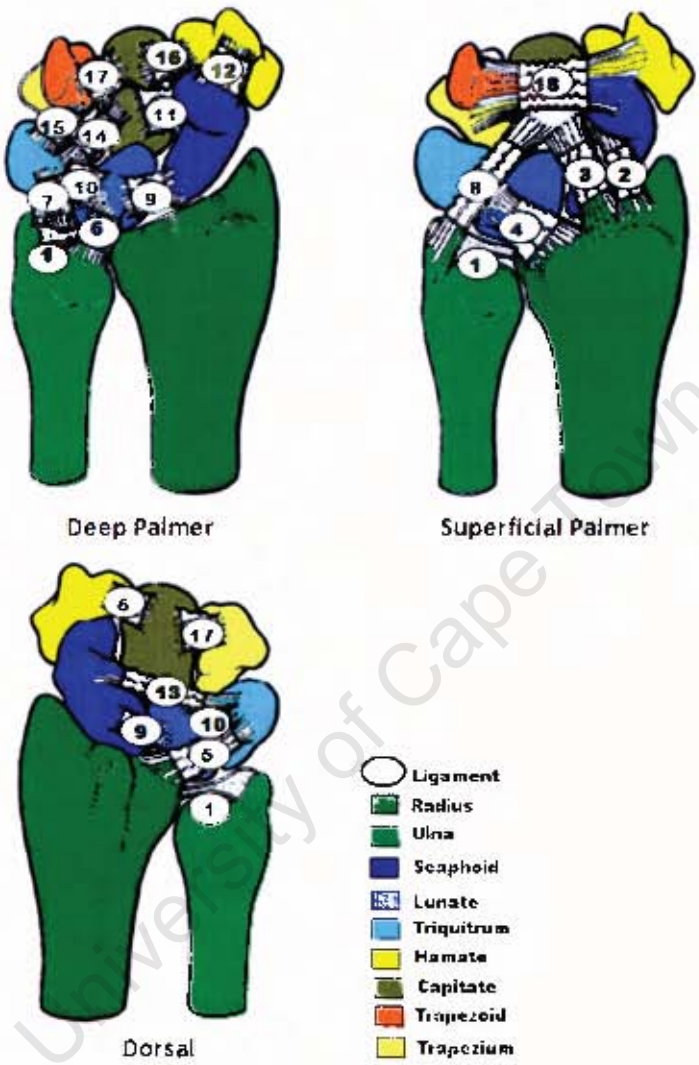

Figure 2.12: Schematic showing ligaments of the wrist [32].

Number (figure 2.12)	Ligament	Attachment	Stabilizing function
1	Distal Radio-ulna	Radius-Ulna	Distal radio-ulna joint
2	Radial collateral	Radius-Scaphoid	Radio-carpal joint
3	Radio-capitate	Radius-Capitate	
4	Short Radio-lunate	Radius-Lunate	Lunate
5	Radio-triquetral	Radius-Triquetrum	Radio-carpal joint
6	Ulno-lunate	Ulna-Lunate	Lunate
7	Ulna-triquetral	Ulna-Triquetrum	Ulnocarpal compartment
8	Ulno-capitate	Ulna-Capitate	
9	Scapo-lunate	Scaphoid-Lunate	Stabiliser proximal carpal row
10	Luno-triquetral	Lunate-Triquetrum	Proximal carpal row
11	Radial Arcuate	Scaphoid-Capitate	Mid-carpal joint
12	Scapho-trapezium	Scaphoid-Trapezium	Distal pole of scaphoid
13	Scapho-triquetral	Scaphoid-Triquetrum	
14	Ulna Arcuate	Capitate-Triquetrum	Mid-carpal joint
15	Hamate-triquetral	Hamate-Triquetrum	Mid-carpal joint
16	Capitate-Trapezoid	Capitate-Trapezoid	Distal carpal row
17	Hamate-capitate	Hamate-Capitate	Stabiliser of distal carpal row
18	Flexor retinaculum	Scaphoid & Trapezium -Hamate & Triquetrum	Tunnel for flexor tendons

Table 2.2: The ligaments of the wrist and their functions [42].

Functions of wrist joint ligaments

A summary of the stabilising function of wrist ligaments is given in table 2.2. Anther function that the wrist joint ligaments play a role in, is the aiding of joint movement. During wrist joint extension, the palmar ligaments (Radio-luno-triquetral and the Radio-capitate) are stretched. The Radio-capitate ligament crosses the neck of the scaphoid and consequently causes simultaneous extension of the scaphoid and the capitate. This effect is carried through the Scapho-lunate ligaments and the lunate extends so that the capitate and lunate are coaxial in extension. The extension of the scaphoid bone ends before the lunate bone ends [39]. During wrist joint flexion, the dorsal ligaments are stretched and the triquetrum is moved towards the radial articular surface of the hamate.

2.4 Epidemiology of fall-related injuries

The wrist joint models in this study were created due to the high incidence of wrist injuries that follow a fall onto the outstretched hand. 15% of injuries brought into emergency departments are fall related [9]. There are three fall scenarios where these injuries are most prevalent. These are falls that occur in the; elderly [5, 6], children [2, 3, 4] and during sporting activities [9, 2, 10].

The data presented in this section focuses on what type and how fall related injuries occur and why they occur across these various demographic groups. Fall direction and impact site are important factors that affect injury risk and type. Forward falls have been found to be the most common type; 60% forward, 20% side and 20% backward falls (figure 2.13). Sideways falls are associated with hip injuries and forward falls are associated with upper-extremity injuries because the upper limbs are used to protect the head and torso.

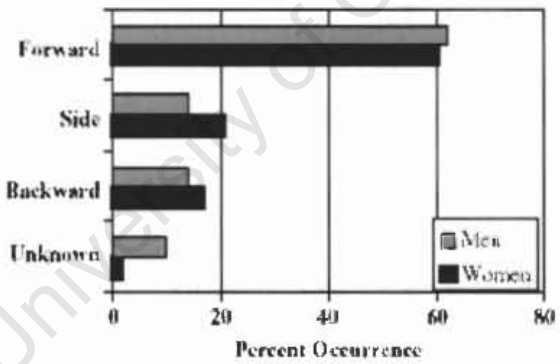

Figure 2.13: Graph showing the occurrence of falls in different fall directions [6].

The body parts receiving the main impact in order of frequency is; the hand and arm, the buttocks, the head and finally the knee (figure 2.14). Injuries to the forearm and hand are mainly soft tissue damage and fractures of carpal bones and/or the radius or ulna [6, 9]. Wrist injuries have the highest frequency of all hand and forearm injuries [9]. These injuries are most prevalent in the dominant hand, particulary during summer and winter months [5]. This is due to an increase in outdoor activities during summer and falls on slippery paths during winter.

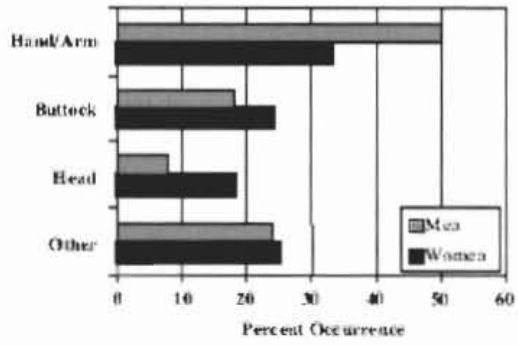

Figure 2.14: Graph showing occurrence of injuries in different body parts after a fall [6].

2.4.1 Falls in the adults

Distal radius fractures have been found to have highest incidence rate of 17.5% of all fractures occurring in the elderly [7]. Distal radius fractures can be either extra articulator or intra-articular. The most common type of extra-articular fracture is known as a Colles' fracture, more details of this fracture are given in section 2.8.3. Extra-articular fractures were found in 73% of all the distal radius fractures studied whilst the intra-articular fractures occurred in 27% of the cases studied. 98% of fractures occurred after a minor fall: 73.5% from standing height and 24.5% from greater than standing height [8].

Interestingly, there is continuous rise in the incidence of distal radius fractures in women over the age of 50 and men over 65, as seen in figure 2.15 [5]. This coincides with the period where women undergo menopause and the incidence of Osteoporosis increases. Details about Osteoporosis are given in section 2.8.2. Osteoporotic fractures mainly occur in the spine, the proximal femur, the proximal humerus and the distal radius. 70% of inpatient fractures are potentially osteoporotic [7]. Additionally, the annual incidence of Colles fracture in pre-menopausal women are 10 per every 10000 population, whilst in post-menopausal women are 120 per every 10000. In comparison, injuries increase annually in men over 65 from 10 per every 10000 to 33 per every 10000 over age 85 years [5]. Therefore, it can be concluded that a fracture to the distal radius that usually follows a fall onto the outstretched arm is related to osteoporosis in post-menopausal women.

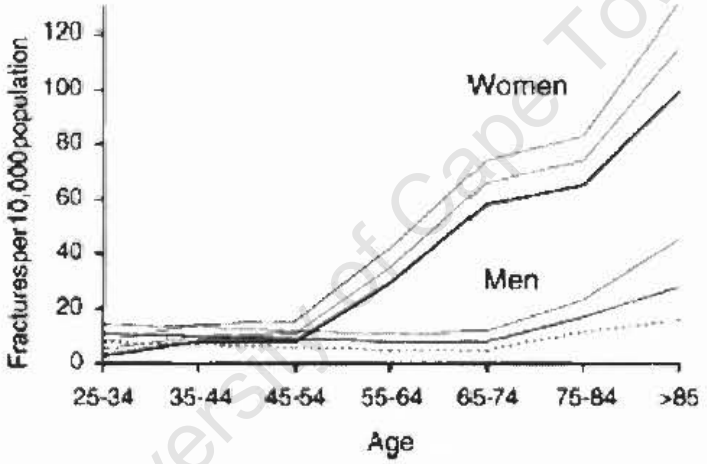

Figure 2.15: The incidence of distal radius fracture in men and women per 10000 population per year and 95% confidence intervals [5].

2.4.2 Falls in children

According to the Red Cross Children's Hospital, falls are the leading cause of injury in children under the age of 14 (figure 2.16) [3]. 36% of injuries occurring in children, were from falls during play; i.e. ball games, falls from trees and slides or sport. 8% of all fractures occurred in the wrist. Of these wrist fractures, 29% were a complete fracture of the distal end of the forearm, 9% included both the radius and the ulna and 4% were Colles' fractures [2].

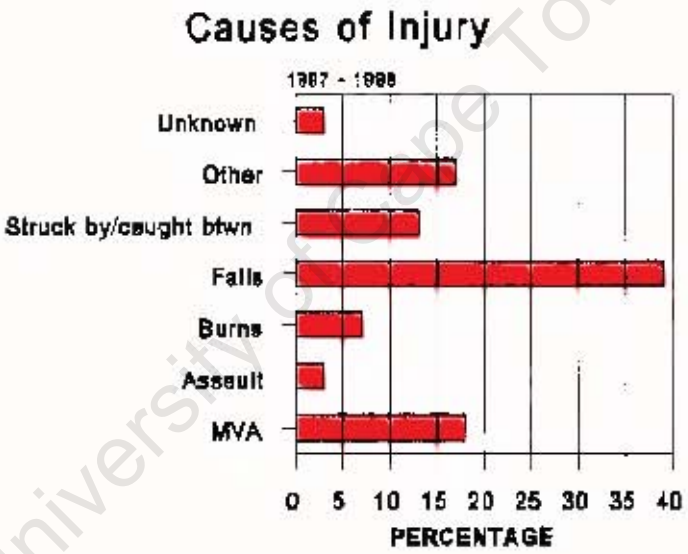

Figure 2.16: Causes of injuries in children [3].

Forearm fractures tend to happen at the age that the maximum growth spurt takes place due to poorer than normal bone mineral density. These peak ages are 10-12 years for girls and 12-14 years for boys [2]. A further study was conducted to determine if this was indeed the case for girls between the age of 3-15 years. It was found that 57% of injuries occurred from falls directly onto the hand or wrist, often resulting from a low bone density [4].

2.4.3 Falls during sport

Falls during sport result in a large amount of hand and wrist injuries. 21% of fractures to the distal radius, in people under the age of 20, occurred during winter sports such as sledding, ice skating, ice hockey, skiing [2]. Sport injuries account for 15% of hand and wrist injuries in Ireland [9]. A wrist fracture occurs once every 1135 days for a snowboarder. 25% of all snowboard injuries affect the wrist joint and 70% of all wrist injuries were fractures [10].

2.5 Forces applied to the body during a fall

From the statistics presented in the previous section (section 2.4), the upper extremities are used to manage fall events. They are used to reduce the risk of injury to the head or torso, by protecting the head and thorax from impact related injury by diminishing or even arresting the momentum acquired by the body during the decent to the ground. By carrying out this function, the upper extremity must absorb the potentially injurious impact loads.

There are two forces to consider when looking at the risk of fracture during a fall. The first force is the force applied to the body when an outreached hand strikes an object or surface. The resultant force applied to a body is made up of peak compressive forces and a bending force. The second force is that force which is needed to fracture a bone.

The forces applied to the body during a fall event can be measured experimentally [11, 12, 13, 14, 15, 16] or using mathematical models [11, 30, 31, 14]. Experimental work using live subjects is used to study cases where lessened potentially injurious loading is applied. Mathematical models can be validated by these results. These mathematical models can be loaded with potentially injurious loads.

The pressures transmitted through the wrist joint can also be measured both experimentally [18, 19, 20, 21] and by mathematical models [32, 33, 34].

2.5.1 Experimental work

Fall experiments involve the physical simulation of falling as well as the measurement of the impact load and three-dimensional motions of the body. The first study carried out in an attempt to quantify the forces and energies applied to the upper body during a fall was by Chiu and Robonovitch in 1998 [11]. This study used both experimental and mathematical models (discussed in section 2.5.2) to characterise the impact response of the body.

The experimental work was carried out on both male and female participants between the ages of 20 and 35 years. The fall scenario used (figureure 2.17) was used to simulate the worst case falling scenario. It involved a forward-directed fall, where ground contact occurred with the knees and a single outstretched hand with a a fully flexed elbow. The

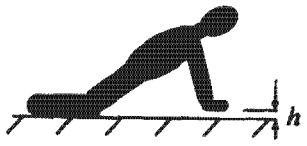

Figure 2.17: Fall scenario schematic, where h is the decent height [11].

reason that the knees are the first body part to make contact with the ground is so that the shins and feet equal zero velocity when the hands make contact. For the experimental work, low heights of 0-5cm were used so as not to cause injury to the subjects.

Figure 2.18 shows a typical force-time profile achieved in the experiment. In the general case contact forces are found to be characterised by a high frequency peak (F_{max1}) occurring approximately 20ms after impact and a lower frequency oscillation (F_{max2}) occurring approximately 110ms after impact. The peak forces for these falls ranged from 400-1000N. These results show that in some falls the forces exerted on the upper extremity are greater than the weight of an average person ($\simeq$ 65Kg's).

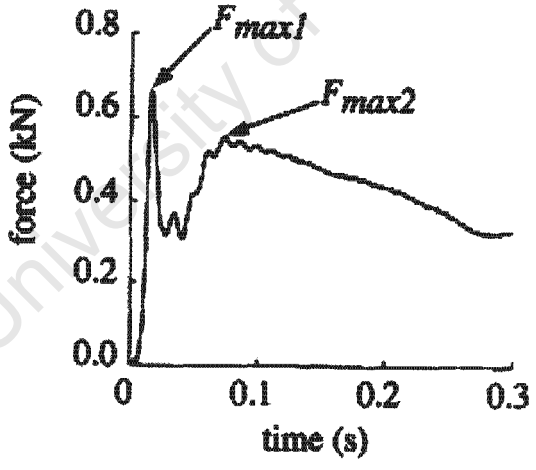

Figure 2.18: Graph of a typical force-time profile. Where force plates were used to measure the forces applied to the body during a fall onto the outstretched hand [11].

Pre impact decent phase

Fall arrest has three post-initiation phases; a pre-impact decent phase, an impact phase and a post-impact phase. The pre-impact phase is the short time from the instant of the loss of balance to the impact of the fall. The impact phase occurs when the hand has made contact with the ground. The post-impact phase occurs after the moment the hand has made contact with the ground. The pre-impact or descent-phase is longer than the post-impact phase.

Therefore, the forces and moments applied to the hands and wrists produced by the impact surface are determined by the pre-impact neuromuscular state, not what neuromuscular changes occur during the impact. This is due to the impact phase duration being so short that the reflexes are too slow to effect any substantial changes in neuromuscular response [6]. The peak impact force, (F_{max1}) in figure 2.18 is thought to be the force that causes injury. Two factors effect the magnitude of the peak impact force; the mechanical properties of the impact surface [30] and the impacted tissues [12, 15], as well as the kinematics of the body upon impact [13, 12, 14, 16].

The main objective in injury prevention mechanisms is to configure the body in such a way so as to reduce the risk of fracture upon impact. This configuration must occur during the pre-impact decent phase. Most of the energy at impact is derived from the conversion of the potential energy of the body's initial mass centre height to kinetic energy at impact. Dissipating some of this energy during the decent phase represents an important aspect of the decent phase.

Studies by DeGoede et al. [12] and Chou et al. [13] on forward falls arrested by two hands have focused on the relationship between the joint loading and the position of the forearm and the elbow. These studies stressed the importance of energy absorption by the shoulder and elbow during a forward fall. The identification of the biomechanical factors of the faller's protective response can be used to design efficient fall arrest strategies or to create fall prevention programs against upper extremity fractures.

DeGoede et al. [12] experiments involved the arrest of a ballistic pendulum that moves towards the subject at typical fall speeds. The experimental setup is shown in figure 2.19. This was carried out in order to look at what the effect of flexing the elbow and the effect of the velocity of the impact mass relative to the hands at the time of impact has on the impact force. It was found that flexing the elbow and decreasing the velocity of the hands

and arms relative to the impact surface results in a decrease in impact force on the hands by 40%.

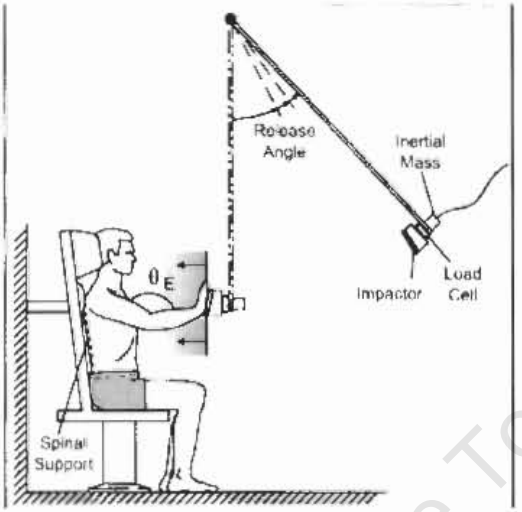

Figure 2.19: Experimental setup: Subject was seated in a rigid chair and arrested a ballistic pendulum with both hands [12].

Studies by Chou et al. [13], DeGoede and Ashton-Miller [14] and Kim and Ashton-Miller [15] studied the fall mechanism in terms of the kinematics around the wrist, elbow and shoulder joints during fall arrests. The effect of flexing (stiff arm landing) or extending the elbow (minimum impact landing) at the moment of impact was studied by subjects falling onto a force plate. The effect of subjects undergoing these effects after impact was also studied by Chou et al. [13]. The effect of voluntary initiated falls, sudden onset of falling (a cable attached to the subject was released after a random time delay) and age on peak impact force was studied by Kim and Ashton-Miller [15]. The experiential setup was as shown in figure 2.20. The piezoelectric force plate was used to measure the following forces; the vertical force (ground reaction force), two shear forces.

The main loading forces at the moment of impact of the three joints (wrist, elbow and shoulder) were axial forces [13]. For the case of pre-impact modifications, the largest impact force was found for the stiff arm landing case [14]. Flexing the elbow lead to a decrease in time period from hand/ground contact to F_{max1} and F_{max2} respectively [13] and a decrease in magnitude of F_{max1} and F_{max2} [14]. These results can be seen in figure 2.21. Therefore, elbow flexion upon impact results in less axial upper extremity force and thereby delays the maximum ground reaction force. Self-initiated falls resulted

in 1015 times higher peak impact forces and 23 times shorter body braking time than sudden onset fall situations [15]. Older adults were found to have experienced 10-15 times higher peak impact forces. This is thought to be due to an increase in the time taken for sensory detection of falling, therefore leaving less time for reflexive activation of the relevant muscles. Post impact modifications were found to have no effect on the impact forces transmitted [13, 15].

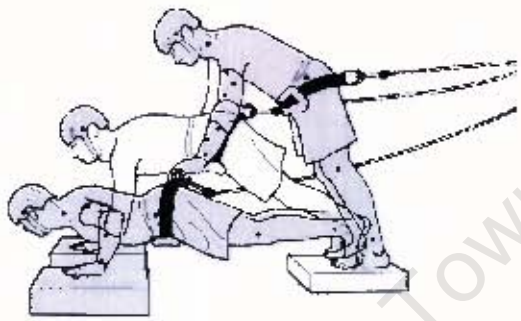

Figure 2.20: An experimental setup whereby subjects were released to fall onto force plates [14].

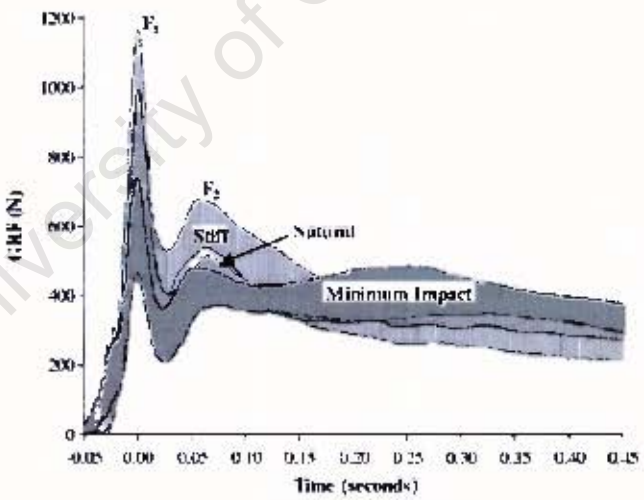

Figure 2.21: Graph showing the variation of ground reaction force with time for three different fall arrest strategies [14].

Experimental studies [11, 13, 31, 14] of how the upper extremities arrest the body momentum at impact, after a forward directed fall have been carried out. This restricts the body to the sagittal plane and initially positions the upper extremity in a symmetrical manner with respect to the trunk. During these experiments the unavoidable preparation time before the fall initiation allows the subject to preplan their response. However, in the actual fall event, the preparation time is reduced or not present. Frontal and transverse plane rotations during falls have also not been studied by these experiments.

The effect of the lack of preparation time was initially studied by Kim et al. [15]. The effect to which hand motion is symmetrical as well as the lack of preparation time was also studied by Troy and Grabiner [16], in forward-directed trip-induced fall experiments. The experiment involved the subject being supported by a safety harness and the trip was induced by a concealed, pneumatically driven obstacle that rose 5cm above the floor in about 150ms, as seen in figure 2.22. The motion of the subjects were measured using passive reflective markers. The results from these experiments showed that older women use their arms in a spatially asymmetrical manner during the decent phase of a trip-induced fall.

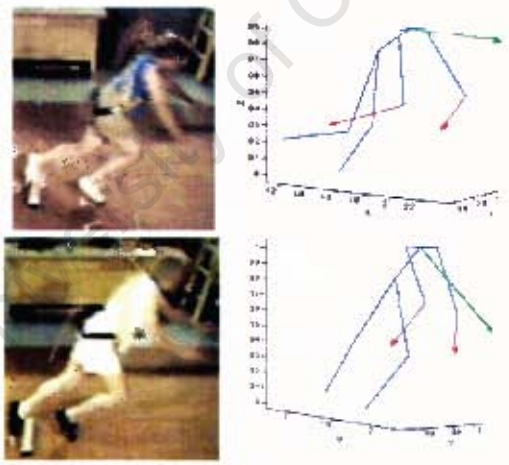

Figure 2.22: Experimental setup showing video images and motion tracking using reflective markers of fall experiments [16].

To quantify the influence of asymmetrical ground impact on the kinetics and kinematics following a simulated forward fall, Troy and Grabiner [16] also conducted forward falls from an upright kneeling position onto two force plates. Each hand contacted a different force plate in a symmetric or asymmetric manner. For the symmetrical protocol, the left and right hands were targeted to identically numbered targets on the left and right force

plates. This setup is shown in figure 2.23. The peak force magnitude and direction were studied.

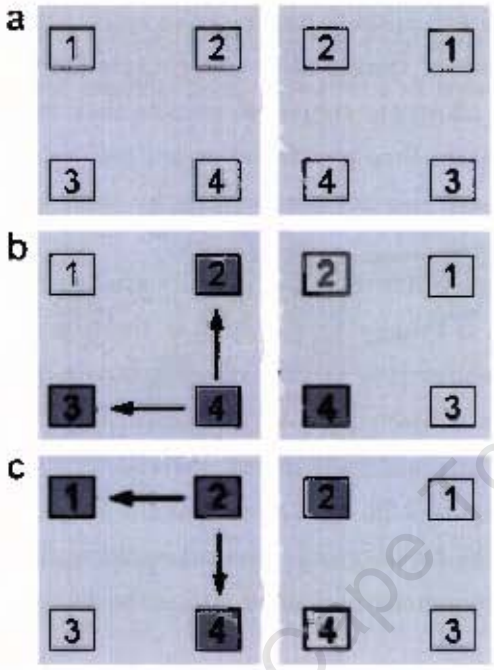

Figure 2.23: Experimental setup showing location of the four targets in symmetric falls (a), each hand targets the same target. In asymmetric falls the non-dominant hand was moved (b and c) [16].

The results found that asymmetry is both spatial and temporal. The temporal offsets were found to be 33ms for the asymmetric case, versus 11ms for the symmetric case. Temporal and spatial offsets influence the direction, but not the magnitude of the reaction force. The peak reaction force occurred $28 - 20$ ms for symmetric and $25 - 9$ms for asymmetric trials. The peak resultant force for the symmetric trails was $92 \pm 38\%$ body weight and for the asymmetric it was $94 + 30\%$. These results agreed with DeGoede and Ashton-Miller [14], who found that variations in time between hand impacts did not affect the peak ground reaction force of the hands. During a spatial or temporal asymmetric fall, energy absorption may occur from rolling from one hand to the next. This rolling is thought to be the explanation as to why larger temporal offsets are not associated with greater peak force magnitude.

Degoede and Ashton-Miller [14] suggested that the peak force magnitude is primarily dependent on the deceleration of the forearm rather than the total amount of energy

delivered to the forearm. They found that the peak impact force decreased the most when the elbow was flexed and that the velocity of the hands relative to the torso was reduced to zero. Therefore, given that the peak ground reaction magnitude may depend on the degree to which an individual rolls from one hand to the next and the degree to which the forearm must decelerate upon impact, the focus on reducing the total force magnitude through these two mechanisms may contribute to future improvements in fall arrest strategies.

2.5.2 Mathematical models

Mathematical models of biomechanical systems can be used to extend the results obtained from experiments into potentially injurious impact conditions and thereby give powerful insights of the biomechanical system studied quickly, safely and with little cost. These models are set up and then validated against experimental results. After this the model can be used to study the impact conditions.

Rigid body spring models (RBSM) are multisegment mathematical models with multiple degrees of freedom that have been used to study joint and segment motion, muscle and ligament forces and joint loading in a wide range of activities. RBSM use the equations of rigid body motion to simulate the fall dynamics of a person [11, 30, 31]. The body regions are modelled by sub-systems with defined mass and inertial properties. The sub-systems are connected by joints and simulated by springs and dampers to build up a two or three-dimensional system of rigid bodies.

Rigid body spring models of the torso and upper limb

Chiu and Robonovitch [11] used a RBSM to analyse impact forces during a forward fall arrest onto straight arms. An experimental study conducted at low heights was used to validate this work. This behaviour was simulated by a two-mass, two-degree-of-freedom RBSM, as shown in figure 2.24. The peak force was entirely determined by the impact velocity and the damping properties of the hand/ground-surface interface. The model was then used to study falls from greater heights between 0 and 2m.

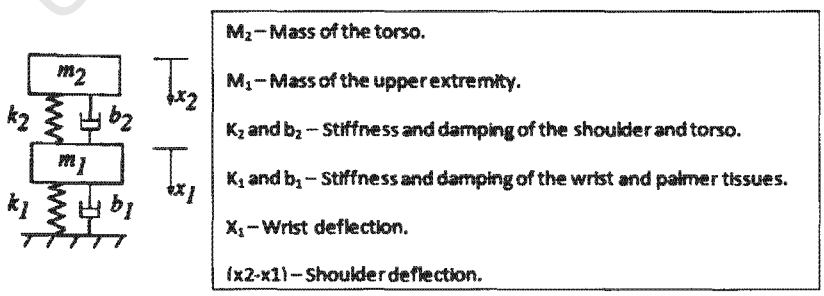

Figure 2.24: Schematic of the two-mass RBSM [11].

Figure 2.25 shows the results obtained in this study. The model predicted that increases

in fall height have a greater influence on F_{max1} than F_{max2}. Therefore a subject's risk of fracture is governed by F_{max1}. Fall heights greater than 0.6m were found to carry a significant risk for wrist fractures, due to above this height F_{max1} exceeds the average fracture force for the elderly distal radius. The impact responses of the wrist and shoulder are different. F_{max1} is not transmitted to the shoulder. The peak shoulder forces closely match F_{max2}.

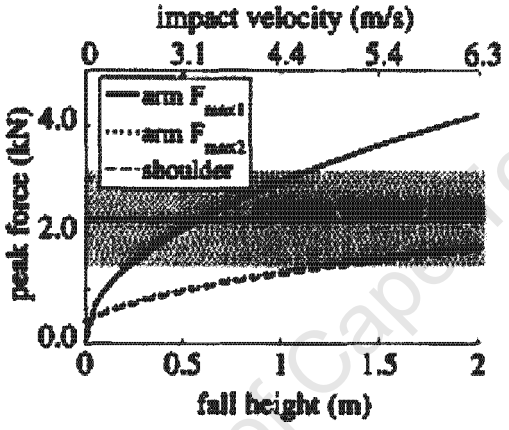

Figure 2.25: Peak impact forces for fall heights between 0 and 2m [11].

Davidson et al. [30] further modified the RBSM used by Chiu and Robonovitch [11] by taking into account the stiffness of the ground. This modification was made to improve the prediction of the likelihood of distal radius fractures that occur in children after a fall from playground equipment. The ground was added as a spring element to the RBSM. Factors such as fall height and surface type were considered and the effects on physical stress transmitted through the forearm and to fracture tolerance of the distal radius was considered.

The model was validated by data gathered from an epidemiological case-controlled study of falls from playground equipment in New Zealand. The model provides insight into how playgrounds may be redesigned to reduce the stresses caused by injury and provides information on the development of safety standards.

Rigid body spring models of the wrist

In RBSM models, the wrist is represented as a collection of rigid bodies interconnected by spring elements of known linear stiffness. The rigid bodies in the RBSM are representative of the bones in the wrist. Cartilage and subchondral bones are represented as compressive springs. Ligaments are represented by tensile springs. Force vectors applied to the model simulate physiological wrist loads. Applying the minimum energy principle to the system (the wrist), the force transmission and displacement of the rigid bodies (the bones) can be calculated.

2-dimensional models

Two-dimensional RBSM were generated by Schuid et al. [32] and Horii et al. [33] to determine the normal wrist joint pressures under physiological loading and to analyse how different procedures used for treating Kienböck's disease modify the force distribution across the carpus. Both models consisted of the five metacarpals, carpal bones, the radius and the ulna. Digitised planar radiographs of normal wrists in neutral positions were used to get the bone geometries. Twenty eight ligaments were modelled as spring elements (figure 2.26). Axial loads were applied along the axes of the five metacarpals, simulating a total grasp load of 140N [32, 33].

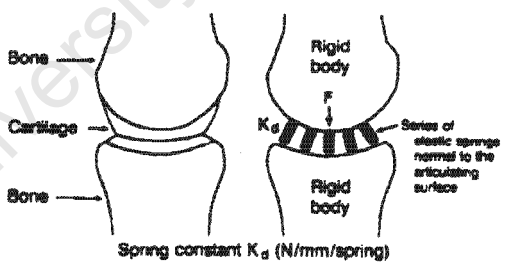

Figure 2.26: Diagram of a 2-d Rigid Body Spring Model [32].

3-dimensional models

Majima et al. [34] proposed a 3-dimensional RBSM to analyse the force distribution through the wrist joint. The force transmission during wrist extension (a fall event) was studied. The geometry for the model was obtained from Computer Tomography (CT) of a wrist in the extended position. 50 ligaments were modelled. The model was loaded by the grasp load being distributed to the five metacarpals, as shown in figure 2.27.

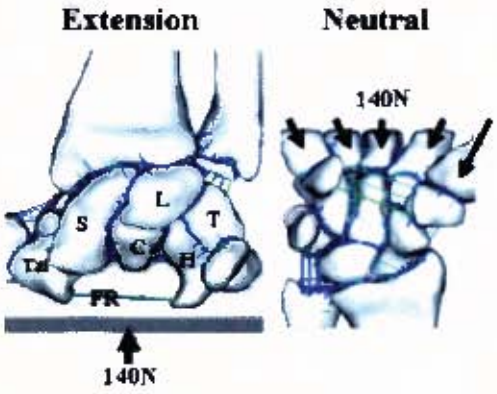

Figure 2.27: The loading patterns for the two different wrist positions [34].

The results showed force transmitted through the scaphoid fossa increased from 52% in the neutral position to 62% in extension. The ratio through the lunate fossa decreased from 42% in the neutral position to 36% in the extended position, as shown in figure 2.28. In the neutral position, force is evenly distributed in the mid-carpal joint, which is consistent with the excremental work of Veigas et al. [18]. In the extended position, high pressure areas were concentrated both on bilateral poles of the scaphoid and on the dorsal ridge of the lunate as shown in figure 2.29.

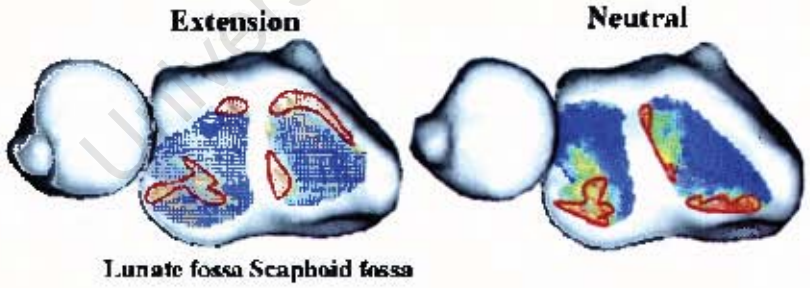

Figure 2.28: Pressure distribution for the articular surface of the distal radius, the red margins indicates high pressure areas [34].

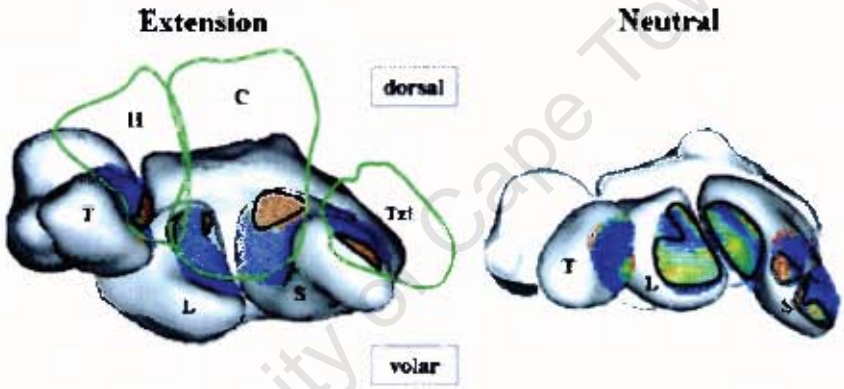

Figure 2.29: Pressure distribution through the mid-carpal joint. S, scaphoid; L, lunate; T, triquetrum; Tzi, trapezium; C, capitate, H, hamate. The red margins indicates high pressure areas [34].

2.6 Measuring the compressive pressure across the wrist joint.

Many different studies have been carried out to determine the magnitude and distribution of force across the wrist joint in both live and cadaver specimens. Being able to quantify the load mechanics of the wrist under various loading conditions can provide better understanding of a variety of normal and post-traumatic conditions of the wrist. The results provided by these measuring devices were used to validate mathematical models.

2.6.1 Physical testing using pressure sensitive film

The most common experimental method to quantify and observe force distribution in the wrist under a variety of loading conditions, is to insert Fuji (Fuji, Ithaca, NY) pressure sensitive film into the radio-carpal and/or mid-carpal joints of cadaveric specimens [48, 49, 18]. External loads in such studies were applied to the wrist either by the application of weights to various tendons [48] or by placing external fixtures in the metacarpal bones [18]. The colour density of the film changes with the increase in pressure. Figure 2.30 shows a result obtained from a typical experiment where region A indicates a high pressure region.

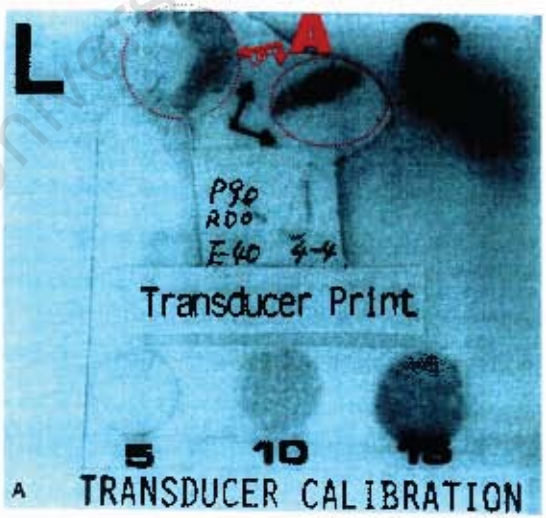

Figure 2.30: A typical pressure-sensitive film print of the radio-carpal joint [18].

Veigas and Patterson [18] conducted experiments using Fuji pressure film. They found

that there are distinct areas of contact within the radio-ulno-carpal and mid-carpal wrist joints and that the load transmission was as shown in figure 2.31. Figure 2.31 also shows that the distal carpal row acts as a single unit and distributes the load rather uniformly to the proximal carpal row.

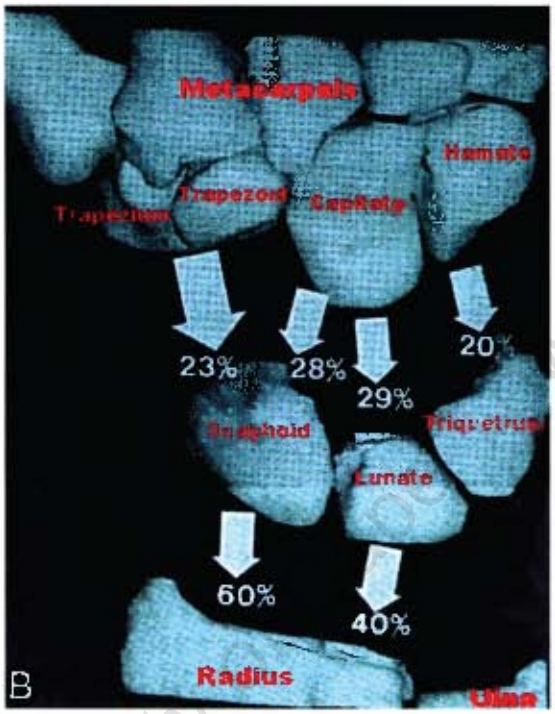

Figure 2.31: A three-dimensional image of the load distribution in the mid-carpal and radio-carpal wrist joints [18].

Figure 2.32 shows that the amount of contact in the radio-carpal joint accounts for 20% of the available joint surface, but that this value increases with increasing load to 40%. As the load increases, the cartilage compresses resulting in a larger contact area. The pressure measured in areas of contact increases as load increases. A maximum contact area is reached when cartilage can no longer compress any further. Once the maximum contact area is reached, the pressure increases indirectly in proportion to the load.

A comparison of the load transfer characteristics of the wrist with respect to loading configuration (2/5 metacarpals and weights suspended from the wrist tendons) found no statistically significant differences between the configurations [18]. The wrist configuration, either neutral or extended, was found not to directly influence the fracture load of the distal radius, but rather the load transfer pattern. The neutral position showed an equally distributed pressure pattern on the radial joint surface and the extended position resulted

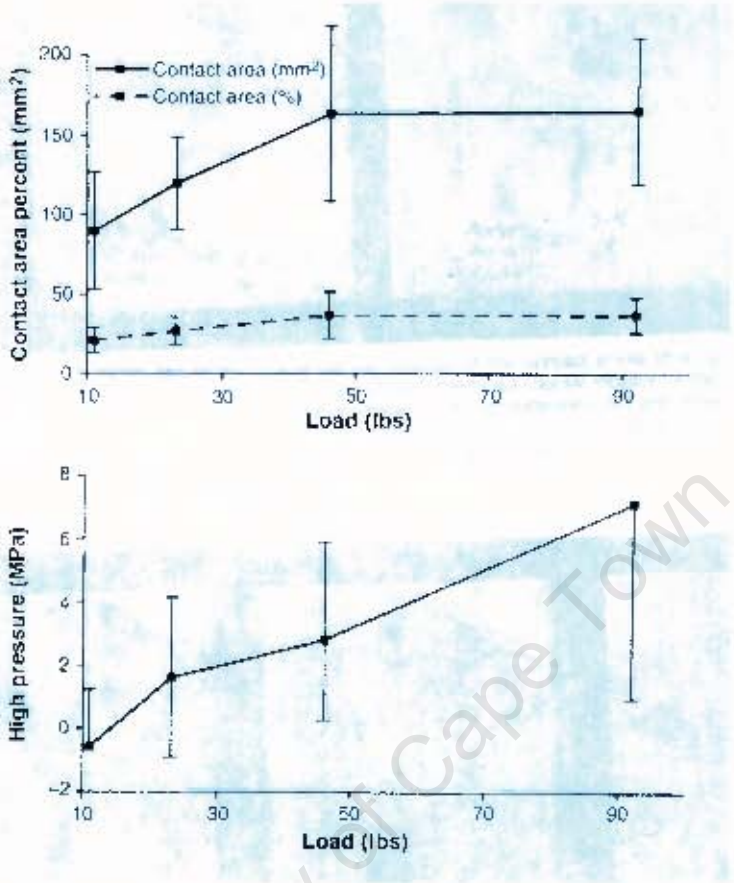

Figure 2.32: Graphs of contact area and maximum contact pressure versus load within the radio-carpal joint [18].

in a localised pressure spot at the centre [19]. The location of contact area on the radius changes in relationship to the position of the wrist, whereby there is a palmar shift within the articular surface of the distal radius and a dorsal shift with extension [18].

Mechanical testing

Strain gauges

The strain in the radial bone of live subjects has been measured in the subjects during activities of daily living by Földazy et al. [50]. Measurements were conducted by placing strain gauge bone staples onto the dorsal surface of the distal radial metaphysis of the subject. The activities included exercise and falls on extended hands. The strain rate for falling from standing height and from kneeling height was measured to be 45954 $\mu\epsilon/s$ and 18582$\mu\epsilon/s$ respectively.

Load cells

Ekenstam et al. [20] employed load cells to measure forces transmitted through the ulna and radius bones. The results showed that when the forearm is pronated and the ulna is deviated, there is less load along the radius. This position can be used to immobilise a fractured radius.

The problem with the mentioned experimental models (strain gauges, load cells and pressure sensitive film) [18, 19, 20] is that they are conducted on cadaveric arms and therefore only the osseoligamentous system is considered. The influence of dynamic muscle and tendon forces is unknown. Muscle action involves a complex system of reflexes and biofeedback loops that normally link the action of agonists, antagonists and stabilizing muscles that may absorb some of the applied load. Another problem with these methods is that the sensing methods used in these experiments were introduced by cutting the dorsal joint capsule [18, 19], therefore transecting the dorsal stabilizing ligaments.

Capacitive sensor

A device capable of measuring the force and pressure distribution across the radio-carpal joint under physiological conditions was designed and tested by Rikli et al. [21]. A capacitive sensor is used to measure both static and dynamic forces. The devices were tested on cadaveric specimens using a specially designed loading rig, where a mobile unit is pulled against a fixed unit, holding the forearm in place with two wires attached to a defined weight. Tests were then carried out in healthy volunteers under local anesthesia. The sensor was inserted in a region where the ligaments did not have important stabilizing functions. The experimental setup is shown in figure 2.33. For the in vivo tests, the sensor

was introduced surgically and the subject was asked to perform flexion/extension, ulna and radial deviation, thereby allowing the measurement of both static and dynamic loads.

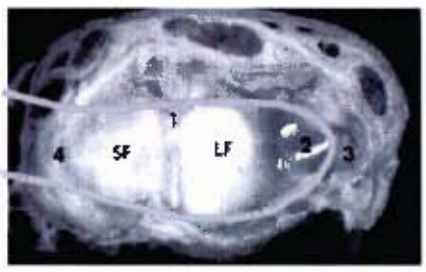

(a) The region covered by the sensor

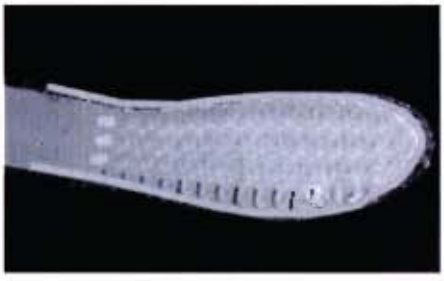

(b) The sensor

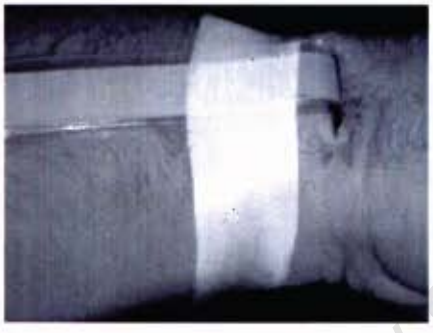

(c) The sensor with the subject

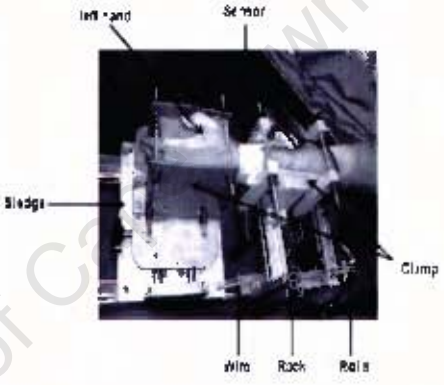

(d) The cadaveric testing rig

Figure 2.33: The experimental setup of Rikli et al. [21]. Where 1-region in between scaphoid and lunate, 2-TFCC, 3-ulnar styloid, 4-radial styloid, SF-scaphoid fossa, LF-lunate fossa.

The static studies found that there were two centres of force transmission in the distal radio-carpal joint. The first is located radially, opposite the proximal pole of the scaphoid and the other is located more ulnarly, opposite the lunate.

The effect of including active muscle responses (i.e. the dynamic study) found there to be a shift of contact pressure, in the distal radio-carpal joint, towards the ulnar side with ulna deviation and a shift towards the radial side with radial deviation. This was not the case for extension and flexion as seen in the static work by Veigas et al. [18], and there was no shift to the palmar with extension or the dorsal for extension. Therefore the dynamic studies main difference with the static studies is the contact pressure distribution not the magnitude.

2.7 Finite element model

The Finite Element (FE) method is a numerical analysis technique, one application of this technique is for studying musculoskeletal biomechanics. The FE-method breaks the body concerned into discrete elements and therefore approximates a continuous system. FE-modeling can be used to estimate stress and strain distributions within bone and tissue, such as cartilage or ligaments, and contact pressures in complex contact models. Examples of some of its applications in biomechanics are:

- Determining the hip joint contact pressure before and after surgical procedures [51].
- Simulating the human body under impact, such as in automobile accident testing [52].
- To predict the failure of a bone specimen [53].
- To study the effect of degenerating cartilage within a joint, such as the knee joint [54].

2.7.1 Two dimensional finite element models of the wrist joint

Two dimensional FE-wrist models were created to investigate stress patterns and how they are affected by; bone fracture [22], bone shape that is altered by an operation following a fracture [23] or a prosthetic bone [24]. These 2-d models are limited to the coronal plane and neglect the out-of-plane movement of the carpal bones.

These models, shown in figure 2.34, were constructed from traced microradiograms of a sectioned specimen. The models contained carpal bones, the radius and ulna. Bone and cartilage were modelled as linear elastic isotropic materials. The pressure distributions at the articular interfaces in the wrist was determined from these models. The results found that the prostatic implant studied could prevent the carpus from collapsing under applied loads [24]. The scaphoid is frequently fractured due to it playing an important role within the wrist force transmission column [22].

(a) Figure 1 [22] (b) Figure 2 [23] (c) Figure 3 [24]

Figure 2.34: Finite Element models of the wrist in two dimensions.

2.7.2 Three dimensional finite element models of the wrist joint

Two dimensional models provide reasonable agreement with contact stress distributions. But, they are limited to a single plane of analysis. The wrist joint has been found to undergo out-of-plane movements [16]. Therefore, 3-d FEM models have been used to analyse these movements.

The geometry for these models has been constructed from CT scan [25, 26, 27] or magnetic resonance images (MRI) [29] of the wrist joint of live subjects with their wrist placed in the position for the desired application of the model. For the models constructed from CT scan data, the inclusion of articular cartilage was restricted to a uniform thickness region layered on the end of bones. This is due to CT scan data just giving bone geometry. For the models constructed from MRI data and cryomicrotome sections of cadaver wrists [28], the bone and cartilage geometry was extracted. These models modeled bone and cartilage as linear elastic materials. The bones were connected by ligaments modeled as tension only non-linear spring elements. These material properties of these ligaments are further discussed in section 2.9.4.

Anderson et al. [28] and Troy and Grabiner [26] constructed models that investigated the radio-carpal contact stress distribution. These models included only the distal portion of the radius, the scaphoid and the lunate bones. Loads were applied to the distal surfaces of the scaphoid and lunate. Anderson et al. [28] model included the support provided by the ulna through the TFCC, as a parallel array of compressive springs attached to fixed nodes on the lunate. Anderson et al. [28] investigated the effect of an intra-articular distal radius fracture on contact stress within the joint. The results of this model provided quantitative descriptions of the load transfer mechanism through the joint, thereby allowing the effect of different treatment procedures to be studied in the future.

Troy and Grabiner [26] used experimentally derived kinematics and kinetics [16] as boundary conditions for their model. The peak force was composed of both forces that acted along the axis of the radius and off-axially. The wrist was found to be extended and ulna deviated at the moment that the hand impacted the force plate. These results were used as boundary conditions for the FE-model to determine the effect of off-axis loading and bone quality (Osteoporotic bone) on the radial bone fracture strength.

The study found that the direction of the load applied to the radius has a very strong influence on fracture strength and the fracture initiation sight, as shown in figure 2.35.

The combined bending and compression from the off-axis loading resulted in a nearly 50% decrease in the estimated strength of the radius. This may provide a way of reducing the occurrence of Colles' fracture. A decrease of bone mineral density, seen during Osteoporosis, was also found to decrease the fracture strength in the model.

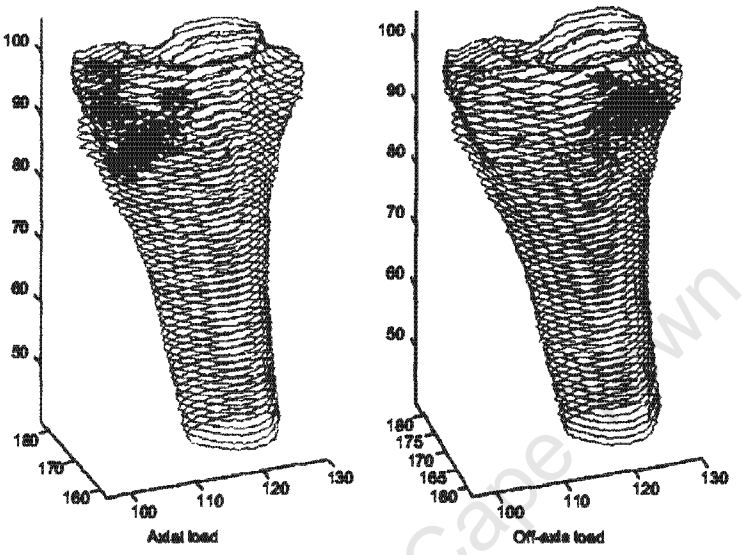

Figure 2.35: Distribution of failed elements when a failure (a) axial load, (b) off-axis load was applied [26].

Gislason et al. [29] also used physiologically realistic loads from experimental work as boundary conditions for their model to determine how load is transferred through the wrist joint during maximum grip. The internal metacarpophalangeal joint load used to load the model, was determined from the experimental maximum grip strength tests performed on subjects and a biomechanical model. The model included the distal radius, ulna, carpal and metacarpal bones.

Non physiological constraints were applied to all the FE-models discussed in this section in order to obtain solution convergence. All the carpal bones were constrained to only move in a direction parallel to the load [26] or the bones were brought into contact and not allowed to separate after loading [29]. These constraints were applied because the model did not provide static stability under compressive loading, due to the constraining activity of muscles not being modelled. The models were validated using cadaveric experimental work, whereby muscle activity is not present.

Carrigan et al. [25] investigated the effect of unconstrained motion of the scaphoid, in a

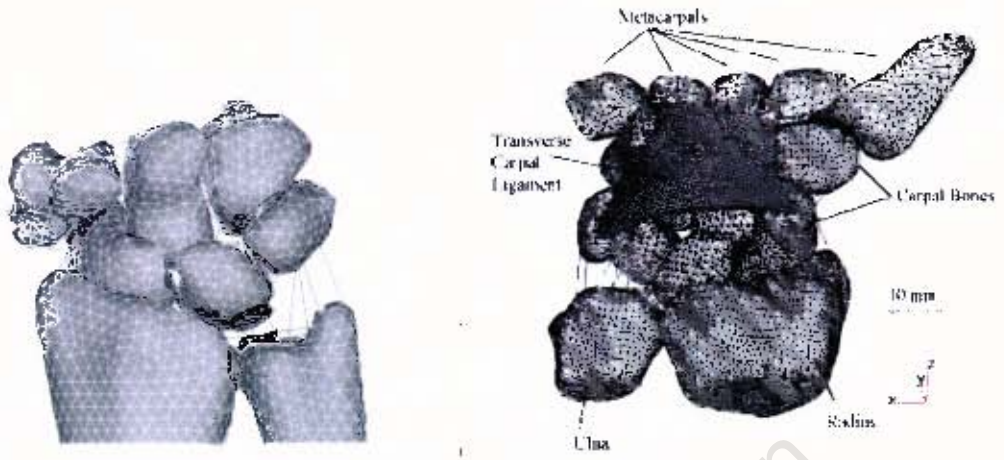

(a) Carrigan et al. [25] (b) Guo et al. [27]

Figure 2.36: Three dimensional FEM model geometry.

model that included cortical shells of carpal, distal radius and ulna bones (figure 2.36). Compressive loading was applied to the capitate. It was found that allowing the scaphoid to freely rotate decreased the contact pressure, area and caused a palmar ulna shift on the contact region of the radial articular surface. Guo et al. [27] used this method of constraint in a model that analysed the effect of a surgical procedure that involves dividing the transverse carpal ligament (TLC) on the mechanical behaviour of the carpal bones. The model included cortical and cancellous bone of the distal radius, ulna, proximal metacarpals, shown in figure 2.36. A grasping load was applied to the upper section of the second and third metacarpals. The results found that dividing the TLC lead to the carpal bones deviating more radially under compressive loads.

2.8 Biological capacity

2.8.1 Fracture loads

The load at which a bone fractures is dependent on many factors such as; bone geometry, bone properties, load application point, load direction (the angle the limb makes with the ground, as well as the angle the resultant impact force makes with the limb and the rate of load application) [55]. The fracture loads of the radius are between 1580-3180N for females and 2370-3773N for males [6].

The factor of risk for wrist fractures is defined as the applied load divided by the failure load. When this value is greater than one, a fracture is predicted to occur [17]. The applied load is defined as the load applied to the outstretched hand during a fall from standing height. The load is estimated as the product of a damping constant and the impact velocity associated with the fall. This impact velocity is calculated using the fall height as half the height of a subject [11]. The failure load of the wrist is determined through mechanical testing methods, such as those shown in figure 2.37. Load and displacement data was recorded and the failure load was determined from the load-displacement curves. Muller et al. [17] focused on the region of the radius, where Colles' fractures occurred. They found that women had a greater probability of fracturing their distal radius when falling from a standing height than men. The mean failure load was found to be 3231± 825N. The type of fracture that occurs in the distal radius was found not to be related to the loading configuration of the wrist (neutral of extended) or load transfer pattern (uniform or localised) [49]. Cortical bone was found to contribute the most to the bone strength of the distal radius. Mid-distal measurements (cortical bone mineral content and area) were found to be the best predictors of fracture load [49].

Fracture risk focuses largely on impact forces, rather than displacement or energy. A reason for this is that there is difficulty involved in determining the portion of total wrist displacement and energy absorption, due to deformation of the bone, rather than soft tissue. If deformation is small, an injury criterion based on deformation or energy would better reflect the risk for soft tissue injury. No methods exist for assessing wrist fracture risks in terms of displacement and energy. To generate a wrist fracture in terms of displacement or energy, further biomechanical tests need to be undertaken [6].

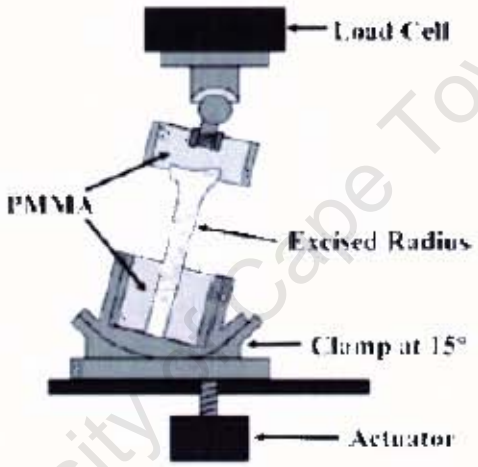

Figure 2.37: Diagram of mechanical testing configuration to determine radial failure loads [17].

Finite element models used to predict bone failure

There are two methods by which FEM has been used to predict the failure of a bone. These are by using micro-FE (μFE) and continuum models. μFE analysis uses high resolution digital images obtained from micro-computer tomography scanning to determine the precise trabecular architecture (discussed in section 2.9.1) of bone. μFE-models of the distal radius have been used to examine the stress and strain distributions with goals to predict the failure loads [35], determine how load is transmitted through bone and to identify potential sights of fracture initiation [36].

Bone failure in these types of μFE-models is said to be initiated if a certain percentage of the bone tissue (trabecular) would be strained beyond the tissue yield strain. The external force that created the strain was calculated from the FE analysis. An average fracture load of 1.40KN for the distal radius was predicted. The advantage of these models is that they account for the individual bone architecture of each person, an example is shown in figure 2.38. These type of models helps to clarify the loading mechanics of the trabecular bone. However, they did not specifically address potentially important changes in impact mechanics.

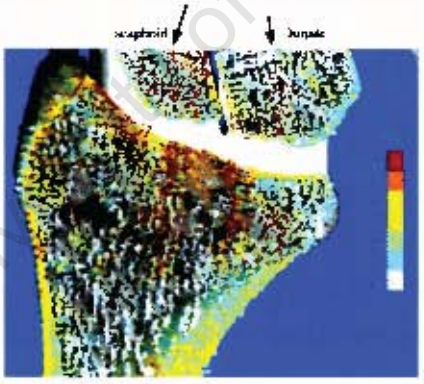

Figure 2.38: Contour plot of von misses stress distribution in a microFEM [36].

μFE analysis can be computationally inefficient as they involve millions of elements, the estimates of fracture load are generally unreliable and the failure criterion focuses on the failure of the trabecular bone. Cortical bone geometry and material properties have been found to contribute more to the bone strength than trabecular bone [56, 53] and especially for the case of the radius [37]. Continuum based failure models (macroFE) have been used to analyse femoral fractures [56] and radius fracture [37] in cortical bone. The reliability of bone fracture models depends on the accurate assessment of material properties and

specifications of the conditions at failure.

Material failure can be either locally stress or strain-controlled. Brittle fracture in stress-controlled and ductile fracture is strain-controlled. Keyak and Rossi [56] found that isotropic stress-based failure theories best predicted failure loads in the femur, regardless of the loading conditions. Stress-based failure theories were also used by van der Westuizen [53] in predicting the failure of bovine cortical bone. Pietruszczak et al. [37] evaluated the risk of cortical bone fracture in the distal radius by using a stress-based failure criterion. Load was applied to the surface of the radius to represent typical scaphoid and lunate loading. The model predicted Colles' fractures at loads that were consistent with experimental loads.

2.8.2 Osteoporosis

Osteoporosis is a skeletal disorder that leads to bone strength being compromised and leads to a predisposition to an increased risk of fracture. According to the Merck Manual [57], Osteoporosis is a progressive disorder that leads to a reduction in the cortical bone mineral density, bone thickness and in the number and size of the cancellous bone trabeculae. Bone re-absorption is also increased, but bone formation remains normal. Postmenopausal osteoporosis occurs in adults between the ages of 51 to 75 years and occurs six times more in women than men.

2.8.3 Colles' fracture

Colles' fractures are fractures of the distal region of the radius due to the bone being compressed on one side and extended on the other 39]. This occurs if the compression the lunate, scaphoid and anterior ligaments undergoes is transmitted to the distal radius. The compressive stress is transferred to the posterior surface of the radius, causing a crush of the radius. The tension stress occurs on the anterior surface of the radius, thereby leading to a rupture of the structures. A Colles' fracture (figure 2.39) is an extra-articular fracture (occurs away from the radio-carpal articulation) that is usually situated 15-20mm below the articular surface of the radius [45], this has also been shown in a FE-model of the radius (figure 2.40).

(a) Normal (b) Colles' fracture

Figure 2.39: An Xray showing the location of a typical Colles' fracture (palmar view) [58].

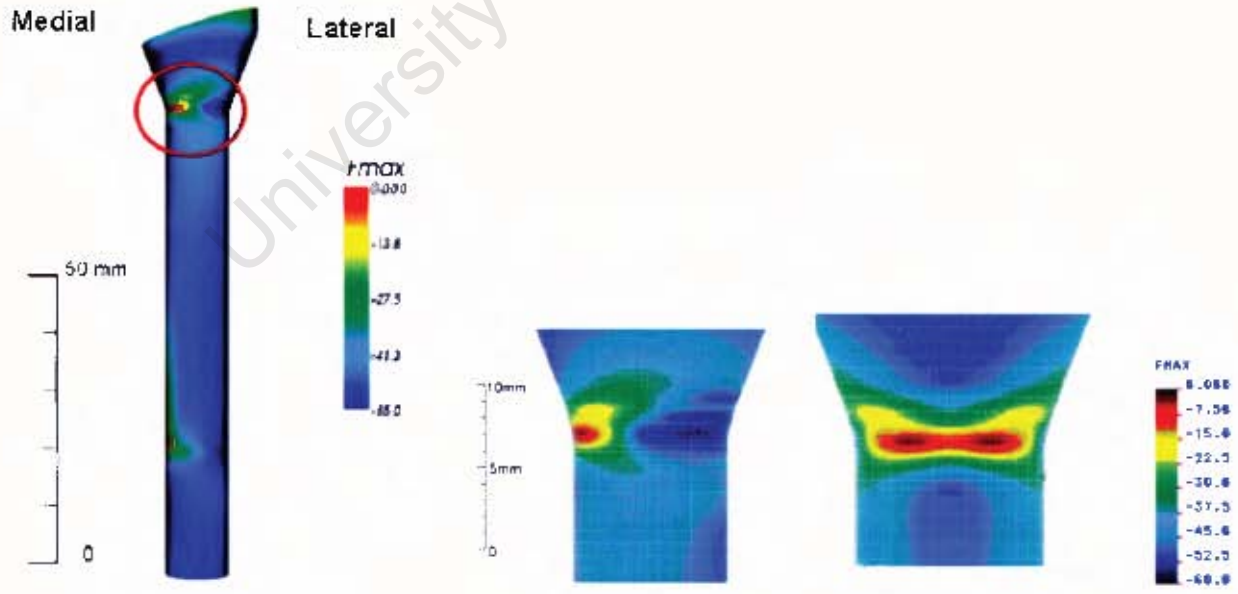

(a) palmar view (b) palmar view (c) Medial/lateral view

Figure 2.40: FE-model of the radius showing the location of a Colles' fracture (Load 700N) [37]. F_{max} is a variable used to indicate failure, where red regions indicate bone failure.

2.9 Material properties

Only the macroscopic structures (bone, cartilage and ligaments) of the body were considered relevant for the modelling work contained within this thesis. A model with microscopic structures, blood vessels and nerves ect., would require a great deal of computational resources. Such a model requires a large number of variables and there are many uncertainties in material properties definitions of the microscopic structures [36, 46].

2.9.1 Bones

An adult skeleton consists of 206 distinct bones. These bones can be categorised as [43]:

- **Long bones**, found in the extremities such as the radius and ulna.
- **Short bones**, forming the carpal and tarsal bones.
- **Flat bones**, forming the ribs and skull bones.
- **Irregular bones**, forming the vertebrae.
- **Sesamoid bones**, located within tendons, like the patella and pisiform

Bones act as; a lever system for transfer forces, an attachment site for muscles and give protection to vital internal organs. Bones also have a physiological function to form red blood cells, store calcium and store phosphorus [38].

The macroscopic bone structure

Long bones (figure 2.41) have a macroscopic structure consisting of a tubular shaft called the *diaphysis* and two large rounded ends called the *epiphyses*. The epiphysis is protected by a layer of hyaline cartilage, referred to as articular cartilage. This is the region of a bone that articulates with other bones. Surrounding and attached to bone, except for areas covered by cartilage is a tough vascular, fibrous tissue called the *periosteum* [43]. The periosteum is firmly attached to the bone and the periosteal fibres are continuous with ligaments and tendons that connect to the tissue [38].

The wall of the diaphysis is made up of tightly packed dense tissue called compact/cortical bone. This bone type is strong, solid and resistant to bending. The thickness of cortical bone varies between and within bones as a function of the mechanical requirements of the bone. The epiphysis is composed of spongy or cancellous bone with thin layers of compact bone on its surface. Cancellous bone is less dense that cortical bone [38, 59]. The diaphysis of a long bone surrounds a hollow structure called the *medullary cavity.* This cavity is used as a fat storage sight. It is filled with a soft connective tissue called marrow and is lined by a thin, largely cellular connective tissue membrane, the *endosteum.* Projections of bone called processes act as attachment sights for ligaments and tendons [43, 60]. Short bones are found in the wrist and ankle, i.e. carpals and tarsals respectively. They have no shaft with a center composed of cancellous bone and a hard outer shell of compact bone [43].

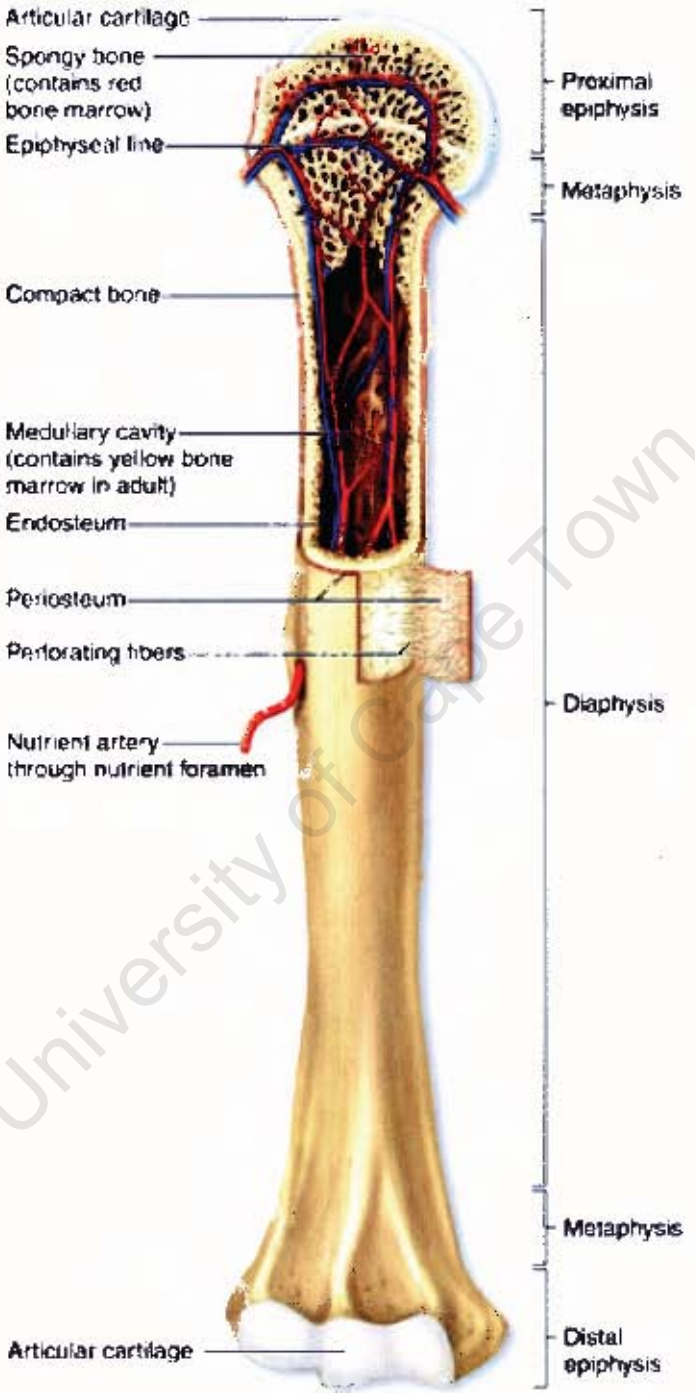

Figure 2.41: Diagram showing the macroscopic structure of long bone [60].

The microscopic structure of bone

Bone material is composed of cells, collagen (section 2.9.2) and inorganic salts. The cells produce a extracellular matrix. The extracellular matrix determines the material properties of the bone. Collagen gives bone its strength and resistance to loading and inorganic salts (mainly hydroxyapatite and calcium) make it hard and resistant to crushing [38].

The network of interconnected fibres of collagen form sheets of bone called lamella [60]. The plane of lamella winds around a central opening called the haversian canal. The haversian canal contains blood vessels and nerves. This system of concentric lamella and the canal is called the haversian system or an osteon, as shown in figure 2.42. Cortical bone is composed of the interconnected osteons of bone that are aligned parallel to the long axis of a bone [59].

Cancellous bone (figure 2.44) has a three-dimensional lattice-like structure of fibres (*trabeculae*) to better distribute the stress. The trabeculae of cancellous bone can be in the form of plates or rods. These structures have been known to orientate themselves in the direction of forces applied [61].

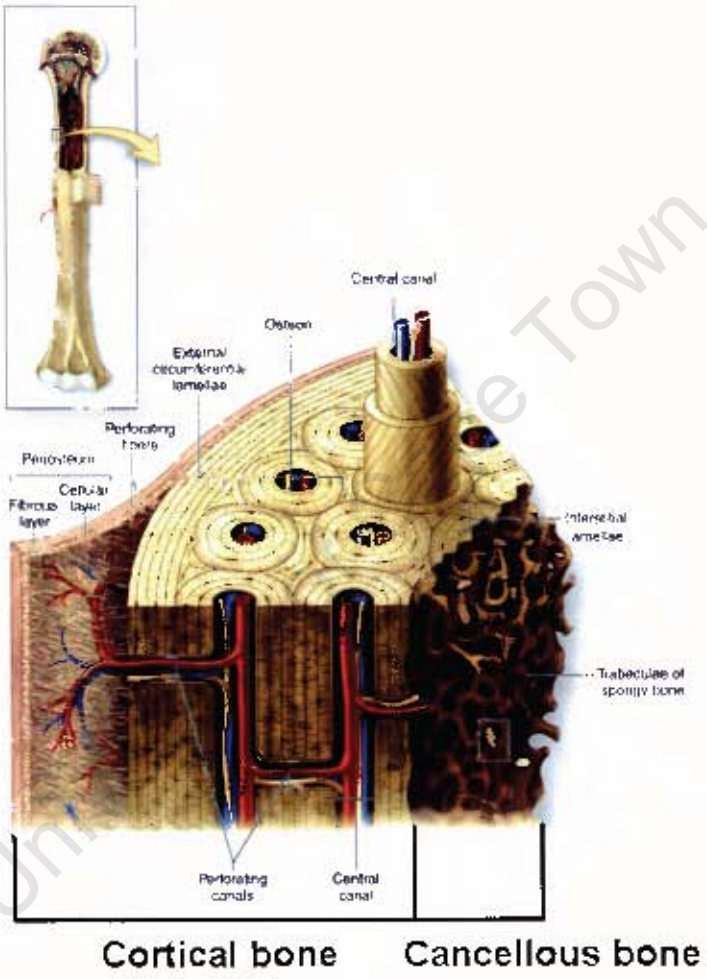

Figure 2.42: Diagram showing the microscopic structure of long bone [60].

Bone properties

The structural properties of bone are related to the complex organisation of cortical and cancellous bone material within a bone, the material properties are defined for cortical and cancellous bone individually [59]. To determine the structural properties whole bone specimens are tested using compression tests. Applied load to deflection curves are determined by these methods giving the stiffness and ultimate load of the particular bone. An example of such experimental work for the radius bone is given in section 2.8.1.

The material properties are determined from the testing of a machined solid specimen of bone tissue, either a piece of cortical or trabeculae bone of known geometry. There are many factors that influence the material properties and fracture strength of a sample of cortical or cancellous bone. These factors will be mentioned briefly and discussed in the paragraphs that follow:

- Material orientation and location.
- Age and gender.
- Mode of loading.
- Apparent density.
- Strain rate.

Material orientation and location

Cortical bone is considered to be an orthotropic material with a set of different material properties in three orthogonal directions, this can be seen in figure 2.43 and table 2.3. The anisotropy of material properties is due to the overlapping layers of lamella patterns. Bone grows in such a way that its greatest load bearing capacity is structured in the axial direction. The axial direction is defined according to the Haversian osteons of the cortical bone and according to the special main direction of the trabecular structures of cancellous bone [37]. Figure 2.44 shows that the architecture of cancellous bone also varies with anatomic site [61]. The distribution and number of plates and rods within a sample influences its material properties.

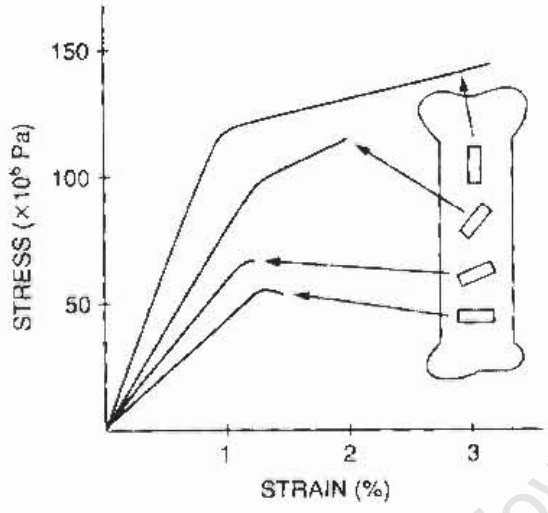

Figure 2.43: Stress-strain curve for cortical bone tested in different orientations [47].

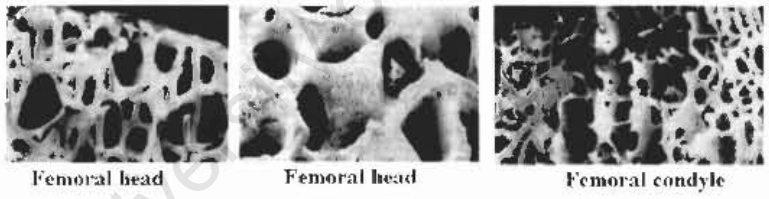

Figure 2.44: Rod-plate structure of cancellous bone from different locations within the femur bone [61].

Reference	Bone details	E_1	E_2	E_3	G_1	G_2	G_3
Homminga [62]	Hip cancellous bone	1.65MPa	0.83MPa	0.52MPa	1.40Mpa	0.72MPa	0.88MPa
Krone [63]	Femur cortical bone	6.30GPa	6.88GPa	16.00GPa	3.60GPa	3.20GPa	3.30GPa

Table 2.3: Anisotropic elastic and shear moduli.

Mode of loading

The mode of loading of a bone has an effect on the type of fracture that results [47], a schematic of these various loading modes is described below and shown in figure 2.45. Cortical bone has been shown to have inelastic responses that differ in tension and compression (figure 2.46).

- Daily loading of bone is compressive by nature, more extreme compressive loading, such as impacts from falls, can result in fractures.
- Shear loadings applied parallel to the surface of the structure, results in deformation of the internal cancellous bone.
- Bending fractures can occur when one end of the bone is relatively fixed and the other end is loaded, creating a bending moment, causing the bone to bend about its longitudinal axis.
- Torsional fractures occur when the bone twists about its long axis.

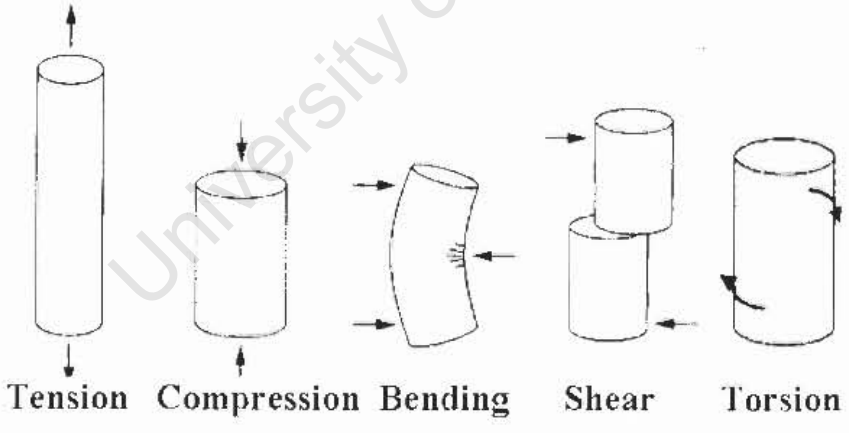

Figure 2.45: Schematic of the various loading configurations [47].

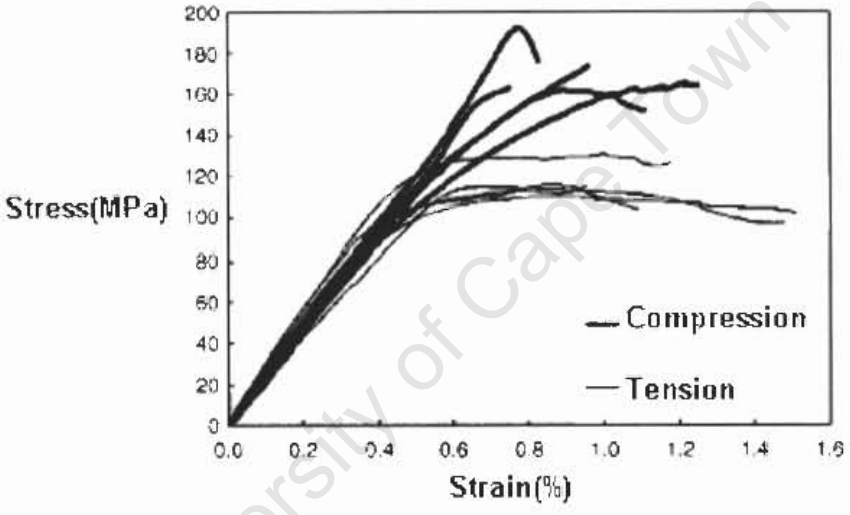

Figure 2.46: Comparison of compressive and tensile bone responses for human tibial cortical bone [64].

Apparent density

The Young's modulus and strength of both cortical and cancellous bone vary as a function of apparent density, illustrated in figures 2.47 and 2.48 [61, 65]. Apparent bone density is the density of the bone mineral without the fat and liquids, which do not contribute appreciably to the load bearing ability of the structure.

A relationship has been determined by Rho et al. [66] between mechanical properties of bone and the; apparent density and CT numbers. The relationship is between the elastic modulus and the other two variables. Bone specimens in water were scanned using a CT scanner. The raw CT values (for each pixel making up the CT scan) was converted into Hounsfield Units(HU) by relating the bone values to nearby water CT_w (HU=0) and air values CT_a ($HU = (-1000^{14})$) with the following formula:

$$HU = 1000\frac{CT - CT_w}{CT_w - CT_a} \tag{2.1}$$

Bone density is defined as the mean value expressed in Hounsfield units in each pixel of the ct scan.

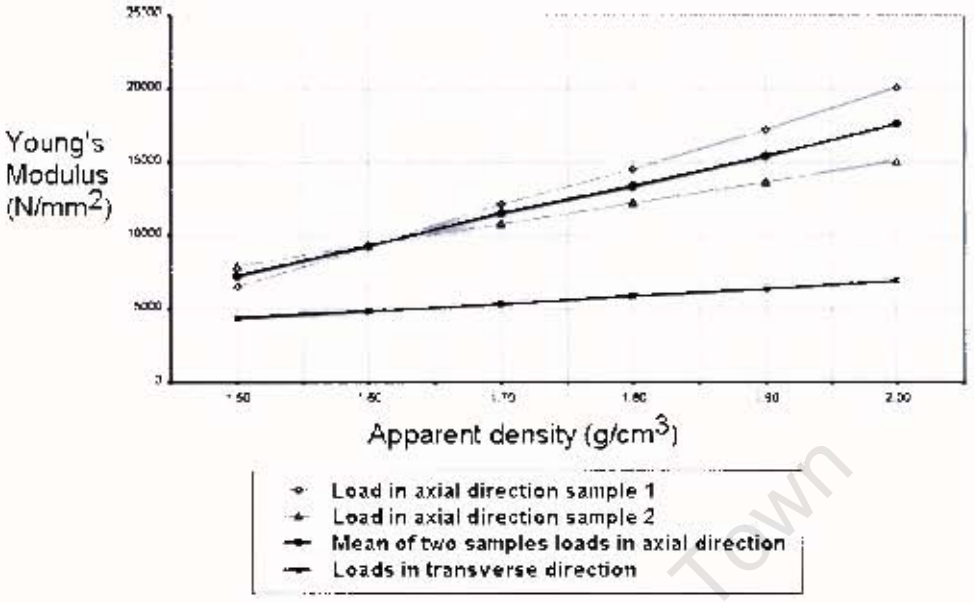

Figure 2.47: Young's Modulus versus density for cortical femoral bone in the axial and transverse load directions [65].

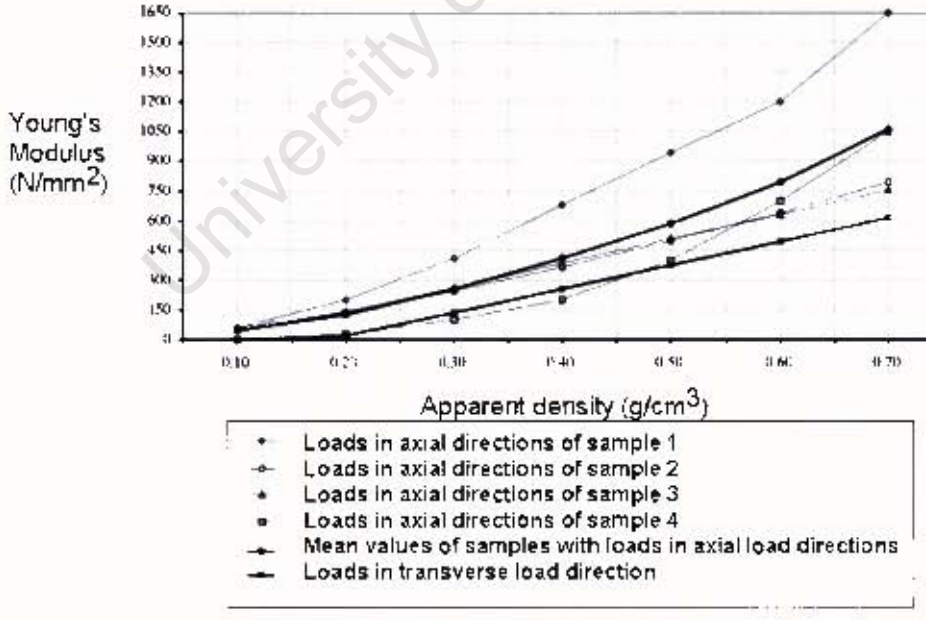

Figure 2.48: Young's Modulus versus density for cancellous femoral bone in the axial and transverse load directions [65].

Strain rate

Strain is defined as the deformation per unit length, therefore strain rate is elongation per unit time [67]. Bone behaves in a visco-elastic manner. Visco-elastic behaviour occurs when a materials response to a constant force or deformation varies over time. In contrast an elastic materials behaviour does not vary over time [47]. This visco-elastic behaviour noted experimentally during dynamic and quasistatic testing of bovine cancellous [68] and cortical bone [53] is function of strain rate and apparent density. The stress-strain behaviour of human cortical bone also exhibited this dependence, as shown in figure 2.49.

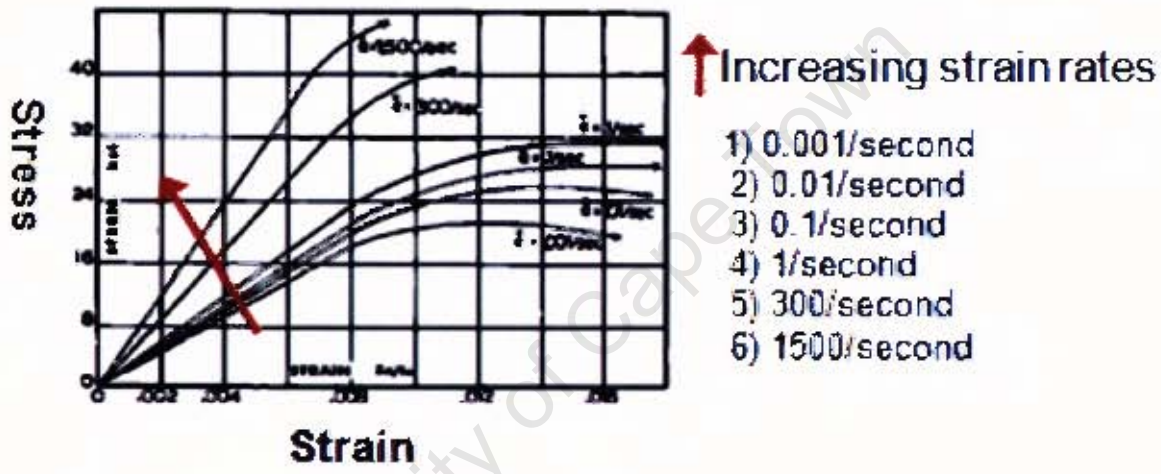

Figure 2.49: The strain rate dependent response of human femoral cortical bone in compression [69].

The material properties of bone are very complex, hence for the FE-modeling used in this thesis bone was modelled as a linear elastic isotropic material. A complex material model, that considers the parameters described in this section, is only superior to a linear model if there is experimental data to validate the material model. The tables that follow list the mechanical properties of cortical (table 2.5) and cancellous (table 2.4) bone found in the literature that have been used in previous FE-models or material tests. Young's modulus and Poisson's ratio were varied within this range for the model development stage of the modelling work contained within this thesis.

Reference	Anatomical region	Young's Modulus (MPa)	Poison's ratio	Density (g/cm^3)
Troy and Grabiner [70]	Wrist	100MPa-1.9GPa		
Anderson [28]	Wrist-cancellous	1400, 690, 345MPa	0.3	
	Wrist- subcondral	2800	0.3	
Oda et al. [24]	Wrist	100MPa	0.2	
LeDoux [22]	Wrist - All bone	18GPa		
Miyake [23]	Wrist - cancellous	100MPa	0.2	
	Wrist - subcondral	1GPa	0.2	
Pistoia [35]	Wrist	10GPa	0.3	
Cheug [71]	Foot	7.3GPa	0.3	
Philips [72]	Pelvis	150MPa	0.2	
Majumder [73]	Hip	32-3340MPa	0.2	
Zhang [74]	Lumbar spine	100MPa	0.2	
Higgins [68]	Bovine - experimentally			1.33
Gislason [29]	Wrist	100MPa	0.25	1.3
Keaveny [61]	Experimentally		0.3	
Range		32-18000MPa	0.2-0.3	1.3-1.33

Table 2.4: Summary of material properties of cancellous bone.

Reference	Anatomical region	Young's Modulus (MPa)	Poison's ratio	Density (g/cm^3)	Thickness (mm)
Guo et al. [27]	Wrist	10Gpa	0.3		
Carrigan [25]	Wrist	10Gpa	0.3		
Troy and Grabiner [70]	Wrist	5.7-20.7Gpa			
Anderson [28]	Wrist	13.8Gpa	0.3		
Oda et al. [24]	Wrist	15Gpa	0.3		
LeDoux [22]	Wrist - All bone	18Gpa			
Miyake [23]	Wrist	15Gpa	0.3		
Pistoia [35]	Wrist	10Gpa	0.3		
Cheug [71]	Foot	7.3Gpa	0.3		
Philips [72]	Pelvis	18Gpa	0.3		
Majumder [73]	hip	22.7Gpa	0.3		
Zhang [74]	Lumbar spine	12Gpa	0.3		
Bosisio [75]	Radial bone	16± 1.8Gpa			2.9± 0.6
van der Westhuizen [53]	Bovine			2.1	
Jost [52]	Whole body	2.5-12Gpa	0.3	1.0-2.5	
Gislason [29]	Wrist	18GPa	0.2	2	
Range		2.5-22.7GPa	0.2	2-2.1	

Table 2.5: Summary of material properties of cortical bone.

2.9.2 Soft tissue

Ligaments, tendons, fascia and cartilage are composed of soft tissue. These elements provide structural support to the musculoskeletal system and transmit force between the components. All connective tissue is composed of cells, an extracellular matrix of fibres and a ground substance.

There are 3 main types of fibres; collagen, elastin and reticulin [47]. Collagen fibres provide the strength and stiffness to the tissue. Collagen fibrils have a high tensile stiffness, they are thought to have negligible compressive strength, as they are assumed to buckle when subject to compressive loading.

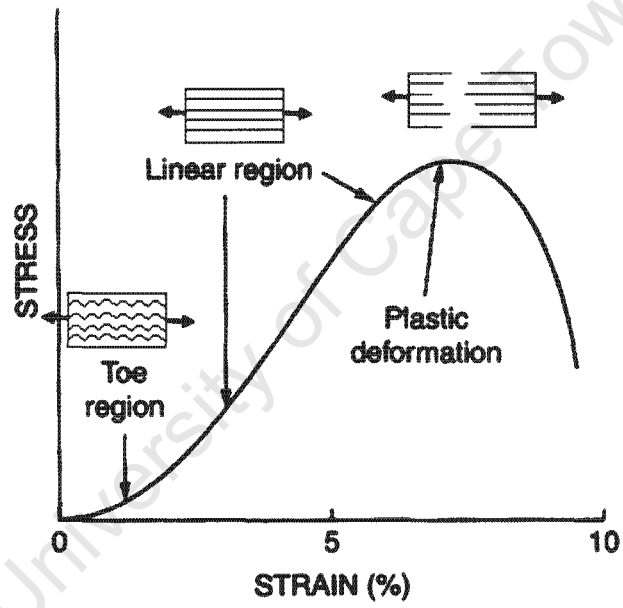

Figure 2.50: Stress strain curve for collagen fibres in tension [47].

Figure 2.50 shows the stress-strain relationship for collagen fibres, the fibres have a small toe region (up to 1% strain) in which the kinky strands are straightened, proceeded by a relatively linear elastic region up to roughly 7%. Plastic deformation follows with ultimate failure at roughly 10%.

Elastin fibres stress-strain behaviour differs from that of collagen, in that the fibres are elastic up to roughly 200% strain, at which point the fibres have lost their elasticity and become stiff under increasing stress and eventually fail without plastic deformation.

Reticulin fibres provide the bulk to the soft tissue.

2.9.3 Articular cartilage

Articular cartilage is a stiff, load bearing connective tissue that covers the articular surfaces of bone in synovial joints [43]. The primary functions of articular cartilage are; transmitting force across joints, distributing articular forces to minimize stress concentrations and providing a smooth surface for the relative gliding of joint surfaces [59]. Cartilage is composed of cartilage cells (chondrocytes) contained with a matrix. The matrix contains collagen fibres that are embedded in a water-filled firm gel (ground substance). This ground substance is composed of a carbohydrate brush like macromolecule (proteoglycan molecule) [43, 38].

The mechanical properties of articular cartilage are characterised by its load-deformation behaviour. Figure 2.51 shows the three different methods used to determine this behaviour. These methods are; indentation testing [76], confined [77] and unconfined compression tests [78, 79]. The failure stress of articular cartilage was determined from compression testing to be 35.7MPa [76]. Cartilage is also avascular, meaning that it has a lack of direct blood supply therefore it cannot regenerate after being damaged [38]. Factors affecting material properties of articular cartilage are; water content, depth, degradation and age.

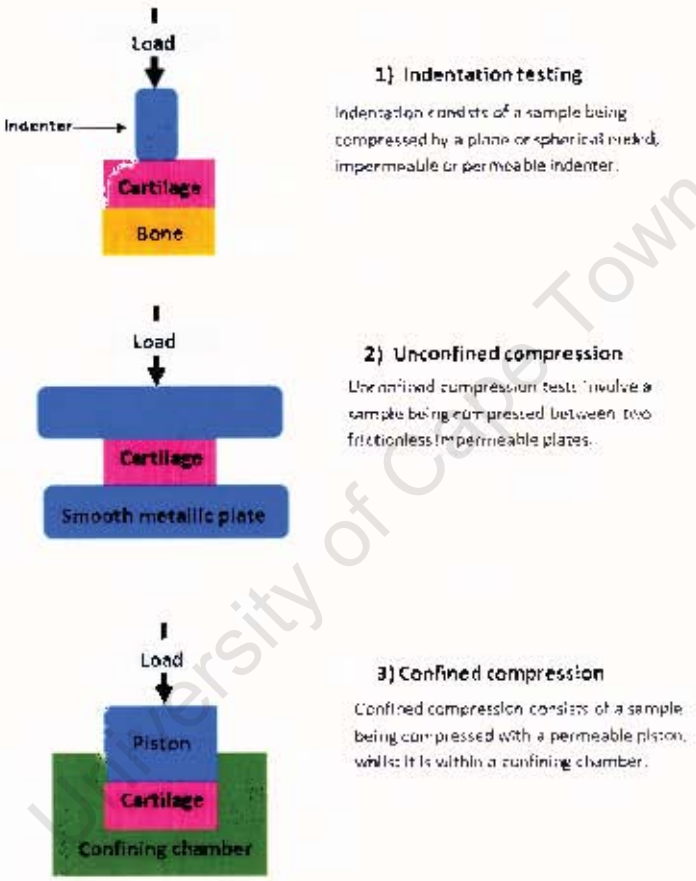

Figure 2.51: Articular cartilage testing methods.

Water content

The dependence of the cartilage material properties on water content and age of the tissue have been described experimentally by confined compression tests conducted by Armstrong et al. [77]. The results are shown in figure 2.52

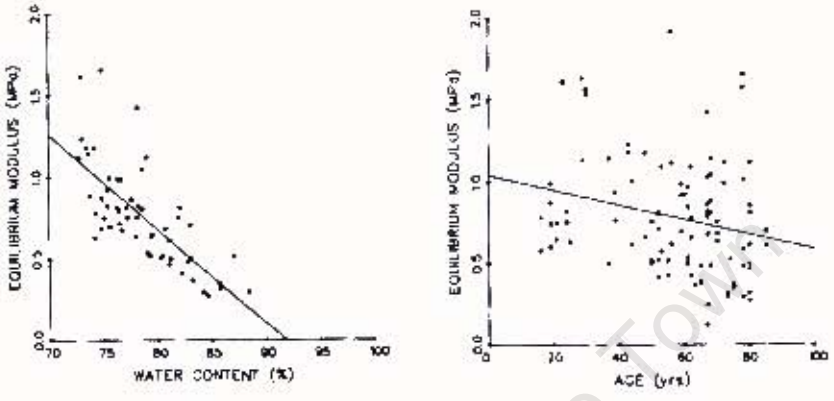

Figure 2.52: Cartilage equilibrium modulus versus water content and age [77].

Proteoglycans have a hyaluronic acid core with many side units. These molecules are strongly hydrophilic. They are attracted to water molecules, but are prevented from fully absorbing water and swelling by the collagen network. The collagen fibrils entrap the proteoglycan molecules [59]. The constraint by the collagen fibrils on swelling of the proteoglycan molecules causes an osmotic pressure and tensile stress on the collagen fibres when there is no external stress. When there is an external stress applied to the cartilage surface, the internal pressure in the cartilage matrix increases, exceeding the osmotic pressure. Therefore water is caused to be squeezed out of the cartilage, producing a naturally lubricating system. This fluid flow through the collagen network dissipates energy and operates like a damper. The collagen network gives cartilage its tensile strength and resistance to highly compressive repetitive loading, allowing articular cartilage to fulfil its primary functions [59]. This material behaviour of cartilage can be described by viscoelastic properties.

The deformation-time behaviour of cartilage is shown in figure 2.53. This behaviour is characteristic of a visco-elastic material behaviour, with an elastic deformation occurring initially followed by a slow creep. With release of the load, there is an initial elastic recoil followed by a slow recovery.

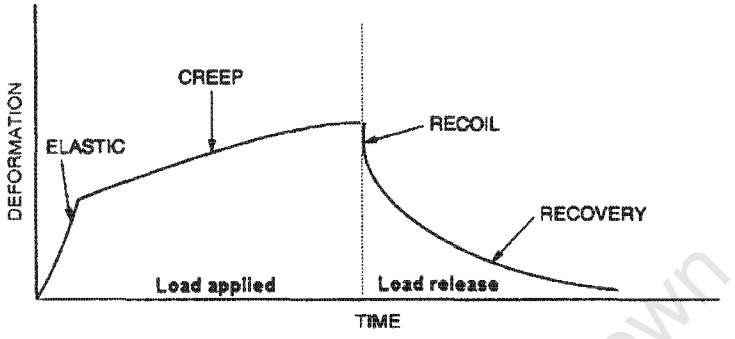

Figure 2.53: Deformation-time curve for articular cartilage [47].

The fluid that is squeezed out of cartilage during compression and reabsorbed during tension is known as synovial fluid. This fluid is present in a synovial joint between the two layers of articular cartilage. Articular cartilage works in conjunction with this synovial fluid to provide an almost frictionless movement of joint surfaces. The synovial fluid lubricates the joint and reduces the friction coefficient for the joint to a low value of $\mu = 0.002 - 0.005$ [59].

Depth

Articular cartilage is structurally heterogeneous and its material properties change as a function of depth, i.e. the distance from the cartilage surface to subchondral bone. This depth dependent behaviour is due to the four zones occurring within cartilage. Each zone contains different collagen fibril organisation and concentrations of proteoglycans, as shown in the schematic in figure 2.54 [47, 59]. The four zones are:

The superficial zone that forms the gliding surface of joints. This zone is $\pm 10\%$ of the cartilage thickness and contains the highest collagen fibril content. These fibrils are randomly aligned with a wave like pattern referred to as crimp. A deep layer within this zone consists of collagen fibrils aligned parallel to the cartilage surface, which follows the direction of normal joint movement and resists shear stresses. This zone has little proteoglycan, but the highest water concentration of all the zones (80%).

The middle zone is ±60% of the thickness of cartilage. In this zone collagen fibrils have a greater diameter than the superficial zone and are orientated in a random fashion. Proteoglycan content is also greater here.

The deep zone is ±30% of the cartilage thickness. This zone contains the largest diameter collagen fibrils, which are orientated perpendicular to the cartilage surface. The water content is the lowest and the proteoglycan content the highest.

The calcified zone provides a transition from the relatively soft cartilage tissue and the underlying stiff subchondral bone. This region contains hydroxyapatite (an inorganic constituent of the bone matrix). The calcified zone is separated from the deep zone by the *tidemark*. Collagen fibres from the deep zone cross the tidemark and anchor into the calcified zone (this is how cartilage adheres to bone).

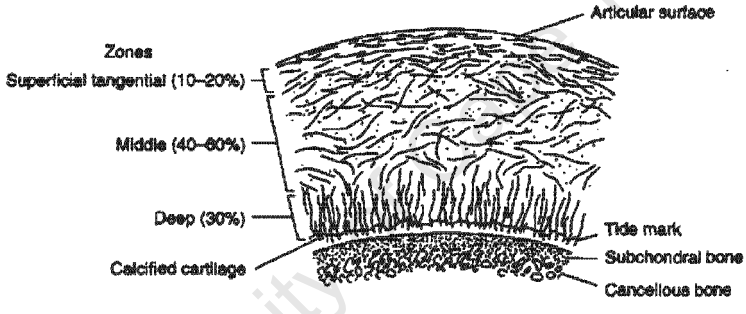

Figure 2.54: Diagram showing the four distinct zones of cartilage [47].

Fibrocartilage

Fibrocartilage, also present in synovial joints, is composed of mainly collagen fibres, hence it is a tough tissue. The main purpose of it is to act as a shock absorber attenuating the load applied to the structure. The TFCC is composed of fibrocartilage. Fibrocartilage is also present in the; vertebral column, knee and pectoral girdle [38]

Finite Element models of articular cartilage

A large proportion of FE-models of synovial joints of the wrist and other joints have modelled cartilage as a single phase substance, where the cartilage is a linear elastic, homogeneous and isotropic material [27, 25, 70, 24, 22, 23, 35]. These single phase models are used in cases where only an estimate of the external forces and the associated joint

contact mechanics are needed to be known. They are not suitable for the analysis of the internal mechanics of cartilage or to estimate the loads acting on the structural elements making up the cartilage.

The visco-elastic behavioural characteristics of articular cartilage can been modelled in different ways. A visco-elastic model with a combination of elastic (spring like) and viscous (damper like) elements can be used. This method was used by Jost [52] to model articular cartilage in an impact loading FE-model. Another method is to model the biphasic nature of cartilage, a solid in terms of the collagen and proteoglycans, and a liquid in terms of freely moving interstitial water. This technique is based on the biphasic model proposed by Mow in 1980. Wu et al. [79] described this biphasic behaviour whereby the individual components of the solid and liquid phases are incompressible, but globally they form a compressible fluid-saturated porous structure. The compressibility is achieved by allowing fluid to escape through the boundaries of the system. This model therefore describes the visco-elastic behaviour of cartilage in compression and the frictional drag associated with interstitial fluid flow.

Another method of describing the behaviour of articular cartilage is to describe it as an isotropic, nearly incompressible hyperelastic material. Hyperelastic materials have J-shaped stress-strain curves and have large elastic deformation when loaded [80]. The stress-strain ($\sigma_1 - \varepsilon_1$) relationship of a hyperelastic material is derived from a strain energy density function, whereby the derivative of this function with respect to strain in the material is a measure of the materials stress.

From experimental compression tests carried out by Brown et al. [80] at different strain rates, it was found that Mooney-Rivlin strain energy density function (W) best fit the experimental results from these different tests. The tests were carried out at strain rates of $0.1s^{-1}$ and $0.025s^{-1}$. Where a strain rate of $0.025s^{-1}$ simulated a below impact loading velocity (cartilage behaviour is independent of fluid exudation) and $0.1s^{-1}$ simulates an impact condition (deformation is controlled by the exudation of fluid).

The Mooney-Rivlin strain energy density function (W) is:

$$W = C_1(\bar{I}_1 - 3) + C_2(\bar{I}_2 - 3) + D_1(\varepsilon_1^{1-2\nu} - 1)^2 \tag{2.2}$$

where C_1 and C_2 are material constants that characterise the deviatoric deformation of

the material. D_1 is the material incompressibility parameter and ν is the Poisson's ratio of the cartilage.

The normal stress (σ_1) of the material is therefore:

$$\sigma_1 = \frac{4(1+\nu)}{3}\varepsilon_1^{-(5+2\nu)/3}(\varepsilon_1^{2+2\nu}-1)(C_1+C_2\varepsilon_1^{-2(1+\nu)/3})+2D_1(1-2\nu)\varepsilon_1^{-2\nu}(\varepsilon_1^{1-2\nu}-1) \quad (2.3)$$

A wide range of linear elastic material properties of cartilage have been found in the literature (listed in table 2.6). For the modelling purposes of this thesis both linear elastic and hyperelastic material models were considered.

Reference	Anatomical terms	Young's Modulus (MPa)	Poison's ratio	Density (g/cm^3)	Thickness (mm)
Guo et al. [27]	Wrist	10	0.45		1
Carrigan [25]	Wrist	10	0.3		1
Troy and Grabiner [70]	Wrist	10	0.1		2.5
Troy and Grabiner [16]	Wrist	48	0.49		2.5
Anderson [28]	Wrist	10	0.45		
Oda et al. [24]	Wrist	5	0.49		
LeDoux [22]	Wrist	15			
Miyake [23]	Wrist	5	0.49		
Pistoia [81]	Wrist	1	0.49		
Cheug [71]	Foot	1	0.4		
Li and Lopez [82]	Knees	3.5-10	0.05-0.49		
Jost [52]	Costal cartilage	2500	0.3	2.5	
	Intervertebral cartilage	500-700	0.3	2.0	
Gislason [29]	Wrist	10MPa	0.4	1.1	
Range		1-2500 MPa	0.1 -0.49	1.1	1-2.5

Table 2.6: Summary of linear elastic material properties of cartilage.

2.9.4 Ligaments

Ligaments attach articulating bones to one another across a joint. Their main function is to resist tensile forces. These tensile forces are caused by muscular contraction or forces tending to displace the joint [38]. The main constituent of ligaments are collagen fibres. These fibres form groups called fascicles, the fascicles are in turn enclosed in a tough connective tissue sheath forming the ligament [59]. Details of the anatomy of ligaments of the wrist is given in section 2.3.3.

Mechanical ligament properties

The abundance of collagen fibres within the ligament tissue give a ligament its stress-strain behaviour which matches that of collagen fibres (figure 2.50) [47]. The toe region of the curve is due to the tension applied to the ligament that causes a gradual flattening out of the crimped collagen fibres. At these low stress ranges ligaments work to guide the bones through their normal movement. The linear region of the curve corresponds to the whole matrix of the ligament being under stress. Under these stresses the ligaments become stiffer and thereby provide more resistance to increasing deformations. It is assumed that such stiffening protects the joint [59]. The stress-strain behaviour of a ligament is also strain rate dependent as shown in figure 2.55.

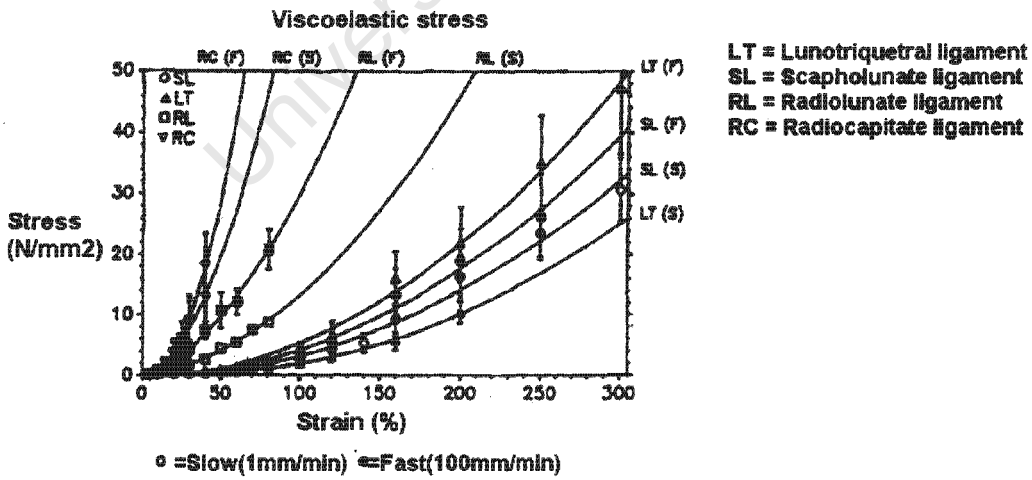

Figure 2.55: A stress-strain curve for a selection of ligaments of the wrist tested under different loading rates [83].

FE-modeling of ligaments

The most common way to model ligaments in FE-models of the wrist, are as non-linear tension only spring elements by connecting the corresponding insertion sites [25, 26, 70, 27, 29, 84]. A schematic of the different non-linear stress-strain definitions used by these various authors is presented in figure 2.56.

Carrigan et al. [25] and Troy et al. [26] described the non-linear behaviour by a parabolic toe region below 2% strain, a linear region beyond 5% strain and for strains greater than this a linear region with a ten fold increase in stiffness. Troy and Grabiner [70] modelled their ligaments in the same manner, however they prestrained the palmar ligaments to 2% to account for wrist extension. Guo et al. [27] specified a linear stiffness for strains under 5% and for strain beyond 5%, the specified linear stiffness was increased by a factor of 10. The non-linear ligament definition for the work conducted by Gislason et al. [29] was based on an equation derived from experimental results of Logan and Nowark [83], equation 2.4. The definition involves a non-linear toe region up to 15% strain (ε_{ref}) and a linear relationship following this. The actual constants used for the parabolic behaviour was not defined in any of the above mentioned cases. The model used by Gislason et al. [29] was not based on the individual ligament stiffness values, instead it was based on constants. Different constants would be required for each ligament. Therefore, none of these ligament behaviours involving parabolic toe regions could be directly recreated for the modelling purposes of this work. The load-deflection behaviour for the ligament in the Fischli [84] model was composed of a single function (equation 2.5) that described the stiffness variation with increasing strain behaviour. This function (equation 2.5) contained a linear and exponential function superimposed, hence enabling the parabolic toe region and the linear region to be described by one function. This function (equation 2.5) and that of Guo et al. [27] were chosen to be used in the model created in this study. Table 2.7 contains a summary of the actual wrist ligaments chosen for this thesis and the data needed for the modelling purposes of each of the chosen ligaments.

$$\begin{aligned} F &= \frac{a}{2\varepsilon_{ref}}\varepsilon^2 \qquad 0 \leq \varepsilon \leq \varepsilon_{ref} \\ &= a\varepsilon + b \qquad\quad \varepsilon > \varepsilon_{ref} \end{aligned} \tag{2.4}$$

Where a and b are constants and f is the ligament force.

$$f(\varepsilon) = k.l_0.(\varepsilon \quad 0.03) - 0.03k.l_0.exp\left(-\frac{\varepsilon}{0.03}\right) \tag{2.5}$$

Where k is the ligament stiffness, ε is ligament strain and l_o is the original ligament length.

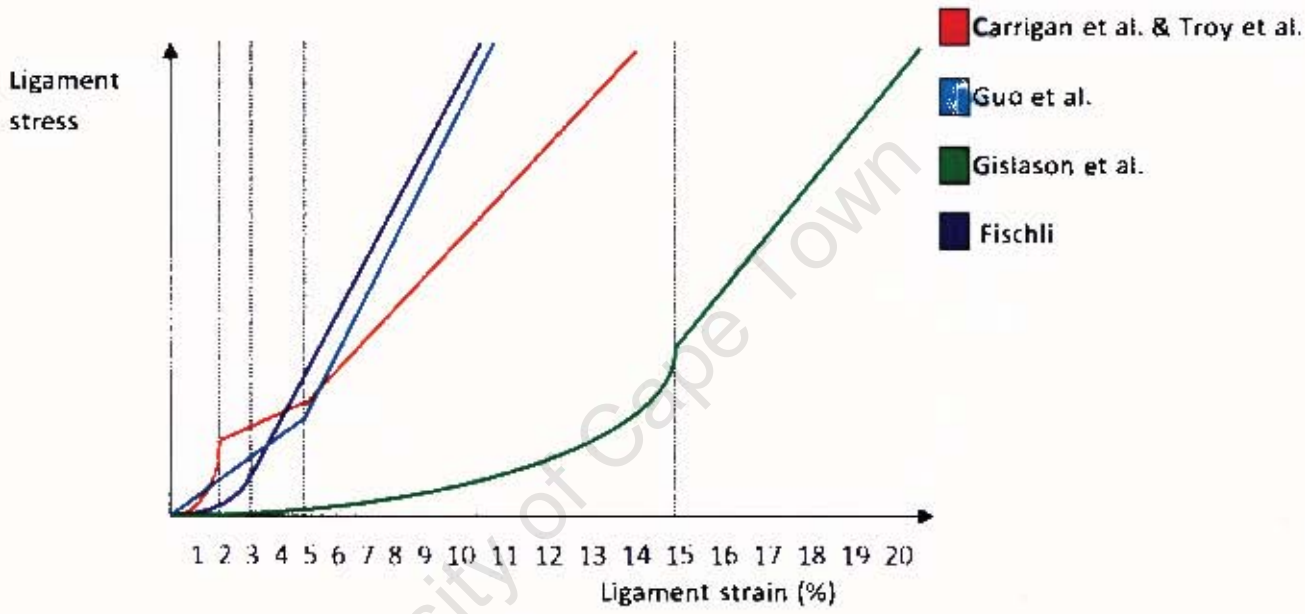

Figure 2.56: A schematic of the elastic stress-strain behaviours for ligaments of the wrist used in FE-models from Carrigan et al. [25], Troy et al. [16] , Guo et al. [27] , Gislason et al. [29] and Fischli [84].

Number in figure 2.12	Origin	Insertion	Stiffness (N/mm^-1)	Original length (mm) [84]
2	Radius	Scaphoid	10 [84]	13.5
9	Scaphoid	Lunate	230 [32]	3.3
10	Lunate	Triquetrum	350 [32]	4.3
11	Capitate	Scaphoid	40 [32]	7.2
14	Capitate	Triquetrum	120 [84]	13.3
17	Capitate	Hamate	325 [32]	7.6
	Capitate	Trapezium	300 [32]	12.1
12	Scaphoid	Trapezium	150 [32]	4
	Carpals	Metacarpals	75 [32]	7.6
15	Triquetrum	Hamate	200 [32]	5.1
	Lunate	Hamate	110 [84]	10.1
	Lunate	Capitate	110 [84]	10
16	Capitate	Trapezoid	300 [32]	3.8
	Trapezoid	Trapezium	110 [84]	7.5
4	Radius	Lunate	75 [32]	11.8

Table 2.7: Summary of the properties of ligaments of the wrist modelled in this thesis.

Chapter 3

Development of the finite element model of the wrist joint

This chapter deals with the development of two validated three-dimensional finite element models of the wrist joint. The modelling was carried out using ABAQUS/CAE (v. 6.8-2, Simulia), a general purpose finite element software. FE-modelling of the wrist is complex due to the complexity of the; materials, structure and mechanics. The load transfer characteristics through the carpo-metacarpal, intercarpal and distal radio-carpal joints were modelled. Two models were developed, a **Geometrically Simplified Model (GSM)** and an **Accurate Bone Geometry Model (ABGM)**. The GSM was validated and the material and structural parameters were verified. The parameters that lead to the most realistic solutions were identified. These parameters were then combined with accurate bone geometry to form the ABGM. Section 2.9 discussed the material properties of the biological tissues used in the modelling process. It was decided not to include the active action of muscles in both these models as cadaveric experimental work was used for the validation process and their incorporation would cause added complexity to the modelling.

The GSM, created from the geometric approximation of wrist bones, was used to determine the effects of different modelling parameters (material properties, ligament definitions and bone constrainment methods) on the contact and stress output variables. A static analysis involving the model being loaded under known conditions from experimental work presented in the literature, was carried out. This process was used to validate the model and to verify which of the previously mentioned model parameters gave the most

realistic results. The validation process is described in chapter 4. The ABGM was created from accurate bone geometry and material properties derived from a subject's CT scan (Appendix D). These were then incorporated into the GSM with the parameters that best fit the experimental validation data. The ABGM was then validated under physiological loads.

3.1 Geometry acquisition for the Geometrically Simplified Model

A half symmetry geometrically simplified model of the wrist joint was created. It involved the metacarpals, carpals and radius bone, shown in figure 3.1. The symmetry plane lies about the anterior posterior axis, therefore this model does not have a distinction between the palmar and dorsal aspects of the hand. This model was simplified in this manner to decrease the run time and complexity of the simulation. The geometry for the computational model was obtained from measurements taken off a human skeleton at the Department of Anatomy at the University of Cape Town. The bones sizes used are described in figures (A.1- A.5) in Appendix A. These measurements were compared with literature carpal bone sizes. The volumes of the scaphoid and lunate compare well to average bone volumes from work by Crisco et al. [85], shown in table A.1 of appendix A.

The geometry of the radius was derived from the idealised geometry used by Pietruskzczak et al. [37]. This geometry had no defined age or gender and was based on published images and spiral CT scans of radii specimens. The radial tilt used in the model is 20^0 [39]. A palmar tilt was not modelled in the GSM. Pietruskzczak et al. [37] results showed the typical Colles' fractures produced to be symmetrical about the dorsal palmar axis even though a tilt was included in their model (figure 2.40). Only the distal end of the radius was modelled as this was the region where a Colles' fracture occurs, section 2.8.3. These model simplifications were carried out to decrease the run time of the model.

It was decided not to include the ulna in the model as it does not directly contact the carpal bones or provide any direct structural support to the carpus [47]. The ulna provides a muscle attachment site and has not been found to be injured in a significant number of cases during fall event studies presented in the literature review, section 2.4. The pisiform bone was also not included as it is a sesamoid bone and its surrounding tendon was not modeled.

(a) Palmar view of wrist bones

(b) Geometric approximation model

Figure 3.1: Diagram of the bones used in the Geometrically Simplified Model.

3.2 Materials of the Geometrically Simplified Model

Each bone within the model had cortical and cancellous bone, and cartilage material properties assigned to them (figure 3.2). For the radius a cartilage thickness of 0.9mm was created [27, 25]. The cortical bone of the radius was modelled as shown in figure 3.3 [37]. For the carpal and metacarpal bones a cortical shell of 0.3mm was created around a cancellous core, these values were chosen based on the size of the thinnest region of cortical bone in the radius. The cortical shell of the carpal bones were surrounded by cartilage with a thickness of 0.3mm. The metacarpals have a cartilage thickness of 0.57mm for the regions of the bone that contacted the carpal bones.

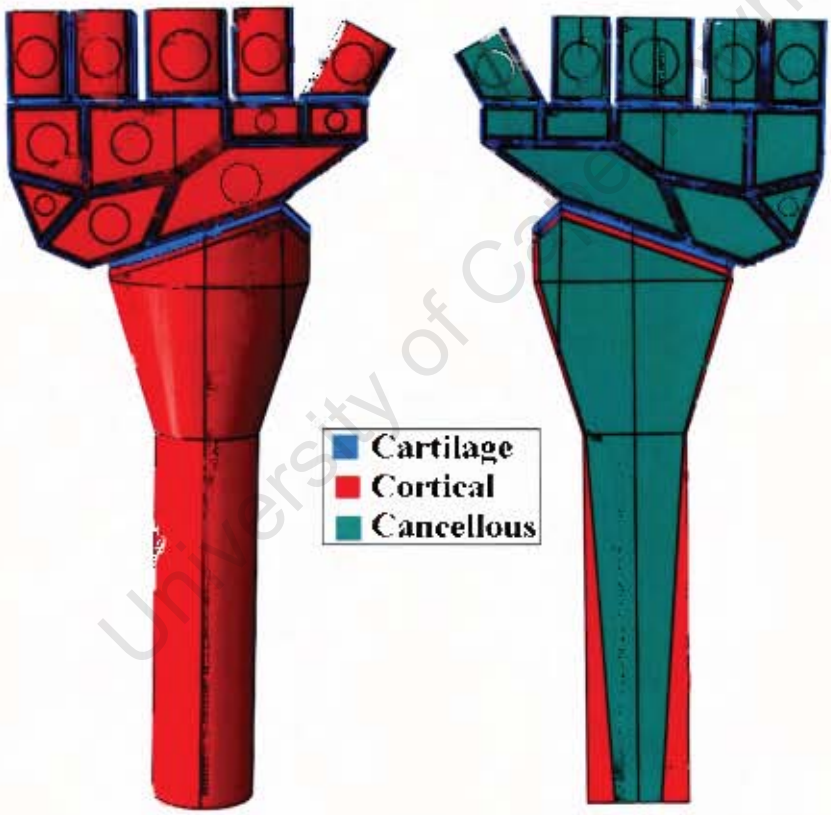

Figure 3.2: Material regions of the GSM.

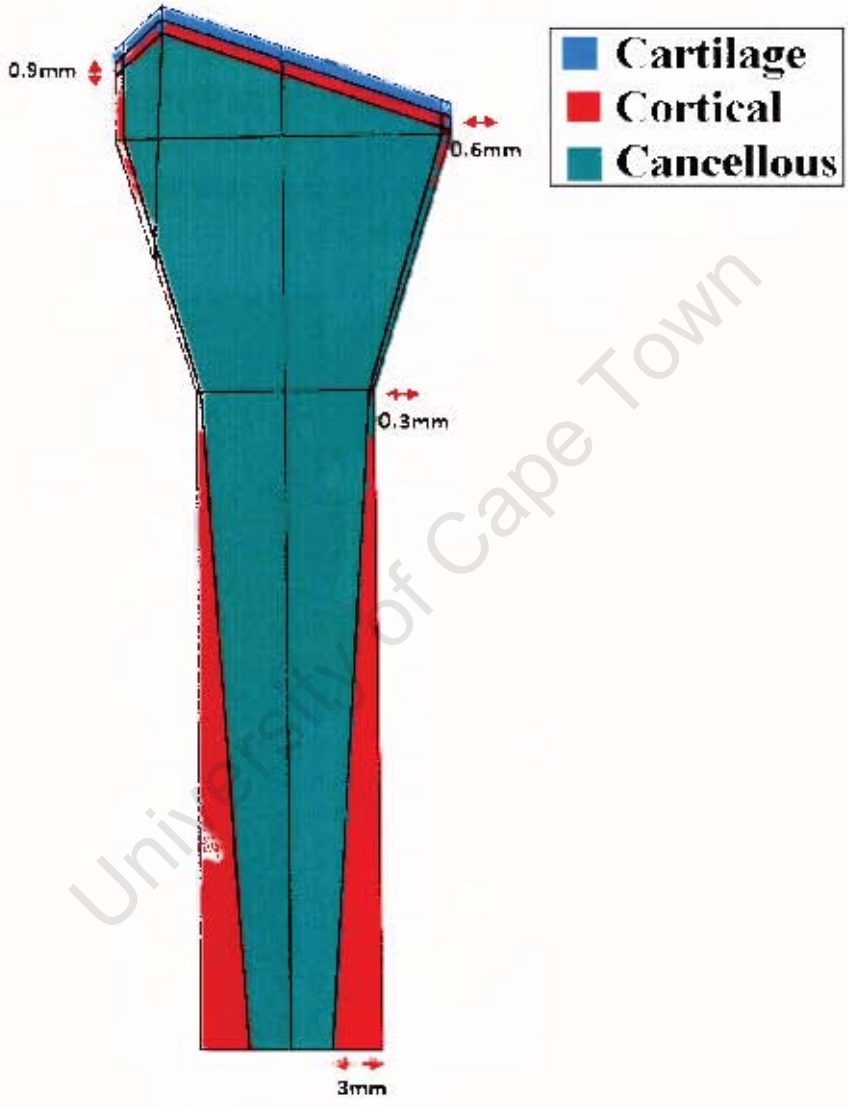

Figure 3.3: Material regions of the radius.

3.3 Acquisition of real bone geometry, mesh and material properties for the Accurate Bone Geometry Model

The same bones modelled in the GSM were used for this model (metacarpals, carpals and the radius). The bones were reconstructed three-dimensionally, using a series of computer tomography (CT) scans of a wrist joint. CT scan data sets are frequently used as a reference for the creation of biomechanical models of the wrist [27, 16, 25] and other body regions [82, 51].

Bone solid geometry is created by extracting the edges contours from CT images with image segmentation software. Details of the CT scan data set used in the creation of the ABGM is given in Appendix D.

Attempt at bone geometry extraction in MATLAB

An initial attempt to extract the surface geometry was carried out using the Image Processing Toolbox in MATLAB. Each CT scan image is composed of 512 x 512 pixels. The images where first converted to a format readable by Matlab, using the *imread* command. Each image was interpreted by Matlab as a 512 x 512 matrix. Each entry within the matrix corresponds to the colour of the pixel and the position of the entry corresponds to the position of the pixel within the row column index. The image was cropped so that only the region containing the bone geometry remained. This colour image was converted to a grayscale image, where the colour of each pixel in the image is assigned a value in the matrix between 0 and 1. The grayscale image was used to create a purely black and white image, using threshholding. Thresholding is a technique used to distinguish areas of bone tissue. Thresholding works by changing all the colours that are darker than the threshold value chosen to black (background). The remaining pixels are set to white (bone). After the image was thresholded, the edges of the bones were detected. The bone edge lines occur where the colour changes from black (background) to white (bone). The bone edges were extracted using an edge detection technique. The algorithm works by taking the derivative of the matrix values in matrix space, therefore detecting the colour change. An example of an image that was processed in this manner is shown in figure 3.4.

From the processed image (figure 3.4) it can be seen that the distinction between some of the carpal bones and the background was not detected. In most bone types, the segmentation of bones seem to be a relatively straight forward task using this method.

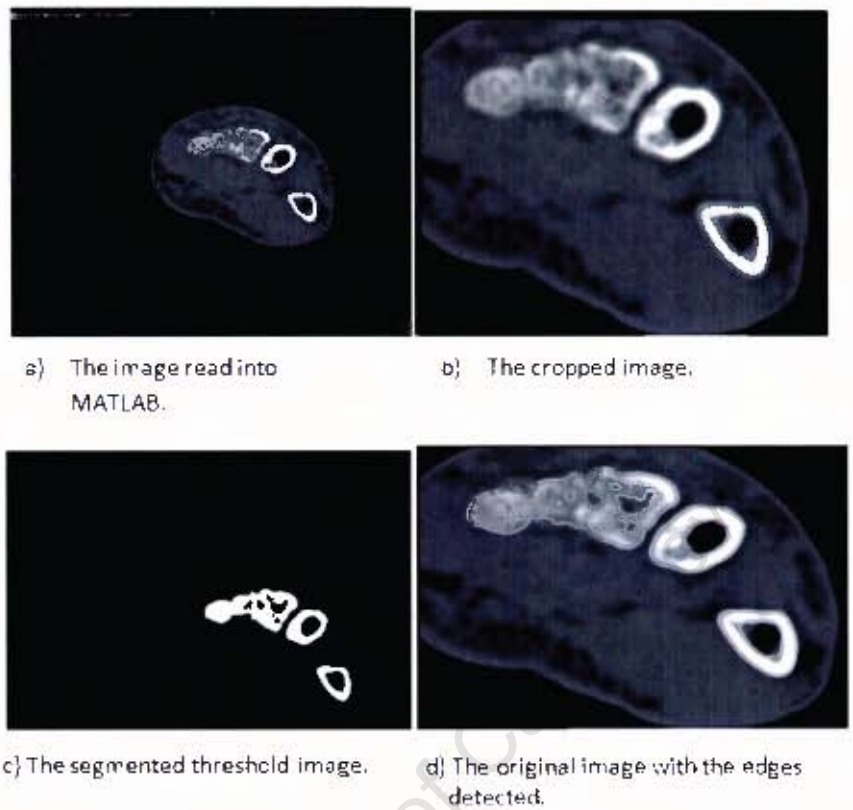

Figure 3.4: Images processed in Matlab.

This is not the case for carpal bones due to their irregular shape, with small inter-bone distances relative to the resolution of the CT imaging. Carpal bones are composed of a cortical shell with a cancellous core. Cortical bone is denser than cancellous bone. With CT imaging cortical bone appears brighter and smooth, whilst cancellous bone appears darker and textured. Due to the close space of the carpal bones and the inherent blur of the CT images, the inter-bone space often appears bright, substantially reducing the boundary contrast at these points. Blood vessels also resemble the background which creates gaps in the cortical shell. Another problem is that cancellous bone regions have both bone-like and tissue-like intensities. Therefore, this method of extraction was rendered unsuitable for the carpal bones.

Geometry extraction using Mimics software

The three-dimensional reconstruction from the scan data was carried out using commercial segmentation software called MIMICS (Materialise). This software was used to visualise, segment and render a three-dimensional mesh from the scan data that could be imported into ABAQUS.

The bone geometry was created by initially identifying the bone tissue on the CT scan, using thresholding. Each pixel within the image has a certain intensity called Hounsfield units (HU). Thresholding of bone tissue was carried out in this case by specifying the range of Hounsfield units that correspond to the intensity of bone tissue. This intensity included both cancellous and cortical bone tissue.

Once the bone tissue boundary was identified, a segmentation mask was created. A segmentation mask contains all the pixels that have HU within the threshold for bone tissue. Individual segmentation masks are created for each bone (figure 3.5). The same problems were encountered using this method as was with using Matlab, whereby the distinction between the individual carpal bones was difficult. In this case however segmentation masks were manually edited, to create separate segmentation masks for each bone and to remove artefact. The segmentation masks were then used to create 3-D surface volumes for each bone (figures 3.6 and 3.7). The software carried out this task by combining the masks for each individual bone in each slice of the scan, as seen in figure 3.6.

Figure 3.5: CT scan image with segmentation masks of each bone.

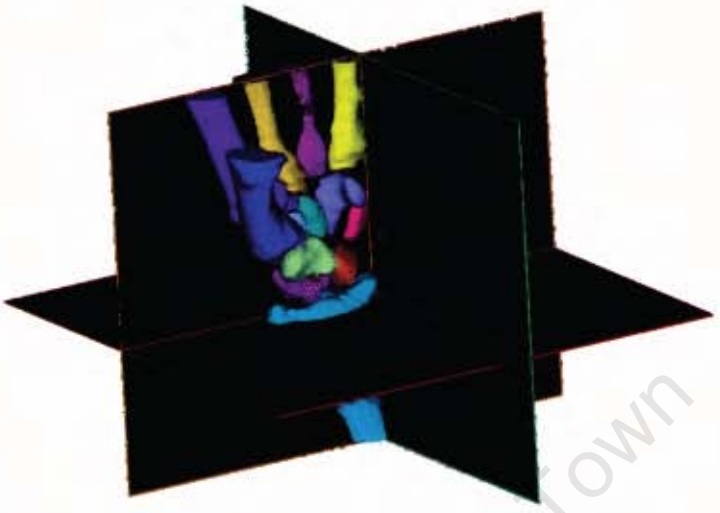

Figure 3.6: 3-D Surface volumes of each bone created from CT-scan data in three different planes.

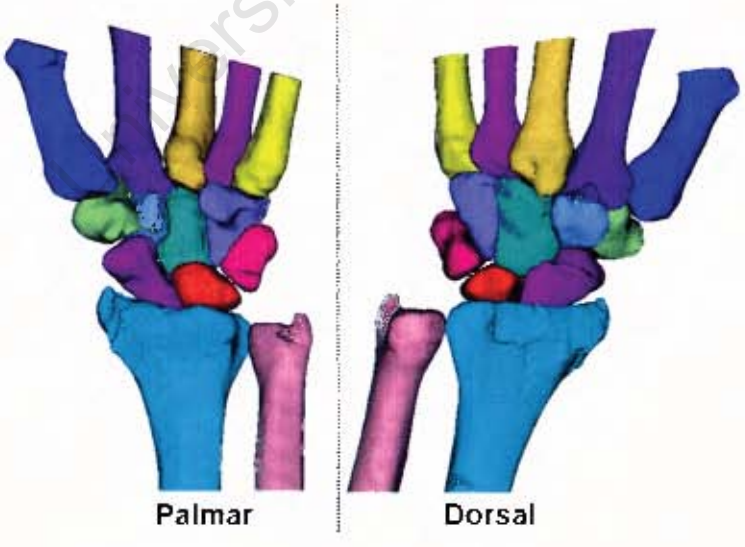

Figure 3.7: 3-D Surface volumes of each bone.

Meshing using MIMICS

The 3-D surface volumes were used to create a surface mesh in MIMICS. The mesh consisted of linear triangular elements. In order for the mesh to be used for FEM purposes, bad quality triangles need to be identified. This was carried out by using various shape parameters.

One shape parameter considered was the height/base ratio. This measures the ratio between the height and the base of the triangle. A perfectly equilateral triangle has a ratio of 1.73. A ratio of 0.4 was chosen and triangles with ratios below this value were removed. The edge length was also used as a parameter, whereby only triangles with edge lengths below 1mm were retained.

After the mesh was optimised the surface mesh was converted into a volume mesh. The linear triangular elements were converted into solid tetrahedral elements. The orphan bone mesh (figure 3.8) was imported into ABAQUS. The orphan mesh consists of node and element definitions along with the type of element assigned. Further details about meshing are given in section 3.8.

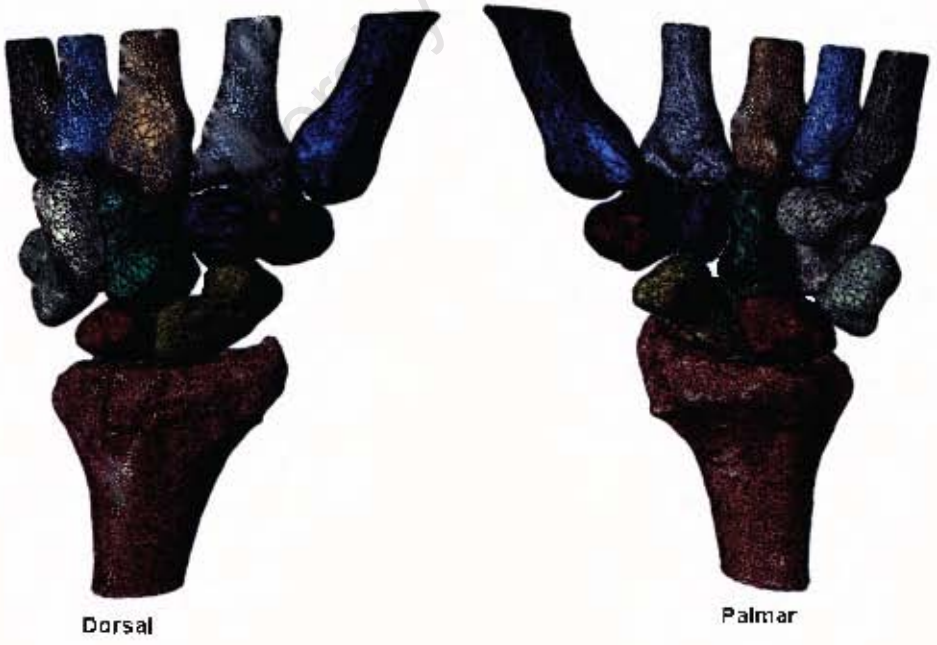

Figure 3.8: Bone mesh imported into Abaqus.

Material assignment using MIMICS

The material properties for each bone were assigned based on the Hounsfield units. Each element within the meshed volume was assigned an individual density and Young's modulus value (figure 3.9). Seven material properties where defined, described in table 3.1.

Figure 3.9: Mesh showing the different material properties for each element within bones.

Number	Apparent density (Kg/m3)	Young's Modulus (MPa)
1	790	2671
2	1023	4487
3	1255	6774
4	1488	9534
5	1721	12766
6	1953	16473
7	2186	20653

Table 3.1: Material property definitions used in the ABGM.

Apparent density was based on its relation to the Hounsfield units of each pixel (discussed in section 2.9). Young's modulus (E) was determined from its relationship with the apparent density (ρ) shown in the equations in 3.1 [66].

$$\begin{aligned} \rho &= 1.067HU + 131 \\ E &= 0.004\rho^{2.01} \end{aligned} \tag{3.1}$$

Units for E are MPa and ρ is Kg/m^3.

CT scan data does not give a clear description of the articular cartilage present covering the bones. To account for the presence of cartilage in the model, an exponential contact pressure-cartilage thickness relationship was defined for the regions of bones where cartilage and cartilage-cartilage contact was thought to occur. This relation is further discussed in section 3.5. This clearance is the approximate cartilage thickness, which had been obtained by measuring the distances between the bones and taking an average value of these distances.

3.4 Analysis Step

Abaqus/Standard was used to perform a static implicit analysis. Static analysis was carried out for both models due to the experimental work used to validate the models having static applied loads. The analysis was composed of an initial and a load application step. During the initial step contact as described in section 3.5 and boundary conditions as described in section 3.7 were defined. The load application step involves the displacement response of each node making up the entire system being calculated, after a load of known magnitude is applied (section 3.7). During an FE-analysis the geometry of the model is broken down into elements. Each element within the system can be thought of as a spring (equation 4.1) between a set of nodes (section 4.1). Since an implicit analysis was carried out, the equilibrium equations needed to be solved for each node of the system simultaneously to obtain the displacements at all the nodes. The equilibrium equations are solved once the external applied load is in equilibrium with the internally generated load.

Each step of the analysis is composed of time increments during which the solver iterates to solve the equilibrium equation. With each iteration, the solver computes the force residual, which is the difference between the applied load and the internal load [86]. This force residual is compared to the force residual tolerance value that is set at 5% of the average force in the structure, averaged over time. At each time increment the difference between the applied and internal loads are checked. When this difference is below the tolerance value, a solution is output.

Linear versus non-linear analysis

The decision of whether to conduct a linear or non-linear analysis was based on the material definition used for cartilage. An analysis can be defined as a 'small-displacement' or 'large-displacement' analysis [86]. A linear analysis is carried out during a small-displacement analysis. During a linear analysis there is a linear relationship between the applied load and the response of the system. This type of analysis is carried out for models where linear elastic material properties were defined for cartilage. In a linear analysis the flexibility of the model needs only to be calculated once. The flexibility is calculated by assembling the stiffness matrix and inverting it. The initial flexibility is multiplied by the applied load to calculate the displacement for the load.

A large-displacement or non-linear analysis was carried out for models that included

hyperelastic (i.e. non-linear) material properties for cartilage. A non-linear analysis is one in which the model's stiffness changes as it deforms. In a non-linear analysis the stiffness is dependent on displacement of the structure, therefore in these cases the flexibility needs to be calculated at increasing applied loads. During these types of analysis elements distort from there original shape as load increases, element calculations involve the nodal positions of the distorted elements. For the linear case the nodal positions are formulated using their original nodal coordinates.

3.5 Contact and Friction

This section contains a general description of contact and friction models used within the GSM and ABGM. Bone surfaces that are in contact are covered by articular cartilage. Contact needed to be defined due to the wrist joint being composed of so many contacting bones. The areas and contact pressures of these contacting surfaces needed to be calculated. When two bone surfaces come into contact a force normal to the two contacting surfaces is generated. The sliding of the two bodies in contact is resisted by shear forces between the two bodies due to friction. Therefore, the interaction between surfaces consists of two components: one normal to the surfaces (contact force) and one tangential to the surfaces (friction). During the analysis a system needs to be put in place that is able to detect when two surfaces are in contact and apply the contact constraints appropriately. Abaqus/Standard has many different contact formulations based on a choice of; a contact discretization, a contact tracking approach and the assignment of 'master' and 'slave' surfaces to the contact surfaces.

3.5.1 Contact Tracking approach and discretization

The contact tracking determines when two surfaces are in contact. There are two methods in ABAQUS/standard for carrying this out. These two approaches account for the motion of the two contacting surfaces relative to one and other. These are the finite-sliding tracking approach and small-sliding tracking approach [86]. The finite-sliding tracking approach was used for both the GSM and ABGM models.

The small-sliding tracking approach was inappropriate due to it assuming that there will be very little sliding of one surface along another. The contact area for this approach is calculated in the input file pre-processor from the undeformed shape of the model, therefore this value does not change throughout the analysis and the contact pressures are calculated according to this contact area. Contact area is a model validation criteria, hence it needs to be determined for different loads applied. The finite-sliding tracking approach allows for arbitrary relative sliding, separation and rotation of the contacting surfaces. The contact pressures and areas are calculated according to the deformed shape of the model.

A contact discretization defines which regions of surfaces in contact interact. There are two different types of contact discretization. These are a surface-surface and a node-

surface discretization [86]. The former involves surfaces interacting with each other, the later involves individual nodes on one surface making contact with a group of nodes on the other. For both GSM and ABGM the surface-surface discretization was chosen. This decision was due to this method taking the shape of the surfaces in contact into account, producing a smoother contact pressure profile.

3.5.2 Contact pressure-overclosure relation

Behaviour normal to the surfaces

The distance separating two surfaces in the model is called the clearance. When there is penetration of the two surfaces, the distance of penetration is called the overclosure. ABAQUS uses this clearence/overclosure relationship to decide when and to what degree to enforce contact constraints. Abaqus has two contact relationships; 'hard' and 'softened' contact [86]. Hard contact was used for the GSM and softened contact was used for the ABGM. The difference between the two contact relationships is the manner in which they related the contact pressure to the clearance/overclosure distance. The relationship for hard and softened contact is shown in figures 3.10 and 3.11 respectively. The hard contact relation in figure 3.10 shows that when surfaces are in contact (clearance = 0), contact pressure is transmitted between the surfaces. No penetration of the surfaces into each other is allowed.

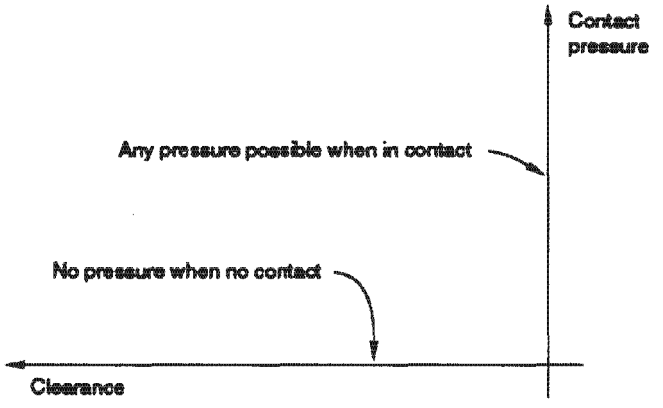

Figure 3.10: The pressure-overclosure-relationship for hard contact [86].

A softened contact relation involves the contact pressure being an exponential function of the clearance (figure 3.11 and equation 3.2). The surfaces begin to transmit contact pressure once the clearance between them reduces to c_0. The contact pressure transmitted between the surfaces increases exponentially as the clearance continues to diminish. This model was used in the ABGM to define the contact response between the articular cartilage surfaces that come into contact. Since the actual geometry of cartilage was not present in the ABGM, the effect of the cartilage on contact pressure needed to be defined. The clearance distance represents the distance between the bones. In reality this space is filled with articular cartilage that covers the bones. The magnitude of the clearance in different regions was measured from the CT-scan. An example of the measurement of the approximate thickness of the cartilage covering a carpal bone and the radius is shown in figure 3.12. The average chosen relationship was defined with C_o=3mm and P_o=4MPa, these values (contact pressure-clearance relationship for articular cartilage) were consistent with the work from Laurian et al. [51].

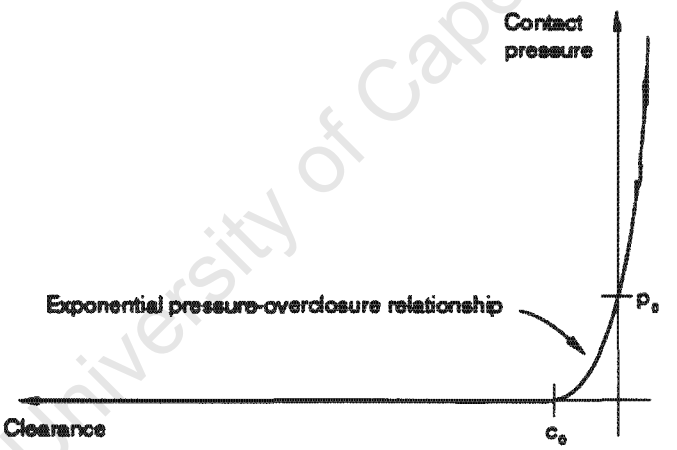

Figure 3.11: The contact pressure-overclosure relationship for softened contact [86]

$$P = 0 \qquad h \leq -c$$
$$P = \frac{P^0}{(\exp(1)-1)}[(\frac{h}{c}+1)((\frac{h}{c}+1)-1)] \qquad h > -c \tag{3.2}$$

Where, P^0, is the pressure when the clearance, h, is zero.

Figure 3.12: An example of the measurement of the approximate thickness of cartilage between the radius and the carpal bones.

Frictional models

Friction was defined for both the GSM and ABGM. A Coulomb friction model is used to relate the normal force and the frictional shear forces between surfaces in contact. These shear forces resist the sliding of the contacting surfaces. Two contacting surfaces can carry shear stresses up to a critical magnitude across their interface before they start sliding relative to one another, this state is known as sticking. The Coulomb friction model defines this critical shear stress (τ_{crit}) at which sliding of the surfaces starts as a fraction of the contact pressure (p) between the surface ($\tau_{crit} = p\mu$). The stick/slip calculations determine when a point on a surface transitions from sticking to slipping or from slipping to sticking. μ is known as the coefficient of friction. A low friction coefficient of $\mu = 0.003$ [59] was used for both models.

3.6 Modelling of ligaments

Ligaments connect two bones together, further details of their functions and anatomy are described in sections 2.3.3 and 2.9.4. A method to enforce this connection was achieved through using connector elements in ABAQUS (figures. 3.13 and 3.15). Axial connectors model axial linear elastic springs (equation 4.1). They provide connections between two nodes that act along the line connecting the nodes. The relative displacement is also along that line. The ligaments that connect the metacarpals to the carpals, the carpals to each other and the carpals to the radius were modeled.

The behaviour of the connector element was controlled by specifying a non-linear force-displacement relation based on the individual ligament's stiffness and original length. This stiffness and original length were determined from experimental work presented in the literature. The ligament properties and ligaments chosen to be modelled in the GSM and ABGM are summarised in table 2.7. The non-linear behaviour of these ligaments were described using force-deflection relations described by Gou et al. [27] and Fischli [84]. These relations have been called A and B respectively.

Some assumptions were made in terms of the ligament behaviour defined for certain ligaments. The ligaments that join the metacarpals to the carpal bones were all given the same stiffness and original length values. The scaphoid to trapezoid and scaphoid to trapezium ligaments were given the same definitions as well. For the ABGM the same ligaments and ligament properties were defined for the dorsal and palmar ligaments. The ligaments that connect the metacarpals together were modelled using link connectors. These connectors provide a pinned rigid link between the attached nodes, to keep the distance between them constant throughout the analysis. These constraints were applied instead of simply defining the behaviour of the intermetacarpal ligaments, due to these ligaments having very high stiffness values k$-200N/mm^{-1}$ [32], with unknown original lengths.

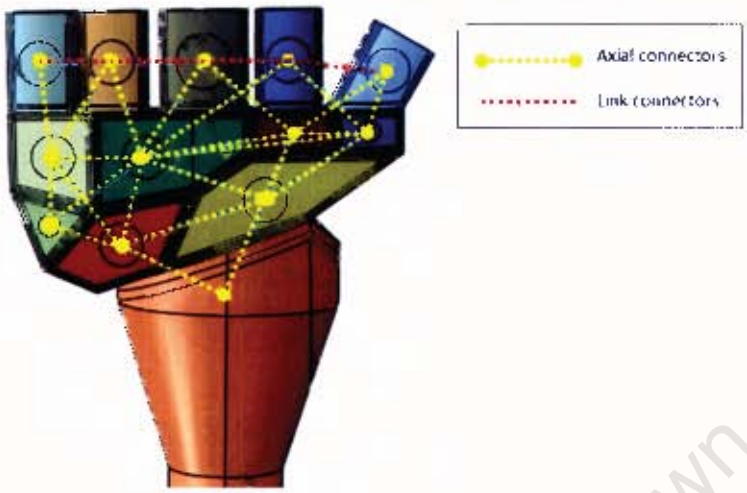

Figure 3.13: Diagram of connectors used to define the ligaments.

Coupling

Since the connector elements are only applied between two nodes a method of applying the same connectors to multiple nodes on the same bone need to be determined. This was done using coupling constraints, whereby a group of nodes on a surface of a bone (ligament attachment zone) were coupled to one reference node, shown in figure 3.14. Each of the carpal and metacarpal bones, surfaces were partitioned to yield a circular group of nodes. This was carried out on the dorsal and palmar surfaces for the ABGM. Where possible the ligament attachments were placed on regions where tuberosity (roughed ligament attachment sights) was identified on the bones. The coupling constraint was applied to these nodes. The same was carried out for the radius. A distributed coupling constrain is used whereby the motion of the nodes on the coupling surface are constrained in both rotational and translational degrees of freedom to the reference node. The constraint distributes the resultant of the forces on the coupling nodes as equivalent to forces of the reference node [86].

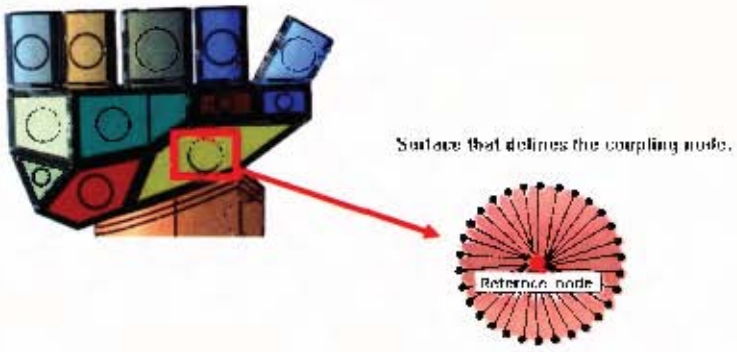

Figure 3.14: Diagram describing coupling of a reference point to a surface.

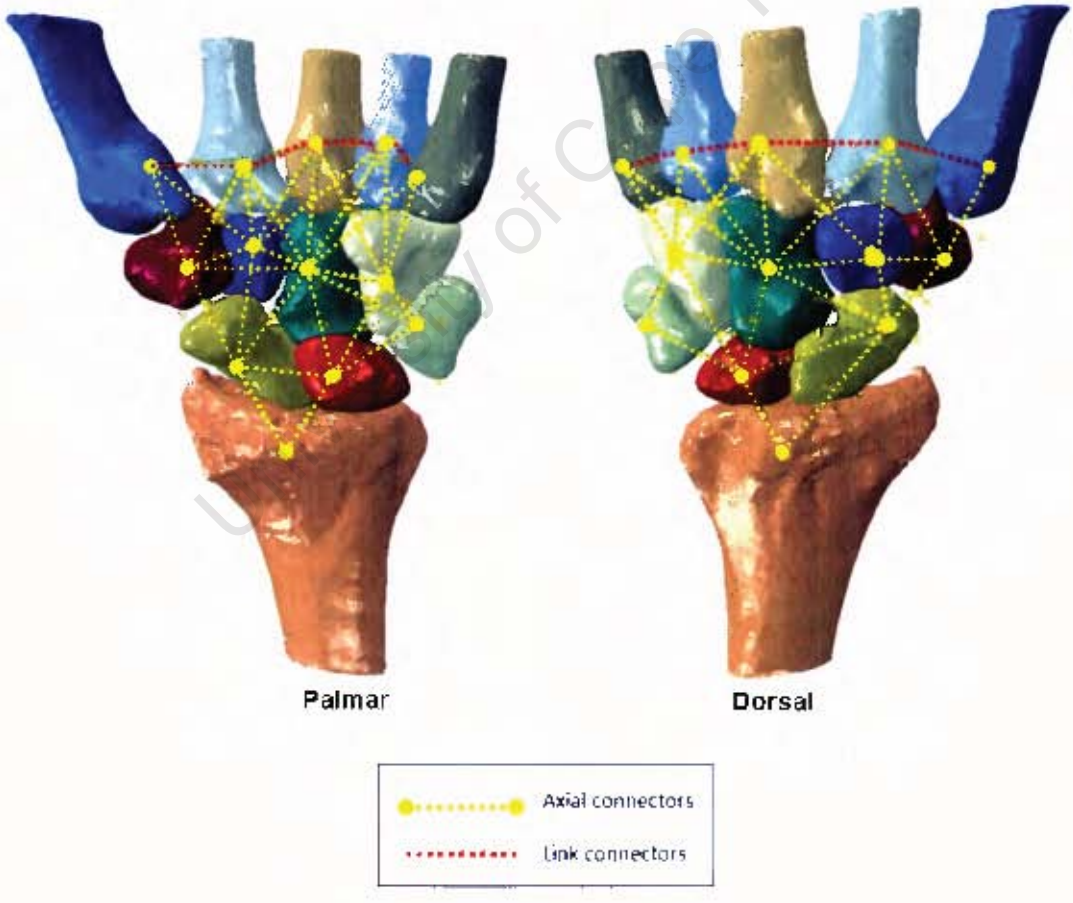

Figure 3.15: Accurate bone geometry model with ligament connectors.

3.7 Loading and Boundary conditions

The boundary conditions and loading applied to both the GSM and the ABGM are shown in figure 3.17. Cylindrical and Cartesian coordinate systems were defined for different regions of the models, these are described in figure 3.16.

3.7.1 Loading

To emulate the experimental work used for validation of the models, discussed in chapter 4, loads where applied to the model as pressure loads acting on the distal surface of the metacarpals. The loads were applied perpendicular to the joint surface of the radius, to be consistent with the validation experimental loading direction. This joint surface lies at twenty degrees to the horizontal for both the GSM and ABGM. The loads were applied in this direction for Mc2-5, with the exception of MC1 where the load was applied along its axis.

To achieve this loading configuration for the GSM the surface traction loading definition in ABAQUS was used for Mc2-5 (C in fig. 3.17) was used. For Mc1 (D in fig. 3.17) the load was applied along the axis of the bone due to its location and orientation relative to the joint. Application perpendicular to the joint would not have been a feasible option. For the ABGM's Mc2-5 (E in fig. 3.17) a Cartesian coordinate system was defined so that the load was applied along the x-direction. The same was carried out for Mc1 but for this case the load was applied along the y-direction (F in fig. 3.17).

3.7.2 Boundary conditions and loading

Non-physiological constraints where applied to both models to allow for solution convergence. The GSM was modelled as a half symmetry model. The symmetry plane was applied about the anterior-posterior axis, therefore making no distinction between palmar and dorsal surfaces.

The proximal surface of the radius of both the GSM (A in fig. 3.17) and the ABGM (G in fig. 3.17) was also constrained. A cylindrical coordinate system was defined such that the z-axis was along the axis of the radius and the radial-axis and theta-axis lay along the plane of the radius proximal surface. This constraint was applied to a reference point located and coupled to the proximal radius surfaces of the GSM and ABGM. This constraint was applied such that the proximal surface could not translate in the z-direction or the theta-direction. Only translation in the radial direction was allowed. This form of constraint allows the bone to undergo slight displacement in the circumferential direction, which occurs in human bones under loading.

The distal surface of the metacarpals, Mc1 (F in fig. 3.17) and Mc2-5 (E in fig. 3.17), were constrained in the ABGM. This constraint was applied through the reference points on the surfaces. The distal surfaces of the metacarpals were coupled to reference points. The constraint applied to these reference points only allows translation in the direction of the load.

Non-physiological constraints were applied to the carpal bones of the ABGM to allow solution convergence. The reason these constraints were needed was that the muscle and surrounding fascia on the joint was not modelled. Therefore the support provided by these structures was not present. Two different constrain methods were employed and the effects of each were studied in section 4.2.2. The first involved constraining the proximal carpal row and the second involved constraining a single node in the center of each carpal bone. The proximal row of the carpus; hamate, capitate, trapezoid and trapezium bones, have been found to act as a single unit [18]. Therefore the motion of the bones in this row was constrained. This constraint was applied to the surface nodes not involved in ligament connections to motion only in the direction of the load (Mc2-5). The second method involving all the carpal bones was the application of a constraint to a single node in the center of each bone. This node was connected to ground using a bushing connector. This connector allowed the displacement and torsional rotation of the node to be controlled by user defined spring and rotational stiffness values. The motion of the bones in the

direction of the load was not constrained in any manner. The values chosen were 150N-mm (translational stiffness) and 150N-mm per Radian (rotational stiffness). These values were chosen as they lead to solution convergence, decided after testing various smaller values.

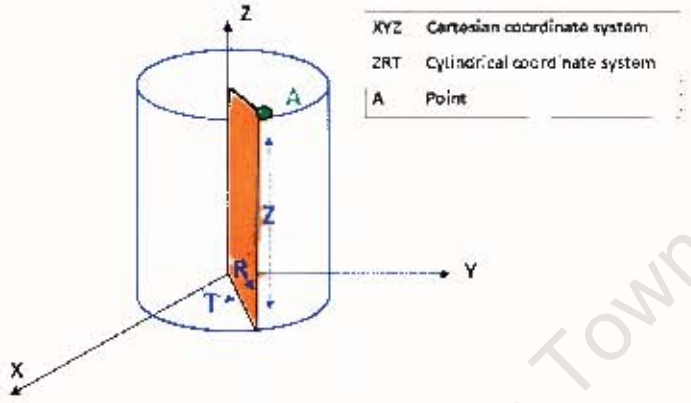

Figure 3.16: Schematic describing Cylindrical and Cartesian coordinate systems.

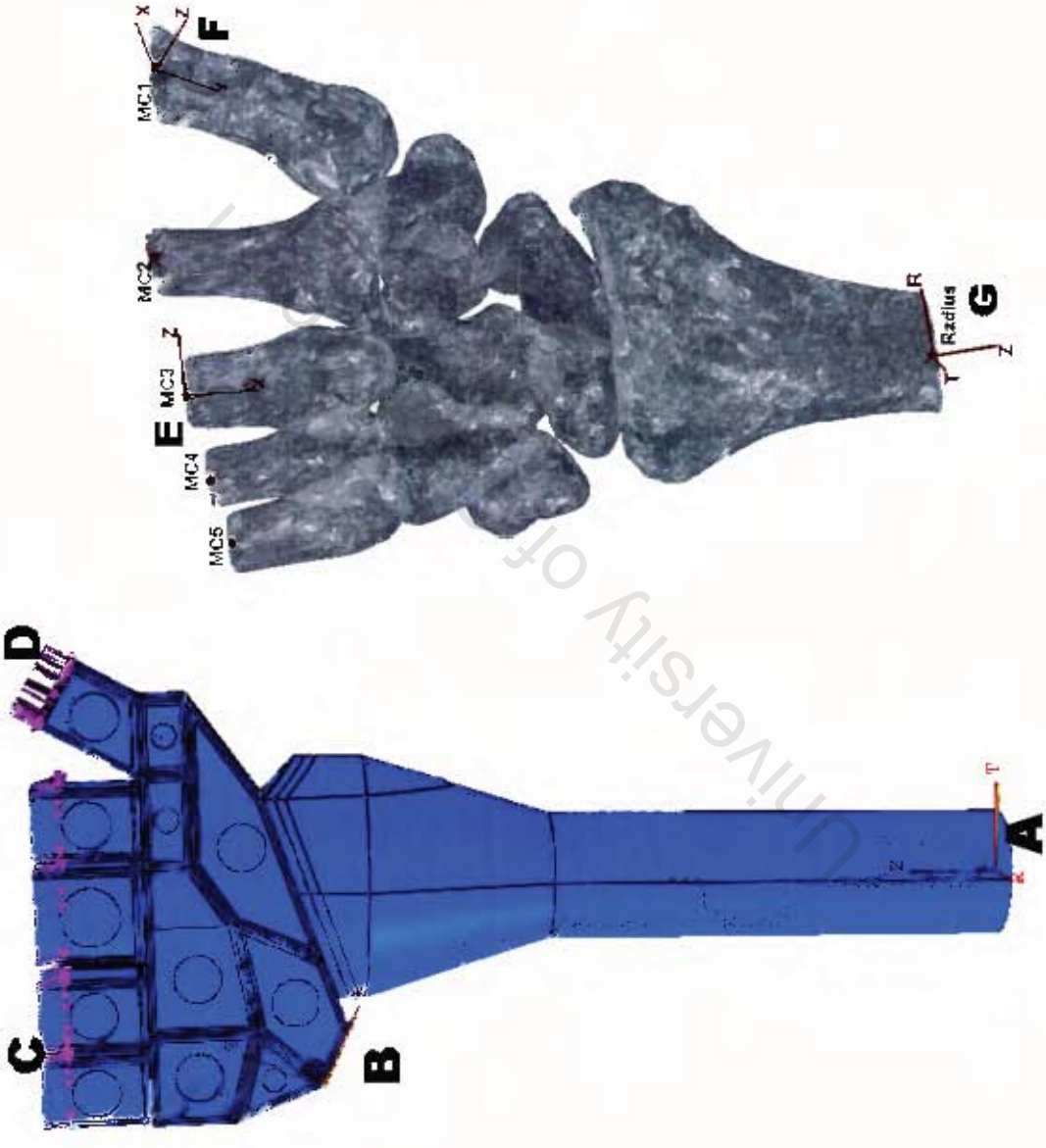

(a) GSM (b) ABGM

Figure 3.17: Loading, boundary conditions and coordinate systems.

TFCC

Due to the ulna and the TFCC not being modelled, the support provided by them was modelled in an indirect manner. Two methods were considered in the GSM and the method that caused the best fit of the validation results was used for the ABGM. The first method involved the lunate bone being constrained over the area that would have been in contact with the TFCC, using a coordinate system defined uniquely for it (B in fig. 3.17). Therefore not allowing motion along the z-direction.

The second method involved modelling the TFCC as an array of compressive springs, a similar method has been previously used by Anderson et al. [28]. For this method the beam on elastic foundation theory was used. This method works by defining an array of compressive springs of a defined stiffness over a defined area. The area defined was the surface of the lunate that would be in contact with the TFCC. A stiffness of $100N/mm^2$ was used to define the stiffness of TFCC [32] in both the GSM and the ABGM.

3.8 Mesh

During a FE-analysis the structure under consideration is broken into a finite number of elements. The collection of these elements refers to the mesh. The mesh factors that have an influence on the solution obtained are; the order of the element (linear or quadratic), the element formulation, and the level of integration.

For the GSM, hexagonal elements (C3D8) were used, with the exception of the distal regions of radius were tetrahedral elements (C3D4) were used. These elements were used due to the difficult geometry seen in Appendix B. For the ABGM the mesh consisting of tetrahedral elements was imported from MIMICS. The number and type of element for each bone of both models is summarised in tables 3.2 and 3.3.

Fully intergraded, linear elements were used for both the GSM and the ABGM, where linear elastic material properties were modelled. These elements use two integration points in each direction i.e. two Gauss points required to intergrate the polynomial terms in the element stiffness matrix [86]. The average element size chosen was 0.6mm for the GSM. The mesh density was varied between smaller values (element sizes 1.2-0.6mm) and the model outputs were found to converge at this mesh density (0.6mm).

C3D8 elements are fully intergraded hexagonal elements with eight nodes per element. C3D4 are fully intergraded tetrahedral 4 noded elements.Hybrid elements (C8D3H and C3D4H) were used when cartilage was modelled as a hyperelastic material. Due to the cartilage being modelled as nearly incompressible. Regular elements cannot be used due to the volume of the elements not changing during loading application, therefore the displacement of the nodes can not be used to calculate pressure stress. These hybrid elements have an additional degree of freedom that determines the pressure stress in the element directly.

Bone	Element type	Number of elements
Radius	C3D8	10586
	C3D4	98330
Scaphoid	C3D8	5700
Lunate	C3D8	3876
Triquetrum	C3D8	1416
Trapezium/Trapezoid	C3D8	1620
Capitate	C3D8	4620
Hamate	C3D8	3420
Metacarpal 1/2/4/5	C3D8	2255
Metacarpal 3	C3D8	3322

Table 3.2: Number and type of element for each bone in the GSM.

Bone	Number of elements (C3D4)
Radius	190346
Scaphoid	27700
Lunate	20136
Triquetrum	14583
Trapezium	25043
Trapezoid	18849
Capitate	35418
Hamate	29380
Metacarpal 1	6071
Metacarpal 2	6337
Metacarpal 3	5219
Metacarpal 4	3518
Metacarpal 5	3418

Table 3.3: Number and type of element for each bone in the ABGM.

Chapter 4

Validation and parameter verification of the wrist joint model

This chapter describes the process of validation and parameter verification of the wrist joint FE-models. The validation of a numeric model is a very important step in the model development. The validation process involved the biomechanical responses of these models (GSM and ABGM) being compared to literature experimental cadaveric and RBSM results from the literature.

For the validation procedure the model results were compared to multiple experiments, as a comparison to one experiment may lead to the model parameters being only valid for that one experiment. The results of cadaver tests are given in the form of experimental corridors as different cadavers subjected to the same load give a spread of different results. The ability of the model to simulate the cadaver tests can be determined by how closely the simulated response falls within the corridor defined by the experiments.

The basic steps involved in validating a numerical model and verifying its parameters are shown in figure 4.1. The feedback shown in the diagram is used to investigate the sensitivity of the model to modelling parameters and material properties of bone, cartilage and ligaments. This procedure is carried out to determine which combination of these parameters and properties gives results that best match the multiple experimental results.

Defining initial parameter values is the first part of the validation process. The problematic nature of material properties has been discussed in section 2.9. The range of material properties chosen to optimise the GSM are presented in tables 2.4, 2.5 and 2.6. Initial values were chosen from this range before the validation procedure. These values were then adjusted according to the model's response to find a configuration of model parameters that satisfies most of the experimental results.

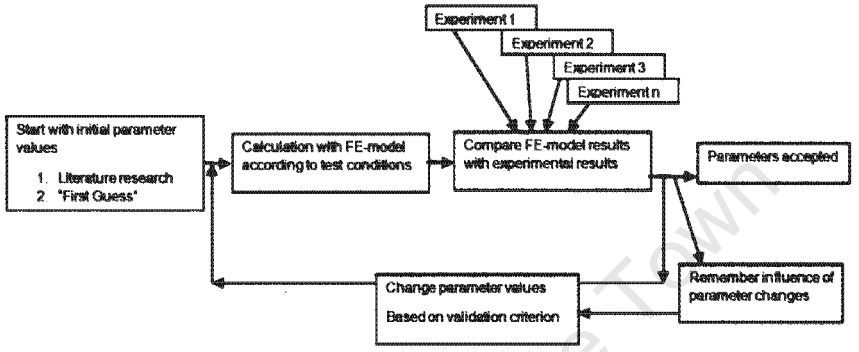

Figure 4.1: Diagram of the process of validating a FE-model [52].

The modelling parameters considered for the GSM were; the modeling of the TFCC, the difference between the two non-linear definitions for ligament stiffness and the difference between defining cartilage as a linear elastic or hyper elastic material. Once these parameters were verified, they were incorporated into the ABGM. For the ABGM the parameters looked at were the different methods in constraining the carpal bones motion discussed in section 3.7. The experimental work used for both models validation procedures is summarised in table 4.1. Further details about this experimental work are discussed in section 2.6. The simulation results used for comparison were:

- Maximum contact pressure on the radial articular surface compared to results from Veigas et al. [18, 87].
- The ligament behaviour compared with results from Horii et al. [33].
- Maximum contact pressure on the scaphoid and lunate to radius articulation, and ratio of maximum pressures compared with Schuind et al. [32], Horii et al. [33] and Blevens et al. [48].
- The articular contact pressure profile along the radius midline compared to work from Teurlings et al. [88].

- The ratio of contact area of the scaphoid and lunate on the radius to the total joint contact area (Blevens et al. [48]) compared with work from Veigas et al. [18, 87].
- The ratio of scaphoid to lunate contact area on the radius compared with the experimental work of Schuind et al. [32], Blevens et al. [48] and Horii et al. [33].
- Force transmitted through the radio-scaphoid and radio-lunate articulation compared with Veigas et al. [18, 87], Horii et al. [33], Schuind et al. [32] and Majima et al. [34].
- A quantitative comparison of contact pressure distribution compared with results from Majima et al. [34].

Reference	Load		Experiment or RBSM
	magnitude (N)	application	
Blevens et al. [48]	178	Wrist tendons	Experiment
Teurlings et al. [88]	300	Wrist	Experiment
Horii et al. [33]	140	midaxis 5 metercarpals	2d-RBSM
Majima et al. [34]	140	5 metacarpals	3d-RBSM
Schuind et al. [32]	140	5 metacarpals	2d-RBSM
Veigas et al. [18, 87]	50 100 200 400	5 metacarpals	Experiment
Pietruszczak et al. [37]	700	The fossa on the radius	FE-model

Table 4.1: Summary of experimental work relevant to the validation procedure.

4.1 A parametric study of the Geometric Approximation Model

A study was performed to determine the sensitivity of the Geometric Approximation Model to different material property parameters. The reasons for carrying out this sensitivity study are; material properties differ from person to person, the wrist joint is geometrically complex therefore the effects of geometric non-linearities need to be studied and there is a wide range of material property values presented in the literature. Stress and pressure outputs were studied due them aiding in checking if the model is behaving realistically and giving an indication of where bone fracture may occur.

For models that were modelled with linear elastic isotropic material properties a Poisson's ratio, a density and a Young's Modulus was specified for each material. For models where non-linear material properties were studied Mooney-Rivlin coefficients were used. An elastic material is a material that returns to its original shape after being deformed, this behaviour obeys Hooke's law [89, 67]. Hooke's Law of linear elasticity states that the extension of a spring is directly proportional to the load applied to it. The relationship is described by equation 4.1.

$$F = -k\Delta x \tag{4.1}$$

Where, F is the restoring force exerted by the spring, k is the axial spring stiffness (measured in force per length) and Δx is the change in length of the end of the spring from its original position. The negative sign is due to the restoring force always acting in the opposite direction of the displacement. A rod of elastic material may be viewed as a linear spring. The rod has length L and cross-sectional area A. The extension of the rod (the axial strain, ε) is linear proportional to its tensile axial stress (σ). The constant of proportionality is the Young's Modulus (E), this relationship is described in equation 4.2.

$$\sigma = E\varepsilon \tag{4.2}$$

where

$$\sigma = \frac{F}{A} \tag{4.3}$$

$$\varepsilon = \frac{\triangle L}{L} \tag{4.4}$$

Where ΔL = change in length.

$$k = \frac{AE}{L} \tag{4.5}$$

Poisson's ratio (ν) of a material is a measure of lateral strain over axial strain that occurs in a material when loaded. Poisson's ratio is related to axial stress by equation 4.6. From this relationship an increase in the magnitude of the Poisson's ratio will lead to a decrease in axial stress. An increase in Young's modulus will lead to an increase in axial stress. Young's Modulus of the constituent material is related to axial stiffness through equation 4.5.

$$\text{lateral strain} = \nu\frac{\sigma}{E} \tag{4.6}$$

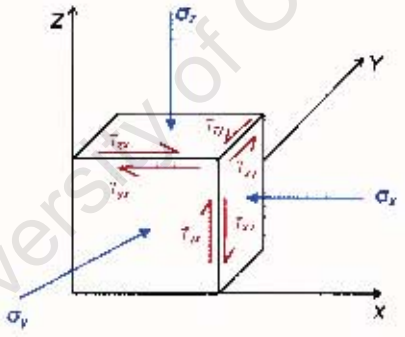

Figure 4.2: Three-dimensional stresses applied to an element.

The stress described in equation 4.3 is called Engineering nominal stress, it is a measure of a normal force acting over an area, leading to a uniform distribution of this stress over the defined area. Continuum elements were used in the FE-modelling in this work, therefore the stress at a specific point in the material was defined by the Cauchy stress tensor ($\underline{\sigma}_c$), which has nine components:

$$\underline{\sigma}_c = \begin{pmatrix} \sigma_{xx} & \tau_{xy} & \tau_{xz} \\ \tau_{yx} & \sigma_{yy} & \tau_{yz} \\ \tau_{zx} & \tau_{zy} & \sigma_{zz} \end{pmatrix} \tag{4.7}$$

Where σ are the normal stresses and τ are the shear stresses on different planes (figure 4.2). The Cauchy Stress tensor is the sum of two stress tensors; the stresses that acts on an element to change its volume without distorting it (Hydrostatic Stress tensor) and the stresses that lead to a shape change with no volume change (Stress Deviator tensor).

These variables measured during this parametric study are defined as:

von Mises Stress (σ_M) an invariant of the Stress Deviator Tensor. Principal stresses (σ_x, σ_y, σ_z) are the eigenvalues of the stress tensor. They represent the stresses that act along the principal axis of the body.

$$\sigma_M = \sqrt{{\sigma_x}^2 + {\sigma_y}^2 + {\sigma_z}^2 - \sigma_x\sigma_y - \sigma_y\sigma_z - \sigma_z\sigma_x + 3{\tau_{xy}}^2 + 3{\tau_{yz}}^2 + 3{\tau_{zx}}^2} \quad (4.8)$$

Maximum principal Stress is representative of the maximum tensile stress within the material.

Contact Pressure is the pressure between surfaces in contact. It is made up of the contact force divided by the contact area.

Contact Area is a sum of the areas of all the surface elements under contact pressure of the radial articular surface.

Cortical and cancellous bones were modelled as linear elastic isotropic materials. The effect of including linear elastic or non-linear hyperelastic material definitions for cartilage was studied. In order to look at only the effects of a particular material on the model results, only that material property was varied. The parameters for each material study are presented in table 4.2. For this analysis ligaments were modelled as linear, only the individual stiffness values were defined as per table 2.7. The lunate was not constrained. These were carried out to decrease the complexity of the model. An arbitrary load of 90N was applied to the metacarpals for these studies.

Material study	Cartilage					Cancellous bone			Cortical bone		
	E (MPa)	ν	ρ (Kg/m^3)	C1 (MPa)	C2 (MPa)	E (GPa)	ν	ρ (Kg/m^3)	E (GPa)	ν	ρ (Kg/m^3)
Cartilage	(3.5-500)	(0.05-0.49)	1100	-	-	1.4	0.2	1330	15	0.3	2100
Cartilage	-	-	1100	(4.1-45.1)	(0.41-4.51)	1.4	0.2	1330	15	0.3	2100
Cancellous	48	0.49	1100	-	-	(0.1-1.4)	(0.2-0.3)	1330	15	0.3	2100
Cortical	48	0.49	1100	-	-	1.4	0.2	1330	(5.7-22.7)	0.3	2100
Ligament	48	0.49	1100	-	-	1.4	0.2	1330	15	0.3	2100
Validation (E)	48	0.49	1100	-	-	1.4	0.2	1330	15	0.3	2100
Validation (H)	-	-	1100	4.1	0.41	1.4	0.2	1330	15	0.3	2100

Table 4.2: Material property definitions used for each material property variation study.

4.1.1 Cartilage

Linear material definition

The effect of changing the Young's modulus and Poisson's ratio of cartilage was studied. These results are presented in table C.2 in Appendix C. Young's modulus was varied between 3.5 and 500MPa (table 2.6). The variation in Young's Modulus lead to no change in the location of the maximum of the stress values studied (von Misses, Maximum principal stress), these locations (figures. 4.4 and 4.5) are consistent with the location of a Colles' fracture (figure 2.40). No significant change was noted in the magnitude of these stress values, this behaviour was expected as linear elastic material properties and a constant load controlled boundary condition were used for the model.

An increase in Young's modulus (by a factor of 142) lead a contact pressure increase (factor of 2.8 increase, figure 4.3) and a radius contact area decrease (factor of 1.5 decrease). The location of maximum contact pressure was found consistently to be on the radius articular surface. The decrease in contact area associated with the increase in contact pressure was expected as contact pressure is inversely proportional to contact area.

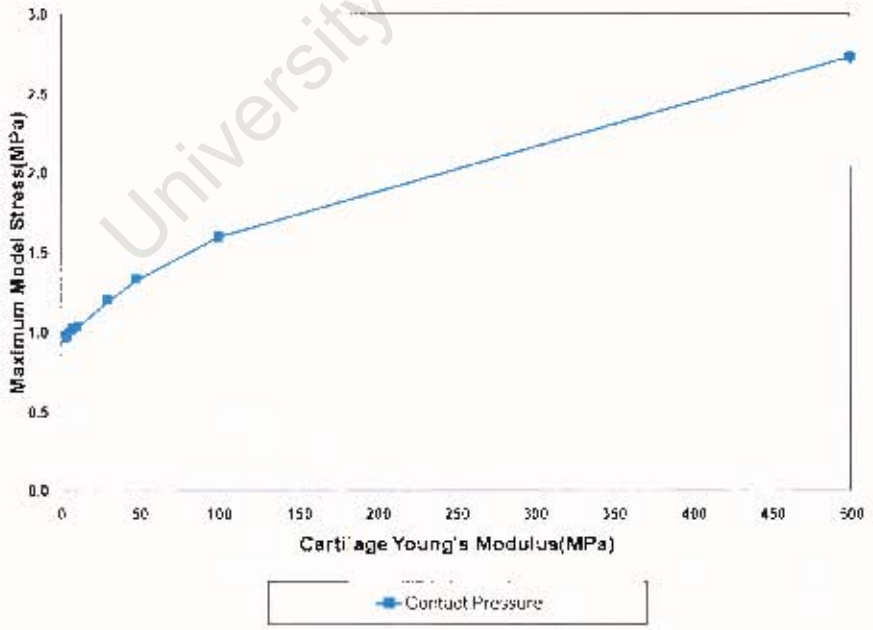

Figure 4.3: Maximum contact pressure in the model versus Young's Modulus of cartilage (3.5-500MPa).

The variation of the Poisson's ratio of cartilage was studied over a range of 0.05-0.49 (table 2.6). Cartilage is thought to behave as a compressible material (v=0) when loaded over a long term and a nearly incompressible material (v=0.5) when load is applied instantaneously. The magnitude of maximum stress measured (von Misses, Maximum principal stress and contact pressure) was consistent over the Poisson's ratio range studied. The locations of maximum stress (von Misses and Maximum principal stress) in the model was also consistent with the location of a Colles' fracture over the Poisson's ratio range. Maximum contact pressure was also consistently located on the radius articular surface over this range. These locations are away from the cartilage region of the radius, therefore no significant change in the maximum stress values or radius contact area were noted.

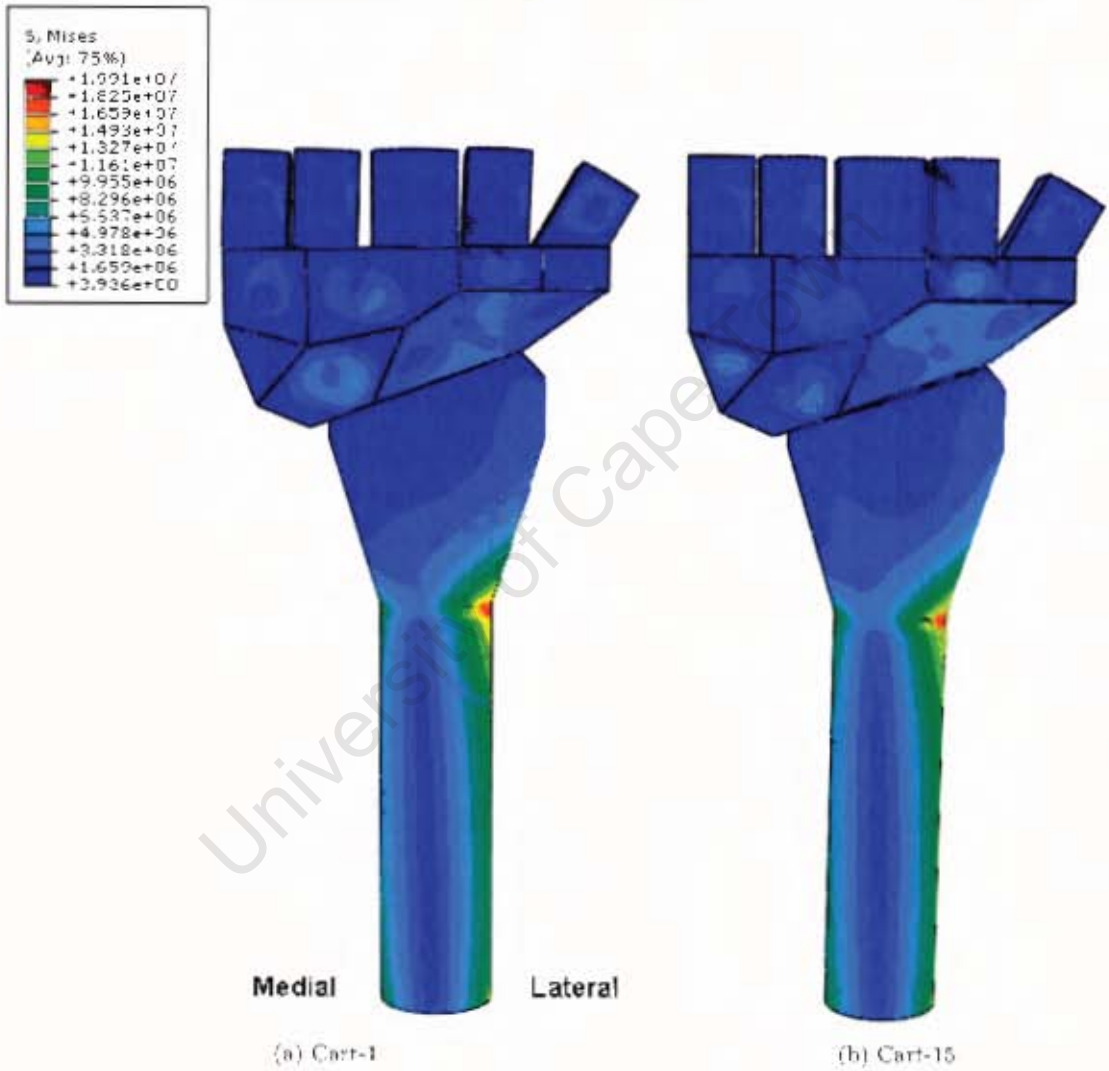

(a) Cart-1 (b) Cart-15

Figure 4.4: von Mises stress distribution (Appendix C - Table C.2).

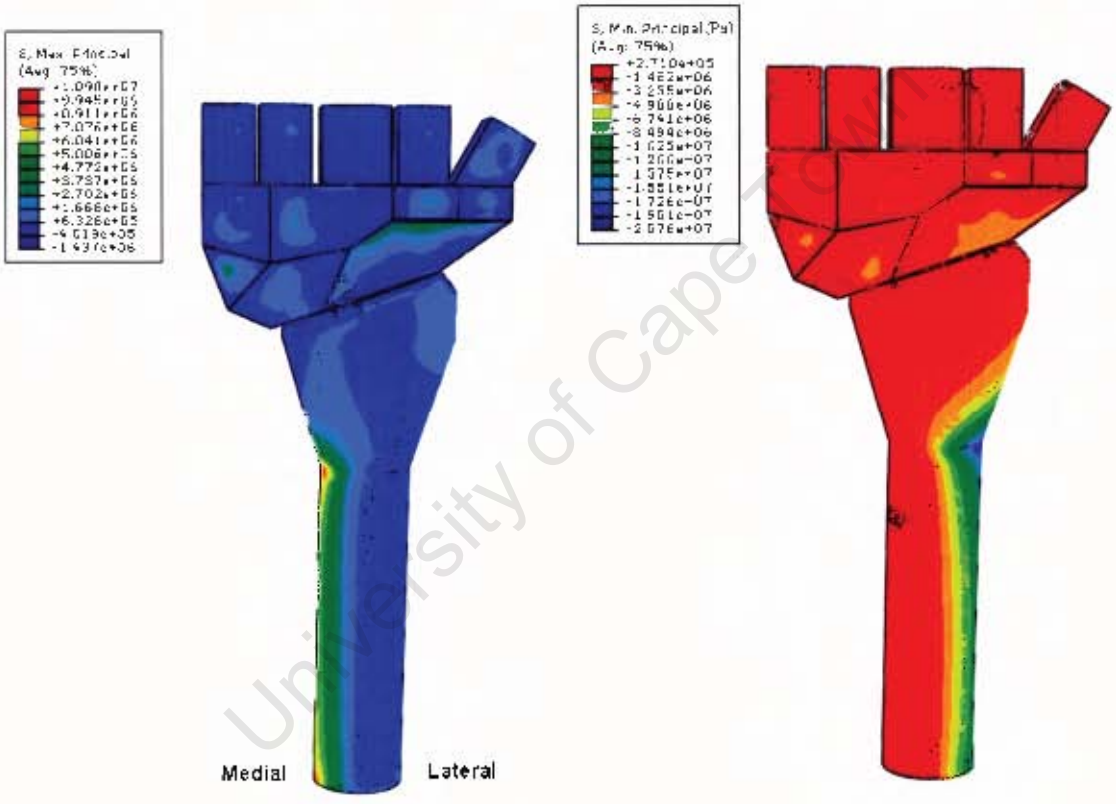

(a) Maximum (b) Minimum

Figure 4.5: Principal stress distributions .

Hyperelastic material definition

Cartilage can be modelled as a hyperelastic material, as described in section 2.9.3, whereby large elastic deformation responses are taken into account. The hyperelastic law chosen to represent the stress-strain relationship was the Mooney-Rivlin model. The Mooney-Rivlin constants chosen where $C_1 = 4.1Mpa$, $C_2 = 0.41Mpa$ and $D_1 = 0$ [54], these constants model cartilage as a nearly incompressible material. A sensitivity analysis was also carried out with 0.5, 1.5, 2.5, 10 times stiffer material properties with respect to the constants, but keeping the other parameters constant. The constants corresponding to these increased stiffness tests as well as the results of the study are presented in table C.3 in Appendix C.

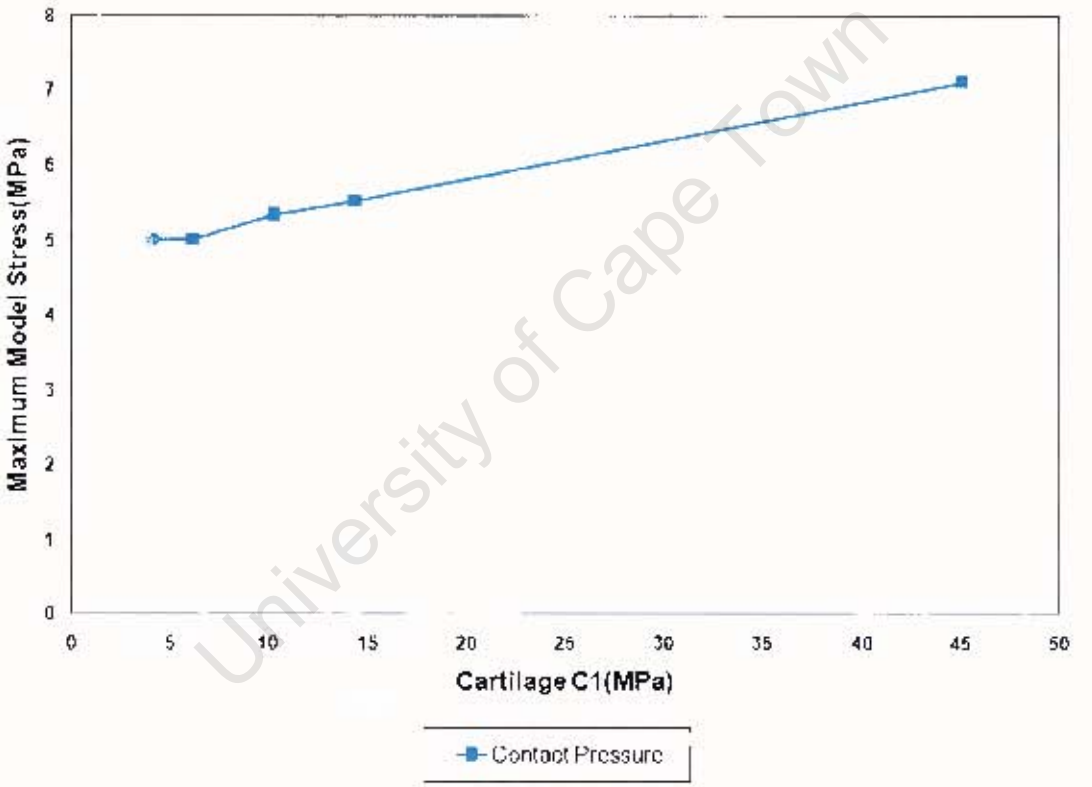

Figure 4.6: Maximum contact pressure in the model versus increasing C_1 constants for cartilage.

Figure 4.6 demonstrates that increasing the material stiffness through the Mooney-Rivlin constants lead to a slight increase in maximum model contact pressure. An increase of the constants (factor of 11) lead to a contact pressure increase (factor of 1.42). The location of the maximum contact pressure was constant as the radius articular surface. The location (typical Colles' fracture region of the radius) and magnitude of other maximum values

of stresses (von Misses and Maximum principal stress) measured, was constant over the range of Mooney-Rivlin constants.

4.1.2 Cortical bone

The effect of a variation of Young's modulus of cortical bone between 5.7-22.7GPa was studied (table 2.5). The results of this study are presented in table C.1 in Appendix C. Of the maximum values of the stresses studied (von Mises, Maximum principal stress and contact pressure), von Mises stress was the only value whose magnitude was significantly influenced by the variation in Young's Modulus. It can be noticed from figure 4.7 that an increase in Young's modulus (factor of 4) lead to an increase in von Mises stress (factor of 1.3). The location of the maximum stress values (von Mises and Maximum principal stress, figure 4.8) is consistent with the cartilage studies as the region of radius cortical bone proximal to the articular surface. The location of maximum contact pressure was also consistently on the radius articular surface over this range.

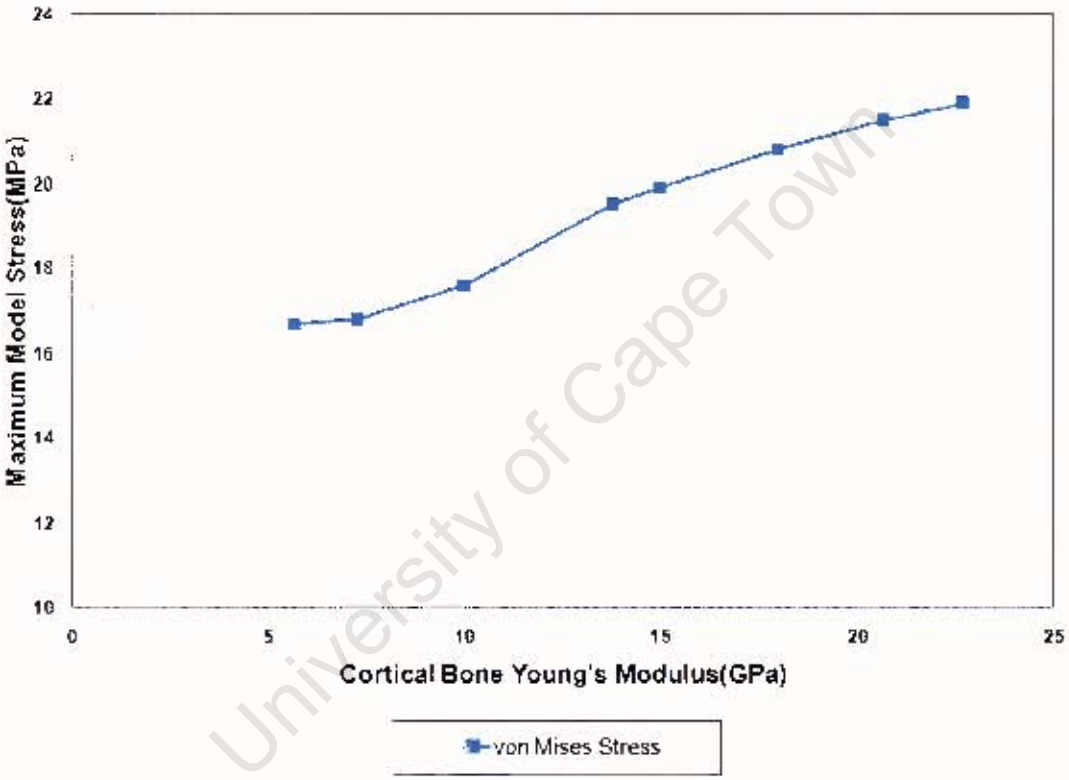

Figure 4.7: Maximum von Mises in the model versus Young's Modulus of cortical bone (5.7-22.7GPa).

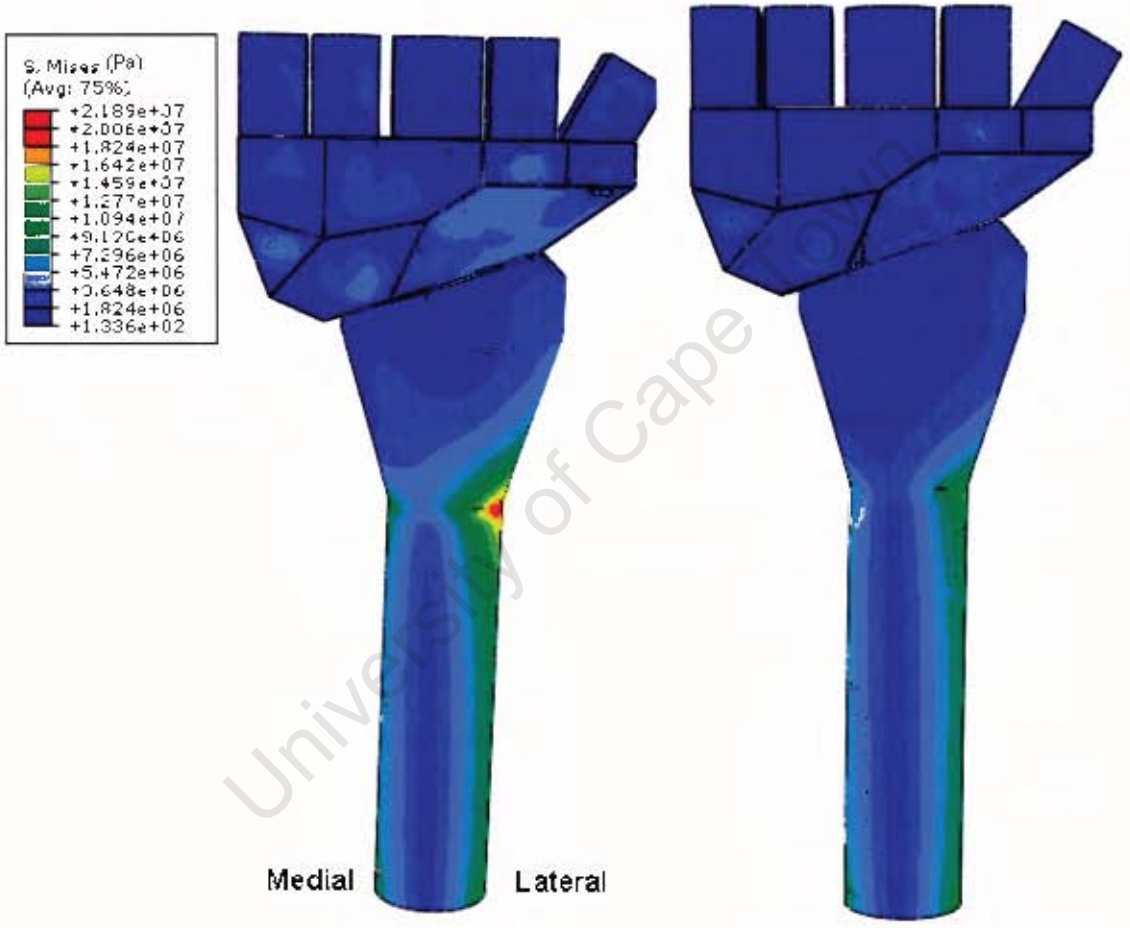

(a) Cort-8 (b) Cort-1

Figure 4.8: von Mises stress distribution (Appendix C - Table C.1).

4.1.3 Cancellous bone

For cancellous bone the effect of varying Young's modulus (0.1-1.4GPa) and the Poisson's ratio (0.2 and 0.3) were studied (table 2.4). The results are presented in table C.4 in Appendix C and figure 4.9. An increase in Young's modulus (factor of 14) lead to decreases in von Misses (factor of 2.4), Maximum principal (factor of 3.1) and contact pressure (factor of 1.6). The location of maximum contact pressure is consistent over the Young's modulus range as the radius articular surface. The maximum von Mises stress location however varies from being on the scaphoid and the radius, coinciding with the location of a Colles' fracture, at lower values of Young's modulus. At higher values of Young's modulus the location is only on the radius coinciding with the location of a Colles' fracture (figure 4.10). Therefore the effect of an increase in the stiffness of the underlying material (in the area of the maximum stress values) is, it can sustain a greater proportion of load hence not so much load has to be sustained in the cortical bone region. This leads to the decrease of maximum stress values noticed.

The effect of an increase in Poisson's ratio (factor of 2) lead to stress (von Misses, Maximum principal stress and contact pressure) and contact area magnitude and location remaining relatively constant. The location of the maximum von Mises stress is seen in figure 4.10.

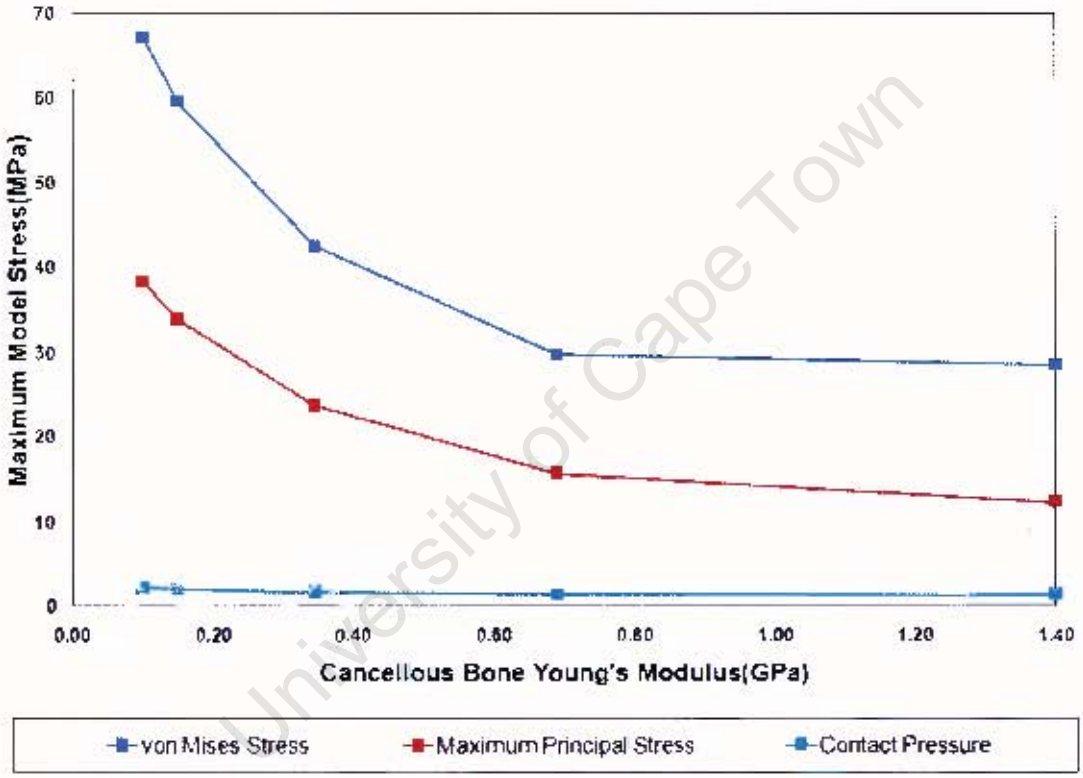

Figure 4.9: Maximum stress in the model versus Young's Modulus of cancellous bone (0.1-1.4GPa).

(a) Can-1 (b) Can-5 (c) Can-6

Figure 4.10: von Mises stress distributions (Appendix C - Table C.1).

4.1.4 Ligament stiffness

The effect of different ligament stiffness definitions on the models maximum stress output (von Mises, Maximum principal stress and contact pressure) was also considered. The effect of these definitions on the model outputs used to validate the model are described in section 4.2. The non-linear stiffness's were defined either as definition **A** [27] or definition **B** [84]. Table 4.3 shows the outputs received when each of these definitions was used. The most significant difference between the two definitions was in contact area. The locations of maximum stress values (von Mises, Maximum principal stress) was consistent over the two ligament property definitions, as the region of the radius were Colles' fracture occurs. The location of the maximum contact pressure was also consistently the articular surface of the radius.

Name	von Mises Stress (MPa)	Max Principal Stress (MPa)	Contact Pressure (MPa)	Contact Area (mm^2)
Linear	19.9	10.96	1.33	80.7
Non-linear (A)	19.9	10.96	1.33	80.7
Non-linear (B)	19.9	10.75	1.59	62.6

Table 4.3: Maximum model stress with different ligament stiffness definitions.

4.2 Comparison of FE wrist model and literature experimental results

4.2.1 Geometrically Simplified Model validation

This section deals with the process of validating the GSM. During the validation process the material properties were adjusted according to the model response and those presented in table 4.2 that best satisfied the experimental results (Validation E and Validation H in table 4.2). The validation process involved finding which model parameters best correlate to multiple experimental results. The modelling parameters considered were the ligament stiffness definition, cartilage material definition and the lunate confinement method. The different models tested are described in table 4.4. The different responses between models 1 and 2 were used to look at the effect of ligament stiffness definitions. Models (1 and 3), and (2 and 4), were used to study the effect of a hyperelastic cartilage definition compared to a linear elastic cartilage definition. The effect of the cartilage definition used on the ligament definition was also undertaken by comparing the the two groups. The effect of including the confining effects of the TFCC on the lunate were studied by models 1, 5 and 6. Finally, the actual method of confinement was considered from a comparison between models 5 and 6.

Model number	Ligament stiffness definition (section 4.1.4)	Lunate constraint method (section 3.7)	Material definition (table 4.2)
1	B	Lunate supported using beam on elastic foundation theory (BEFT)	E
2	A	Lunate supported using BEFT	E
3	B	Lunate supported using BEFT	H
4	A	Lunate supported using BEFT	H
5	B	Lunate is held so it cannot move down the joint	E
6	B	No constraint applied	E

Table 4.4: Geometrically simplified Model's model definitions.

Validation criteria 1 - Contact area on the radius-carpal articular surface

The first validation criteria chosen was the contact area of the lunate and the scaphoid on the radius articular surface. This criterion was compared with values measured from experiments conducted from Veigas et al. [18] at loads of 50, 100, 200, 300 and 400N. The same loads were applied to the metacarpals of the GSM, the load application is further discussed in section 3.7. The results are presented in tables C.12 of Appendix C and figure 4.11. The values presented in figure 4.11 for the experimental work were attained for individual joints by dividing the contact area on the radius of the lunate and scaphoid by the total joint area. For the results of the models in this work the sum of the lunate and scaphoid contact areas on the radius was divided by a value for the size of an average joint area from Blevens et al. [48]. The reason for this approximation is that the size of the radio-carpal joint in this work is smaller than that of a normal joint due to a normal joint having the addition of the area of the TFCC.

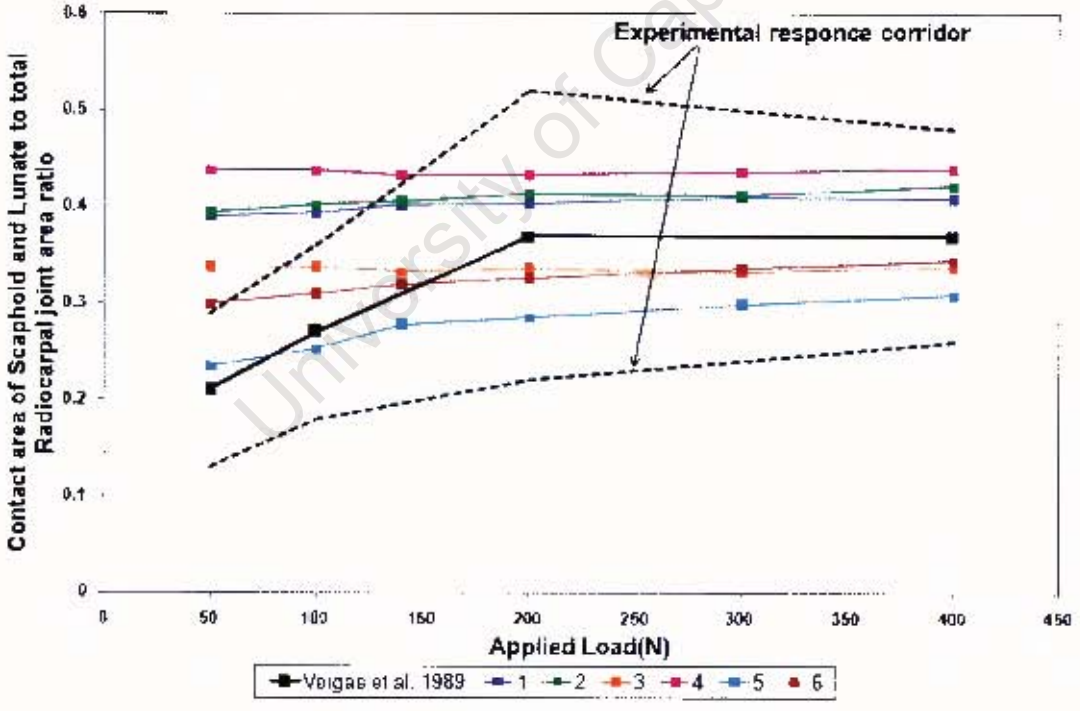

Figure 4.11: Ratio of the contact area of Scaphoid and Lunate to total radio-carpal joint area versus load applied to metacarpals, compared to experimental work from Veigas et al. [18, 87].

Figure 4.11 shows that models 5 and 6 are the only models that consistently fall within

the experimental corridor for all loads examined. The other models 1, 2, 3 and 4 do not fall with the experimental corridor at loads of 50 and 100N. This difference in behaviour of the model from the experiments is that carpal bones contact regions are not flat and rectangular like the bones modelled in the model but rather spherical therefore leading to a lower contact area at lower loads. The contact area for all the models is relatively consistent for loads of 140N and greater. A stiffer cartilage (nearly incompressible) was used, the cartilage in the experimental work however was at equilibrium. Hence, the experimental cartilage would compress with increasing load therefore leading to an increase in contact area.

Maximum contact area for models where linear cartilage material properties are defined was not affected by the ligament property definition used. Substantial differences were seen between the ligament definitions of the different cartilage definitions. Models where ligament definition **A** was used with the hyperelastic cartilage definition, had a lower contact area at all loads than the linear definition. The opposite occurred for ligament cartilage definition **B**. The effect of lunate confinement, was that the greatest contact area at all loads occurred when the beam on elastic foundation method was used, followed by the model where no confinement was used and the lowest contact area occurred in the model where lunate motion along the joint was completely confined.

The ratio of scaphoid to radius and lunate to radius contact area was also used as a validation criteria. Experimental work from Veigas et al. [18, 87], Blevens et al. [48] and Tenser et al. [88] was used to determine the experimental response corridor used. A comparison between the experimental and model ratios is presented in figure 4.12. The actual contact areas for each are presented in table C.9 of Appendix C and figures 4.13 and 4.14. From figure 4.12 it is noted that only model results from 5 and 2 fall consistently within the corridor for all loads applied. The experimental corridor boundaries were determined from the experimental results at 100N. At this load models 2, 3, 5 and 6 all fall within this boundary and models 1 and 4 fall close to the boundary. There was no experimental results found to determine the ratio at higher loads, to check if the model behaviour of scaphoid to lunate contact at these higher loads is realistic.

Models 1-4 and 6 all experienced an increase in the ratio with increasing load. Model 6 experience an initial decrease until a load of 200N, then remains constant till 300N then an increase to 400N. Figure 4.14 shows that the contact area of the lunate decreases with increasing loads for model's 1-4 and 6. Model 5 increases with increasing load until a load of 300N then remains constant.

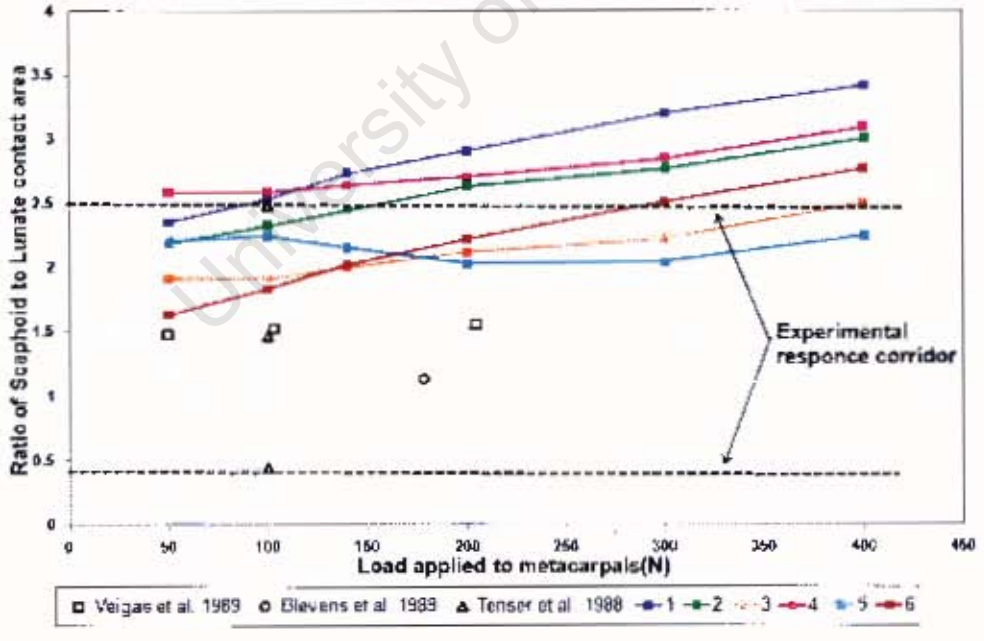

Figure 4.12: Ratio of Scaphoid to Lunate contact area versus load applied to the metacarpals, compared to experimental work from Veigas et al. [18, 87], Blevens et al. [48] and Tenser et al. [88].

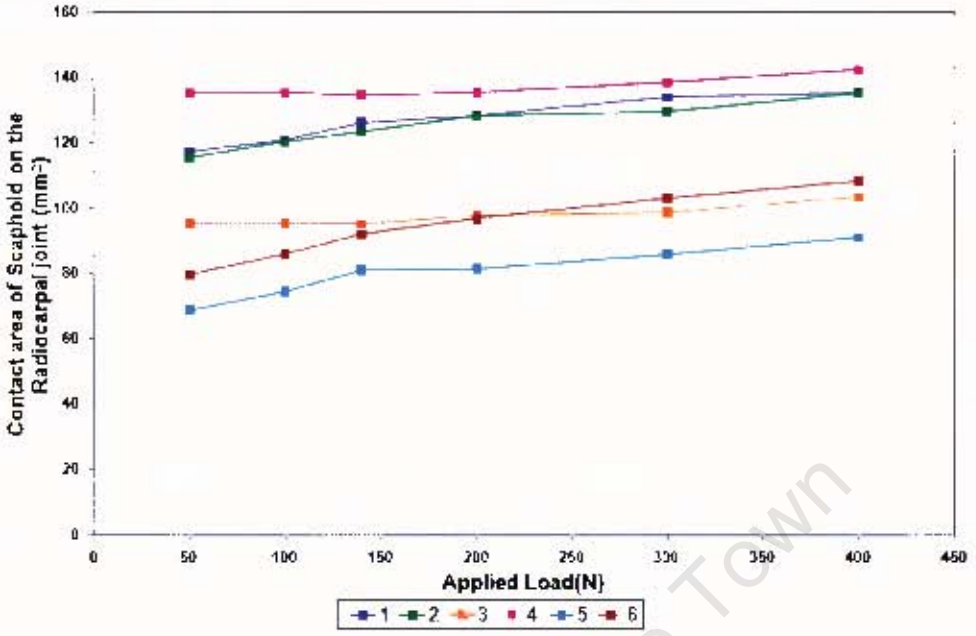

Figure 4.13: Contact area of the scaphoid on the radius articular surface.

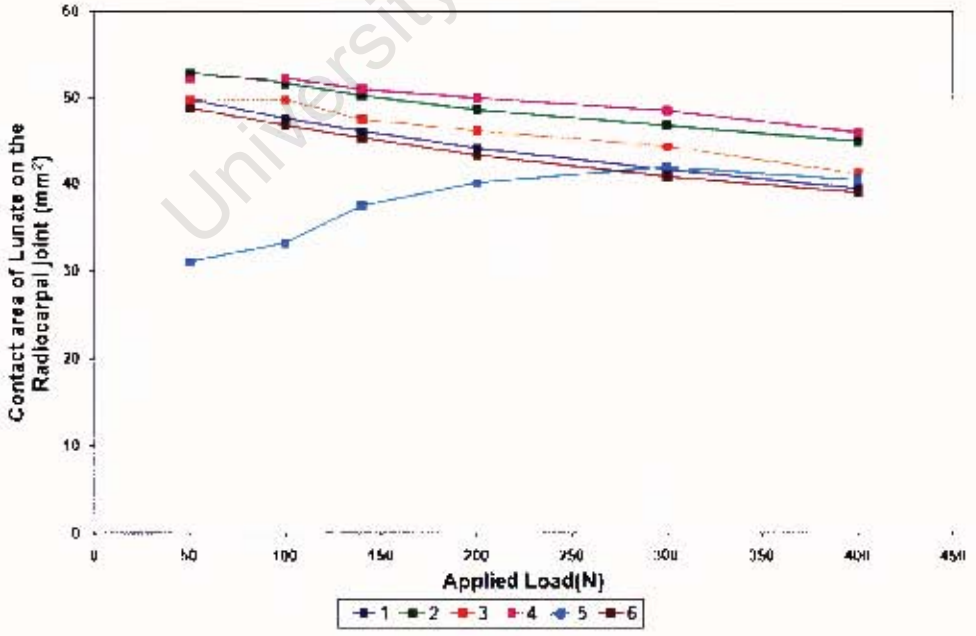

Figure 4.14: Contact area of the lunate on the radius articular surface.

Total/joint Figure 4.11		Scaphoid/Lunate Ratio Figure 4.12		Scaphoid Figure 4.13		Lunate Figure 4.14	
Model	Behaviour	Model	Behaviour	Model	Behaviour	Model	Behaviour
4	Constant	1	Increasing	4	Constant	4	Deceasing
2	Constant	4	Increasing	1	Increasing	2	Deceasing
1	Constant	2	Increasing	2	Increasing	3	Deceasing
3	Constant	6	Increasing	3	Constant	1	Deceasing
6	Increasing	3	Increasing	6	Increasing	6	Deceasing
5	Increasing	5	Decreasing	5	Constant	5	Increasing

Table 4.5: General behaviour of the radio-carpal contact areas with increasing applied load (140-300N) for models 1-6. The columns are arranged in descending order of magnitude corresponding to the graphs (figures 4.11, 4.12, 4.13 and 4.14).

Table 4.5 summarises the behaviour of the models between loads of 140-300N for the different contact area graphs presented in this section. The total contact area is constant for Models 1-4, but increases for Models 5 and 6. The increase in contact area of these models is constant with the increase in scaphoid to lunate contact area. The increase in this ratio is due to the decrease in lunate contact area for these models. Models 1-4 also have the highest contact area magnitudes. All of these models have the lunate supported by the BEFT. Therefore this method of support leads to the highest contact area. The effect of cartilage material definition is the hyperelastic material (Models 3 and 4) experienced a constant scaphoid contact area, with decreasing lunate area. The effect of the ligament definition used was that for hyperelastic models definition **A** (Model 4) had a higher contact area than B (Model 3). The case for when the linear elastic definition was used is that definition **A** caused a higher total contact area and lunate contact area than **B**. But definition **A** had a higher scaphoid to lunate ratio, due to the higher scaphoid contact, than **B**.

The effect of lunate confinement is that the BEFT leads to the highest total, scaphoid and lunate contact areas (Models 1-4). This is followed by the Model 6 where no constraint was used and finally Model 5 where the lunate's boundary motion was constrained. Models that do not use the BEFT experience an increase in total contact area with increasing load. The cause of the increasing total contact area for the model where no constraint was used (Model 6) is the increase in scaphoid area. The lunate contact area for Models 5 and 6 also decreased with increasing load, this decrease could be due to a slight downward movement along the radius articular surface of the lunate due to the lack of constraint. The ratio of

scaphoid to lunate contact area also increases with increasing load for this method. Model 5 whose motion down the radius articular surface is constrained experiences an increase in total contact area and scaphoid to lunate ratio. These increases are completely due to the increase in lunate contact area whilst the scaphoid contact remains constant. This behaviour is due to this constrainment method not allowing the lunate to displace along the radius, therefore it displaces proximally (in the direction of the load, perpendicular to the joint surface) leading to an increase in contact area.

Validation criteria 2 - Contact pressure on the radius-carpal articular surface

The contact pressure on the radius articular surface has been measured in many different experimental setups. The work conducted by Veigas et al. [18] was chosen to validate the maximum contact pressure value determined by the model on this surface. The loads chosen to measure this value were at 50, 100, 200, 300 and 400N. The load application is further discussed in section 3.7. The experimental response at 50N is unrealistic as a negative contact pressure measured with pressure sensitive film is impossible. Therefore, this point was not used for comparison. The results for the behaviour of the different models at these loads is shown in table C.5 of Appendix C and figures 4.15 and 4.16. Figure 4.15 shows that Models 1, 2, 3, 4 and 6 all fit well within the experimental response corridor. Model 5 however experienced a maximum contact pressure at 200N that did not fall with the corridor. At all loads model 5 experienced maximum pressure values that were much greater than the other models, but these values were still close to or within the experimental corridor.

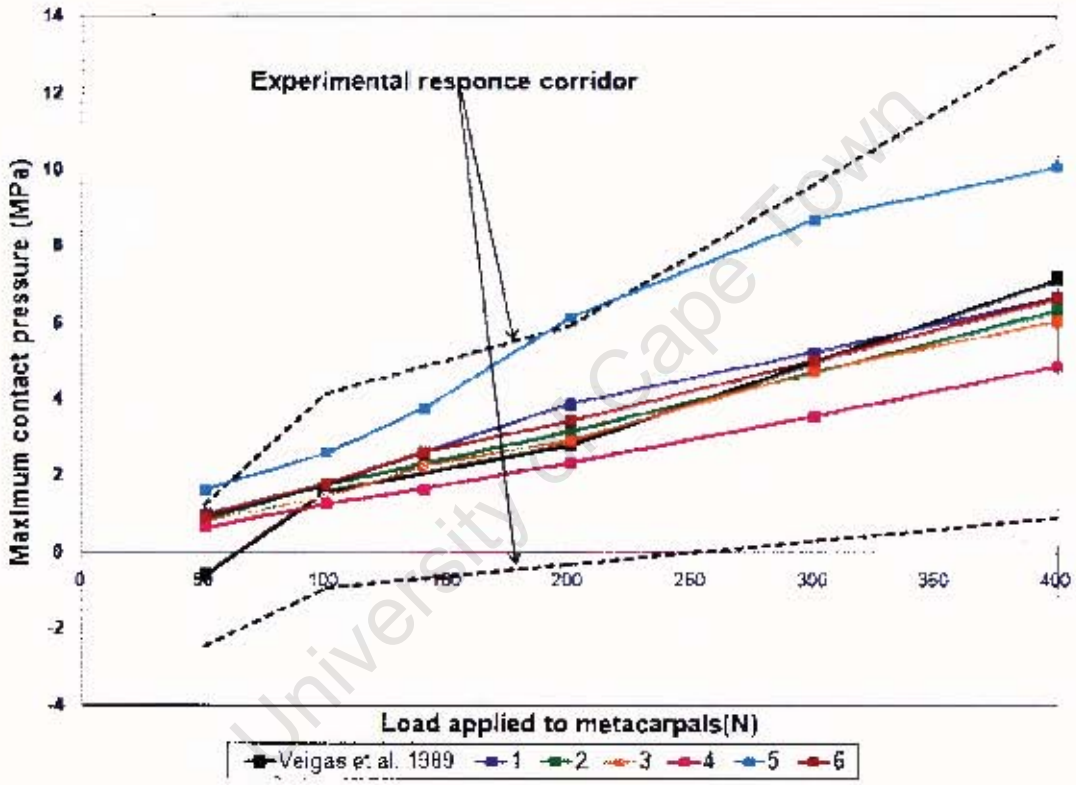

Figure 4.15: Maximum contact pressure versus load applied to the metacarpals, compared to experimental work from Veigas et al. [18, 87].

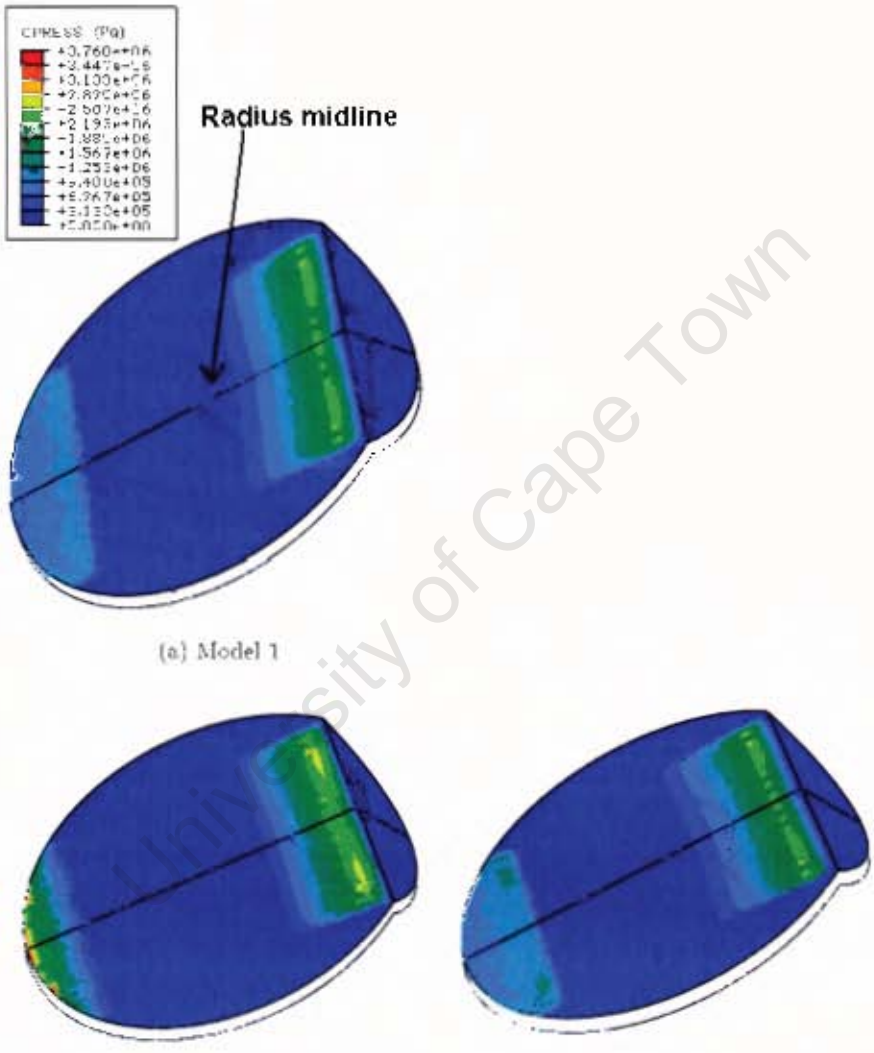

(a) Model 1

(b) Model 5

(c) Model 6

Figure 4.16: contact pressure on the radius articular surface at an applied load of 140N.

The contact pressure on the radius articular surface was further validated by determining the contact pressure profile along the midline of the radius. The maximum values of contact pressure for the radio-lunate and radio-scaphoid articulation were compared with the maximum values determined from experimental work conducted by Teurlings et al. [88]. The loading configuration in the experiment involved a 300N load being applied to the wrist joint. The results of the study of the different models behaviours at this load are described in table C.7 and 4.6 in Appendix C and figure 4.17.

Models 1, 4 and 6 experienced maximum contact pressures for the radio-lunate articulation that lay within the experimental corridor. The other models maximums are greater then the corridors. Models 1, 5 and 6 are the models that experienced maximum contact pressure values for the radio-scaphoid articulation that lay within the experimental response corridor. The other models maximum values are less than the corridors. Therefore, Models 1 and 6 are the only models that experiences values within both scaphoid and lunate corridors.

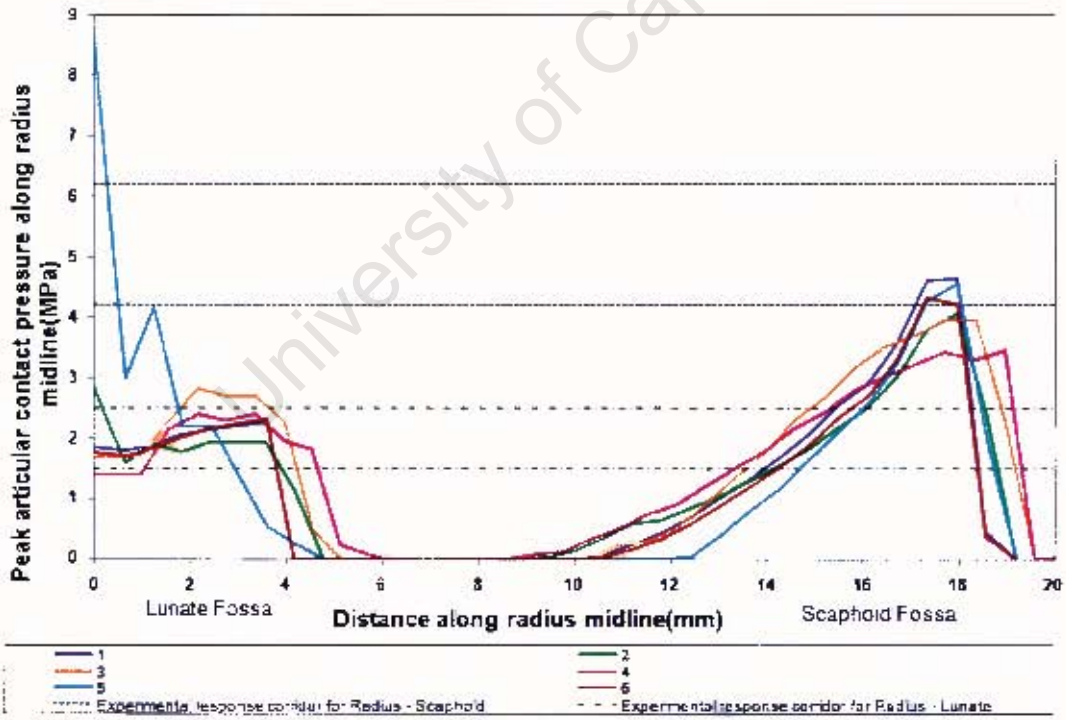

Figure 4.17: Peak articular contact pressure along the radius midline versus distance along the midline at a 300N load, compared to experimental work from Teurlings et al. [88].

The ratio of radio-scaphoid to radio-lunate maximum contact pressure is compared to experimental work from Blevens et al. [48] and 2-d RBSM results of Schuind et al. [32] and Horri et al. [33]. The results from the cadaveric experimental work of Blevens et al. [48] were acquired by the application of load through the wrist tendons. The maximum contact pressure values reported in the work of Schuind et al. [32] and Horri et al. [33] could not be compared directly as they were reported in N/mm as they were 2-d models. A comparison of the different models ratios to the experimental ratios is shown in figure 4.18. Figure 4.18 shows that only Models 3, 4 and 5 fall within this experimental response corridor at a load of 300N.

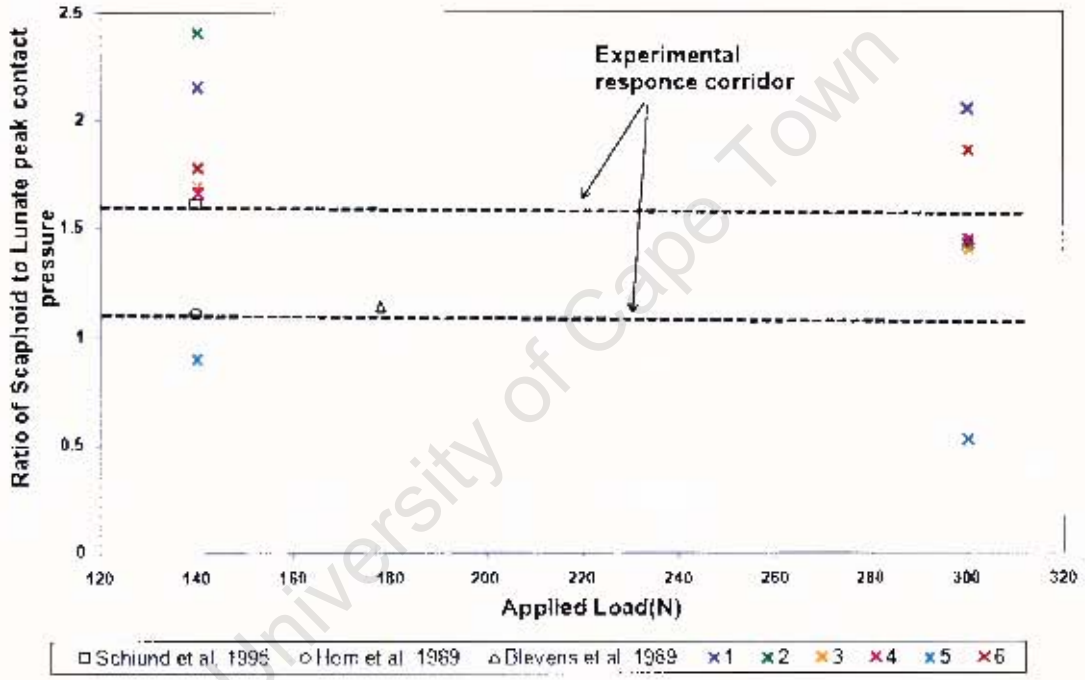

Figure 4.18: Ratio of Scaphoid to Lunate peak contact pressure versus applied load, compared to experimental work from Schuind et al. [32], Horri et al. [33] and Blevens et al. [48].

Noted from figure 4.18 is that at both loads of 140 and 300N, the scaphoid contact pressure is greater than the lunate contact pressure (Models 1, 2, 3 ,4 and 6). Therefore even though GSM results do not fall within the experimental boundaries at all loads, most of the models behave the same as these experimental results. This qualitative comparison is still valid. The reason for the differences could be due to the load application not occurring through the tendons as was in Blevens et al. [48] experimental work. The 2-d model of Schuind et al. [32] and Horri et al. [33] would not include any out of plane movement. Model 5

experiences the opposite at both loads.

Total Figure 4.15		Peak scaphoid Figure 4.17		Peak lunate Figure 4.17		S/L peak pressure Figure 4.18	
Model	Behaviour	Model	Validation boundaries	Model	Validation boundaries	Model	Behaviour
5	Increase	5	Greater	1	Within	2	Decrease
1	Increase	2	Greater	5	Within	1	Constant
6	Increase	3	Greater	6	Within	6	Increase
2	Increase	4	Within	2	Greater	3	Decrease
3	Increase	6	Within	3	Greater	4	Decrease
4	Increase	1	Within	4	Greater	5	Decrease

Table 4.6: General behaviour of the radio-carpal contact pressure with increasing applied load (140-300N) for models 1-6. The columns are arranged in descending order of magnitude corresponding to the graphs (figures 4.15, 4.17, 4.18).

Table 4.6 contains a summary of the contact pressure behaviours for the different models in the figures 4.15, 4.17, 4.18 within this section. The effect of the different methods of defining the material properties of cartilage on the maximum contact pressure was the same for both ligament definitions **A** (2 and 4) and **B** (1 and 3). The hyperelastic cartilage definition (3 and 4) lead to lower maximum contact pressure than the linear elastic definition (1 and 2). The difference caused by the ligament stiffness definitions was that definition **A** lead to lower maximum contact pressures at all loads than definition **B**.

The effect of the cartilage definition was that the linear models experienced greater ratios of scaphoid to lunate peak contact pressure than the hyperelastic models. For both of these material definitions, an increasing load lead to a decrease in this ratio. Contact pressure is related to contact area through equation 4.3, where contact pressure is the stress component of equation and contact area the area. Contact pressure is inversely proportional to contact area. Therefore the increase in maximum contact pressure seen with increasing load, is associated with a constant or slight decrease in contact area with this increasing load. Which is consistent with the constant ratio of contact areas in table 4.5 for Models 1-4 (lunate's confined using BEFT).

Contact pressure was distributed on the radius articular surface shown in figure 4.16 for the models with the different lunate confinement methods. Model 5 experienced the greatest Contact pressure of all the models, at a load of 140N, due to the movement of the

lunate along the joint being confined, hence it can only displace proximally. The contact overclosure in this region is large leading to an increase in contact pressure as noted in figure 4.16.

A decrease of maximum contact pressure ratio with increasing load applied was noticed for all models except for Model 6. All of the models that experienced the decrease had their lunate bones confined. This increase for Models 1-4 is possibly due to the constant contact area ratio shown in table 4.5. The contact area ratio for Model 5 was seen to decrease over this load range, therefore a different reason for the contact pressure ratio increase was needed. Not having the lunate's motion confined along the joint would lead to the movement of it down the joint, causing a decrease in the overclosure that would occur if the lunate was confined and experienced a large proximal movement on the radius articular surface. This overclosure would increase with increasing load, hence the increase in contact pressure.

Validation criteria 3 - Ligament behaviour

The ligament behaviour was validated by comparison with the behaviour of ligaments in the RBSM of Schuind et al. [32] at a load of 140N. The RBSM was a 2-dimensional model so the force transmission was not compared quantitatively, instead a qualitative comparison was carried out. This validation work considers ligament tension to only be considered significant if it is above 5N. The ligament that was found through this RBSM to transmit the most force was the Radio-lunate ligament. The ligaments force transmissions as a percentage of the total load transmitted at 140N was determined, the results are presented in table 4.7. It was noticed that the ligament that consistently, amongst all the models, transmitted the most load was the Radio-lunate ligament.

Ligament attachment		Percentage of 140N load applied (%)					
bone1	bone2	1	2	3	4	5	6
Radius	Scaphoid	0.75	1.21	0.77	1.27	0.47	0.91
Lunare	Scaphoid	0.36	1.05	0.60	1.56	0.40	0.41
Lunate	Triquetrum	3.63	3.70	4.34	3.99	1.95	1.42
Capitate	Scaphoid	0.07	0.17	0.16	0.33	0.08	0.10
Capitate	Triquetrum	1.80	2.94	1.69	2.88	3.20	2.14
Capitate	Hamate	0.02	0.14	0.01	0.10	0.01	0.02
Capitate	Trapezium	1.34	2.19	1.43	2.27	1.27	1.40
Scaphoid	Trapezium	0.27	1.14	0.45	1.49	0.05	0.32
Scaphoid	Trapezoid	0.01	1.29	0.35	2.02	0.54	0.09
Triquetrum	Hamate	0.38	0.66	0.31	0.56	0.50	0.40
Lunate	Hamate	1.20	2.05	1.13	1.97	2.37	1.40
Lunate	Capitate	0.06	0.06	0.17	0.28	0.37	0.10
Capitate	Trapezoid	0.10	0.39	0.16	0.49	0.06	0.13
Trapezoid	Trapezium	0.48	0.55	0.50	0.83	0.51	0.50
Lunate	Radius	7.87	9.95	8.62	10.50	4.92	9.69

Table 4.7: Ligament load when a 140N load is applied to the metacarpals for models 1-6.

The tensile behaviour of the Radio-lunate ligament was further analysed in figures 4.19 and 4.20. Figure 4.19 shows the force-displacement behaviour of the Radio-lunate ligament. Figure 4.20 shows the amount of total force transmitted through the Radio-lunate ligament of the total applied load for each model. Models 2 and 4 have the same ligament definition and Models 1, 3, 5 and 6 all have the same ligament definition. Figure 4.19 shows the force-displacement behaviour of the Radio-lunate ligament. Model 5 transmits the least force of the total applied force, due to the position of the lunate being fixed. The ligament

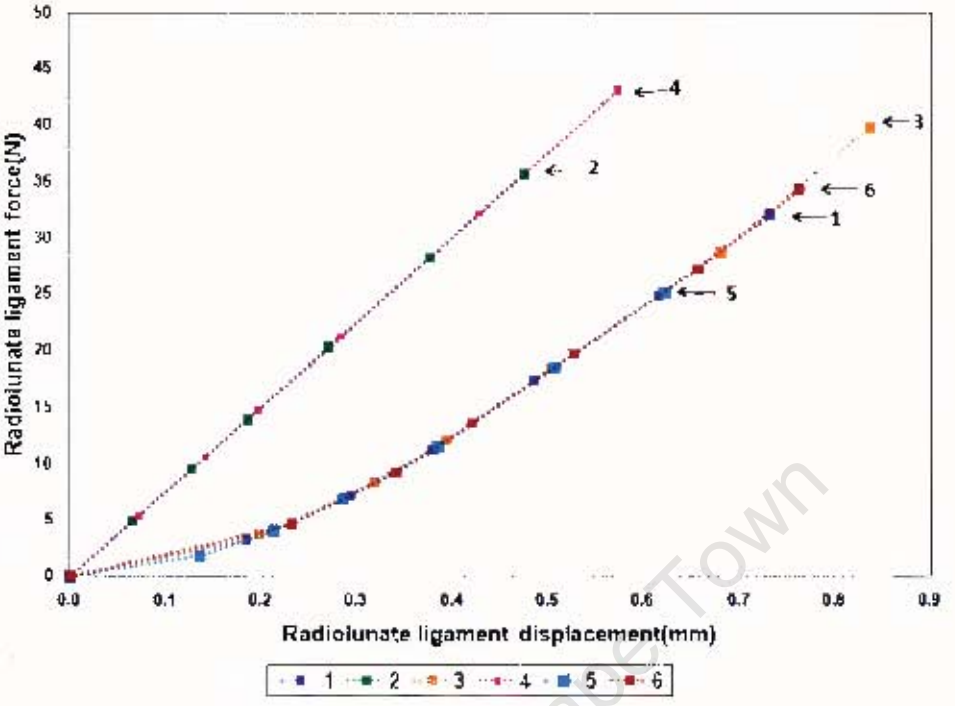

Figure 4.19: Radio-lunate ligament force versus ligament displacement.

undergoes the least amount of displacement (figure 4.19).

For both ligament definitions where lunate movement was confined using the BEFT, Models 3 and 4 (hyperelastic cartilage) experienced a greater force transmission of the total load and a greater displacement than models 1 and 2 (linear cartilage). Models 1, 5 and 6 differed only by the method used for the confinement of the lunate. Model 6's Radio-lunate ligament underwent the most displacement, as the lunate motion was not confined. Model 1 experiences a greater displacement that model 5, due to the elastic springs (BEFT) allowing the lunate to displace based on the defined spring stiffness.

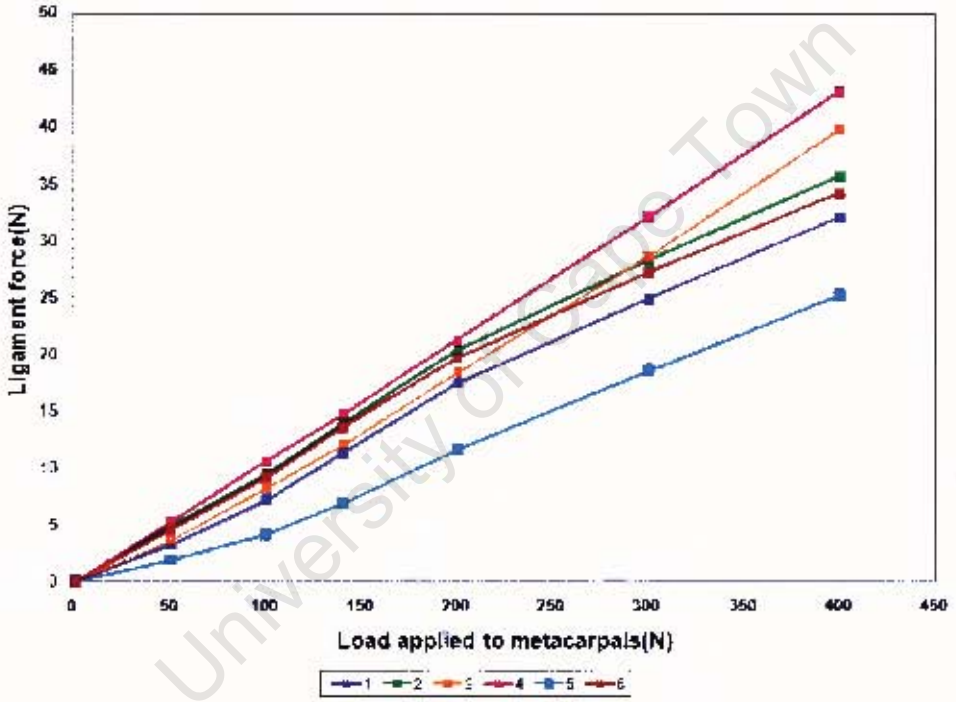

Figure 4.20: Radio-lunate ligament force versus load applied to the metacarpals.

Validation criteria 4 - Force transmission through the radio-carpal joint

The forth validation criteria was the percentage of total load transmitted through the mid-carpal and radio-carpal joints. For models 1, 2, 3, 4 and 6 the load transmission through the individual bone connection that make up these joints was consistent amongst them. The model force transmission and the experimental force transmission are presented in table 4.8. The models in this thesis did not include a TFCC directly so the force transmission through the TFCC-lunate connection could not be compared. Therefore the models differed from the experimental work slightly in that the force will be distributed between the scaphoid-radius and lunate-radius articulations only. The experimentally applied load chosen for this comparison was 140N, as it was the load applied for the experimental work of Majima et al. [34], Horii et al. [33] and Schuind et al. [32]. An example of the load transmission for a 140N load (70N in half symmetry model) through Models 1 and 2 is shown in figure 4.21.

Load transmission for all the Models fell within the experimental corridor for all the joints except the radius to trapezoid and trapezium articulation. The force transmitted through this articulation was slightly greater for all the models. This difference is due to the geometric differences between real bones and the bone approximations.

Since the load transmission percentages for each load were the same for Models 1, 2, 3, 4 and 6, it can be concluded that ligament definition and cartilage material model used have very little effect on the magnitude of load transmission. Whether the lunate is unsupported or supported using the BEFT does not have an effect on this parameter either. A slight difference occurs between these models and Model 5. Constraining the motion of the lunate completely causes a slight difference in force transmission.

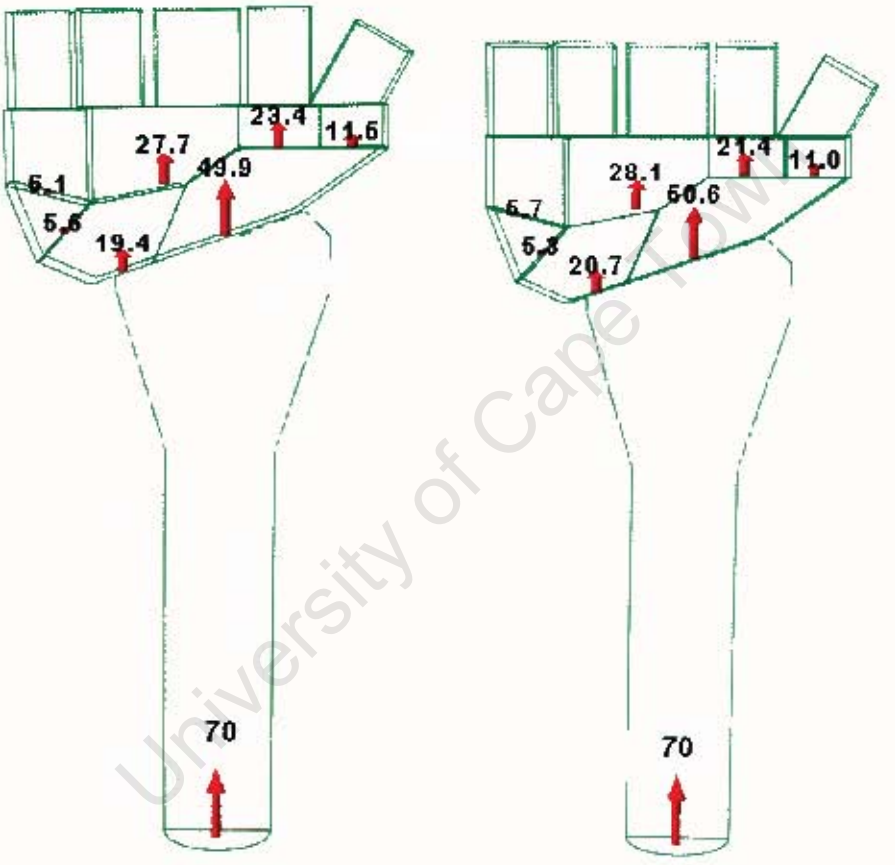

(a) Model 1 (b) Model 2

Figure 4.21: Vertical component of the load transmission through joints of the wrist at a 140N load.

Study	Distal Radio-carpal joint			Mid-carpal joint		
	Radio-scaphoid (%)	Radio-lunate (%)	TFCC lunate & triquetrum (%)	Triquetrum hamate (%)	Capitate Scaphoid&Lunate (%)	Scaphoid Trapezoid&trapezium (%)
Majima et al. [34]	52	42	6	-	-	-
Horri et al. [33]	52±9	37±6	25±8	26±4	59±7	36±6
Schuind et al. [32]	63±9	40±7	11±5	13±5	79±14	40±5
Veigas et al. [18]	60	40	-	-	-	-
Blevens et al. [48]	34	26	40	-	-	-
Experimental corridor	34-72	26-47	6-40	8-30	52-93	30-45
Models 1, 2, 3, 4& 6	70	30	-	8	41	51
Model 5	68	32	-	7	43	50

Table 4.8: Load transmission through the wrist joint.

Summary of validation criteria results for the Geometrically Simplified Model

A summary of the validation results of the GSM follows. The model that fits most of the validation work's parameters will be incorporated into the ABGM. The first validation criteria considered was the contact area of the scaphoid and lunate bones on the radius articular surface. Two parameters were considered for this criterion. The first parameter being the ratio of total contact area on the radius articular surface to the total joint area. These results were validated with work from Veigas et al. [18, 87] (figure 4.11). Models 1-6 all fell within the experimental boundaries for all the loads studied . The second parameter studied was the ratio of scaphoid contact area to lunate contact area. This was compared to work from Veigas et al. [18, 87], Blevens et al. [48] and Tenser et al. [88] (figure 4.12). The boundaries of the experimental response corridor for this work was determined at a load of 100N. At this load Models 1, 2, 3, 5 and 6 all fit on or within the boundary. At a load of 200N only Models 6, 3 and 5 fit within the boundary.

The second validation criteria considered was the maximum contact pressure on the radius articular surface. There were three parameters considered for this criterion. The first was the maximum contact pressure at increasing loads. These results were validated with work from Veigas et al. [18, 87] (figure 4.15). Models 1, 2, 3, 4 and 6 all fell within the experimental corridors. Model 5 fell within for all loads except for load 200N. The second parameter was the magnitude of maximum contact pressure on the radius-lunate and radius-scaphoid articulation. A comparison was conducted with work from Tenser et al. [88] at a load of 300N (figure 4.17). Models 1 and 6 were the only models that fell within the experimental boundaries for both these articulations. The third parameter was the ratio of scaphoid-radius and lunate-radius peak pressure. This was compared to work from Blevens et al. [48], Schuind et al. [32] and Horri et al. [33] (figure 4.18). At a load of 140N none of the models fell within the corridor. At a load of 300N, Models 2, 3 and 4 fell within the corridor. A qualitative comparison of the behaviour of these results was also considered. All the results had ratio's that were greater than 1. This was the case for Models 1-4 and 6.

The third criterion was the a qualitative comparison as to which ligament carried the most tensile force in the model. This comparison was compared with the results from Schuind et al. [32] (table 4.7). The Radio-lunate ligament for all models carried the most significant tensile force, which was consistent with the findings of Schuind et al. [32].

The final criterion was the force transmission percentages through the radio-carpal and

mid-carpal joints. The comparison was made with results from Majima et al. [34], Horri et al. [33], Schuind et al. [32], Veigas et al. [18] and Blevens et al. [48](table 4.8). All the models load transmission percentages fit within the experimental corridors for the radio-carpal, the triquetrum-hamate and the capitate-scaphoid and lunate joints. The scaphoid-trapezium and trapezoid joint was slightly above the boundary for all the models.

Models 1 (lunate constrained using BEFT, ligament definition B [84], cartilage modelled as linear elastic) and 6 (lunate unconstrained, ligament definition B [84], cartilage modelled as linear elastic) fell within the most parameters of the criterions used for the validation. Therefore these models were considered validated. Model 1 was chosen for the ABGM due to the incorporation of the shock absorbing role of the TFCC.

4.2.2 Accurate Bone Geometry Model validation

The lunate confinement and ligament stiffness definition parameters of Model 1 of the GSM was chosen to be used in the ABGM. The ABGM geometry and bone material properties were created from a volunteer's CT-scan (Appendix D). These properties are specific to the subject. The incorporation of Model 1 parameters into this model is a method of further validating these parameters for a volunteer's case. Two different carpal confinement methods were considered for the ABGM. These methods are further discussed *in section 3.7. The parameters used for the two different models studied are summarised* in table 4.9. The stiffness of the bushing connector (section 3.7) and the contact pressure value when the clearance is zero used for softening contact (section 3.5) were decided based on which values gave results closest to the experimental validation results (as described in fig. 4.1). The validation criteria used for the ABGM were the same as those used for the GSM.

Model number	Ligament stiffness definition (section 4.1.4)	Lunate constraint method (section 3.7)	Carpal constraint method applied (section 3.7)
7	B	Lunate supported using BEFT	Distal row carpal bones constrained
8	B	Lunate supported using BEFT	All carpal bones constrained at one node using bushing conector

Table 4.9: Model definitions for the Accurate Bone Geometry Model.

Validation criteria 1 - Contact area on the radius-carpal articular surface

The first validation criteria chosen was the contact area of the lunate and scaphoid on the radius articular surface. This criterion was compared with values measured from experiments conducted by Veigas et al. [18, 87] at loads of 100, 140, 200 and 300N. The same loads were applied to the metacarpals of the GSM, the load application is further discussed in section 3.7. The results are presented in tables C.12 of Appendix C and figure 4.22. Figure 4.22 is the ratio of total contact area of the radius articular surface divided by the total radio-carpal joint area. The total joint area used was measured to be $1285mm^2$. Models 7 and 8 both fall within the experimental response corridors at all applied loads, therefore the carpal confinement method has no significant effect on this variable. The contact area remains constant with increasing loads for both these models.

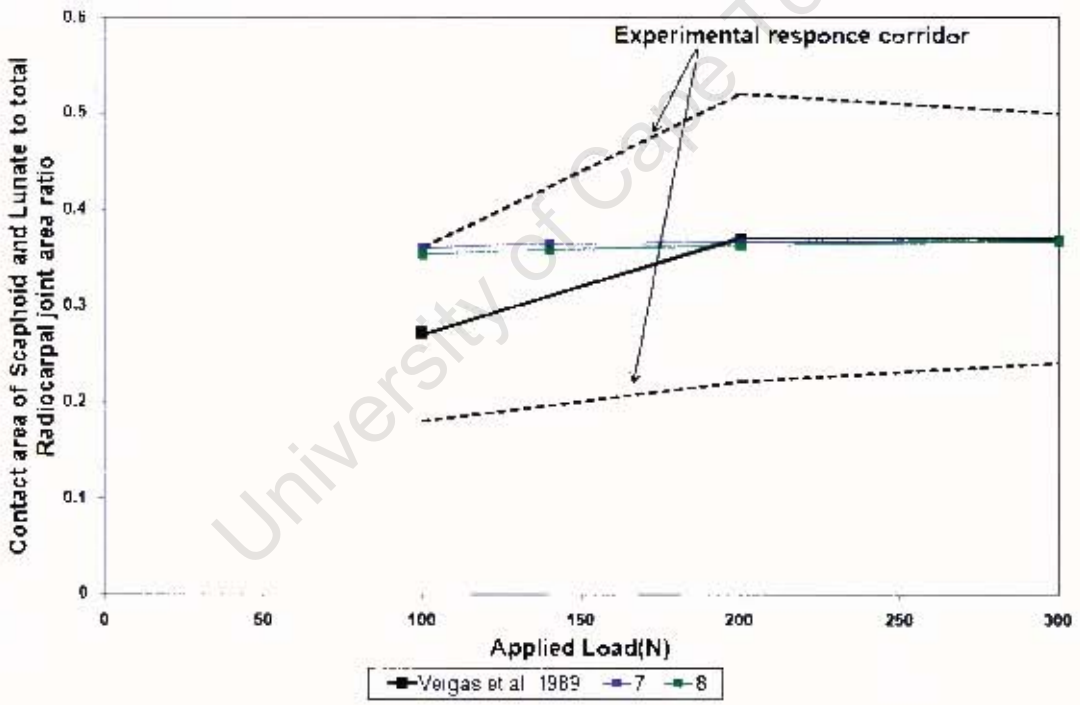

Figure 4.22: Contact area of scaphoid and lunate to total radio-carpal joint area ratio versus load applied to metacarpals, compared to experimental work from Veigas et al. [18, 87].

The ratio of scaphoid to radius and lunate to radius contact area was also used as a validation criteria. Experimental work from Veigas et al. [18, 87], Blevens et al. [48] and Tenser et al. [88] was used to determine the experimental response corridor used. A comparison between the experimental and model ratios is presented in figure 4.23. The actual contact areas for each presented in tables C.12 and C.9 of Appendix C and figures 4.23 and 4.24.

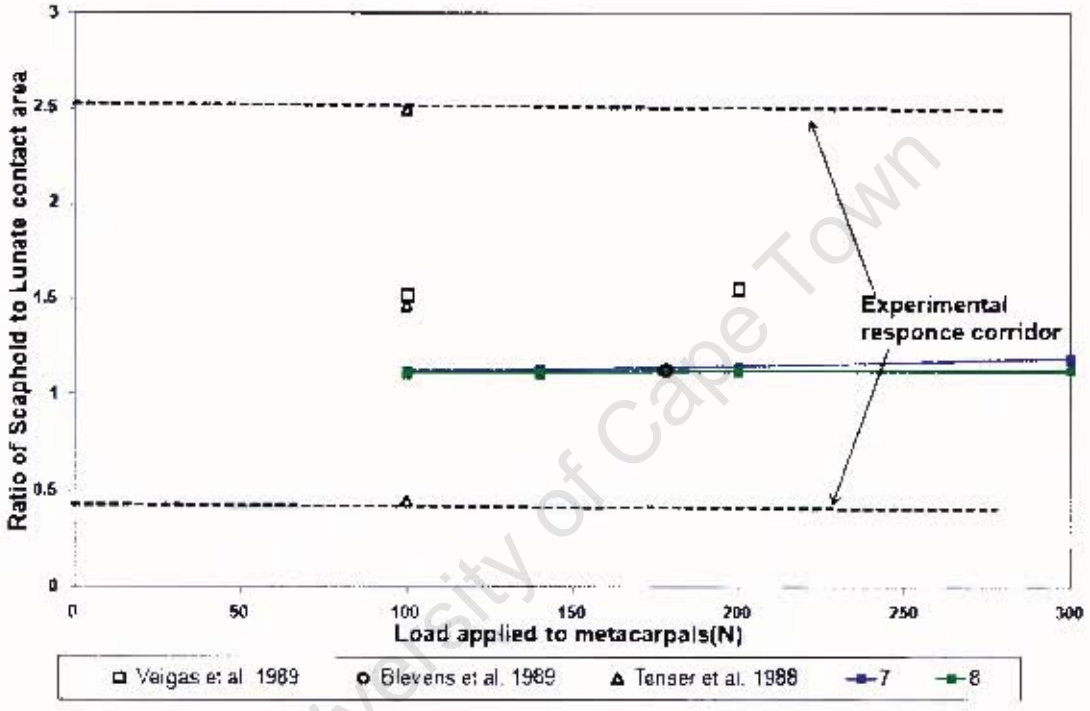

Figure 4.23: Ratio of Scaphoid to Lunate contact area versus load applied to the metacarpals, compared to experimental work from Veigas et al. [18, 87], Blevens et al. [48] and Tenser et al. [88].

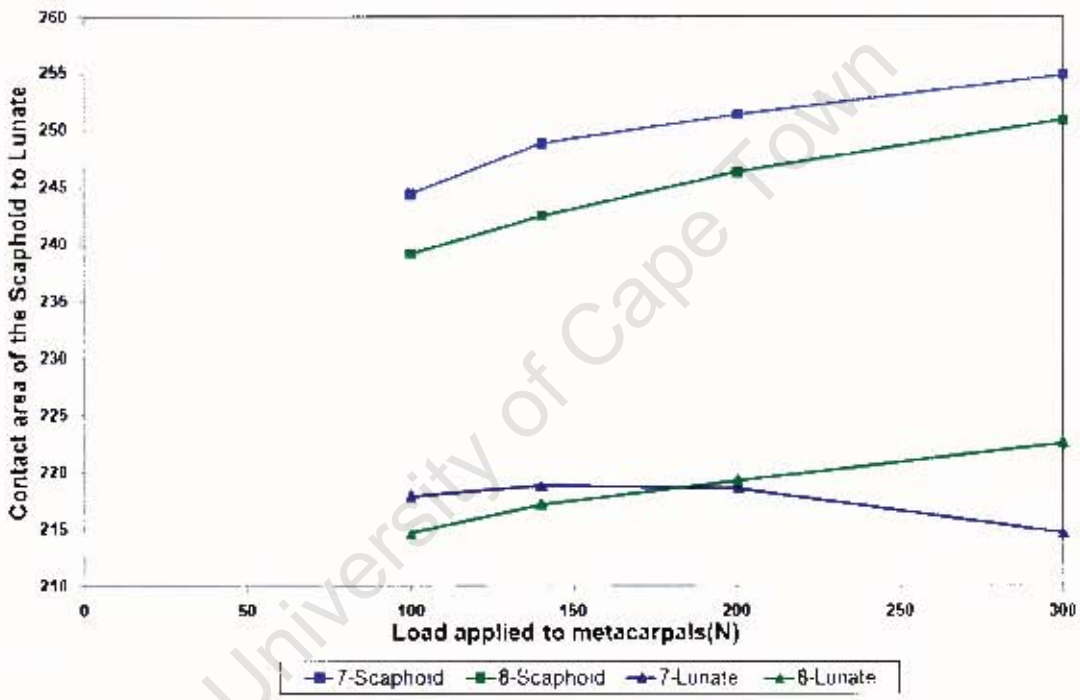

Figure 4.21: Scaphoid and Lunate contact area versus load applied to the metacarpals.

Model	Total/joint Figure 4.22	Scaphoid/Lunate Ratio Figure 4.23	Scaphoid Figure 4.24	Lunate Figure 4.24
7	Constant	Increase	Increase	Decrease
8	Constant	Constant	Increase	Increase

Table 4.10: General behaviour of the radio-carpal contact areas with increasing applied load (140-300N) for models 7 and 8.

Table 4.10 contains a summary of Models 7 and 8 results for the different graphs within the section. The models both fall within the experimental corridors of the total contact area and scaphoid to lunate ratios. The increase in the scaphoid to lunate contact area with increasing load for Model 7 seen in figure 4.23 is consistent with the increase in scaphoid contact area and decrease in lunate contact area. The scaphoid to lunate contact area ratio in Model 8 remains constant with increasing load. This behaviour is due to the increase of scaphoid and decrease of lunate contact area.

Validation criteria 2 - Contact pressure on the radius-carpal articular surface

The work conducted by Veigas et al. [18, 87] was chosen to validate the maximum contact pressure value determined by the model on its radius articular surface. The loads chosen to measure this value were at 100, 140, 200 and 300N. The load application is further discussed in section 3.7. The results for the behaviour of the different models at these loads is shown in table C.11 of Appendix C and figures 4.25 and 4.29.

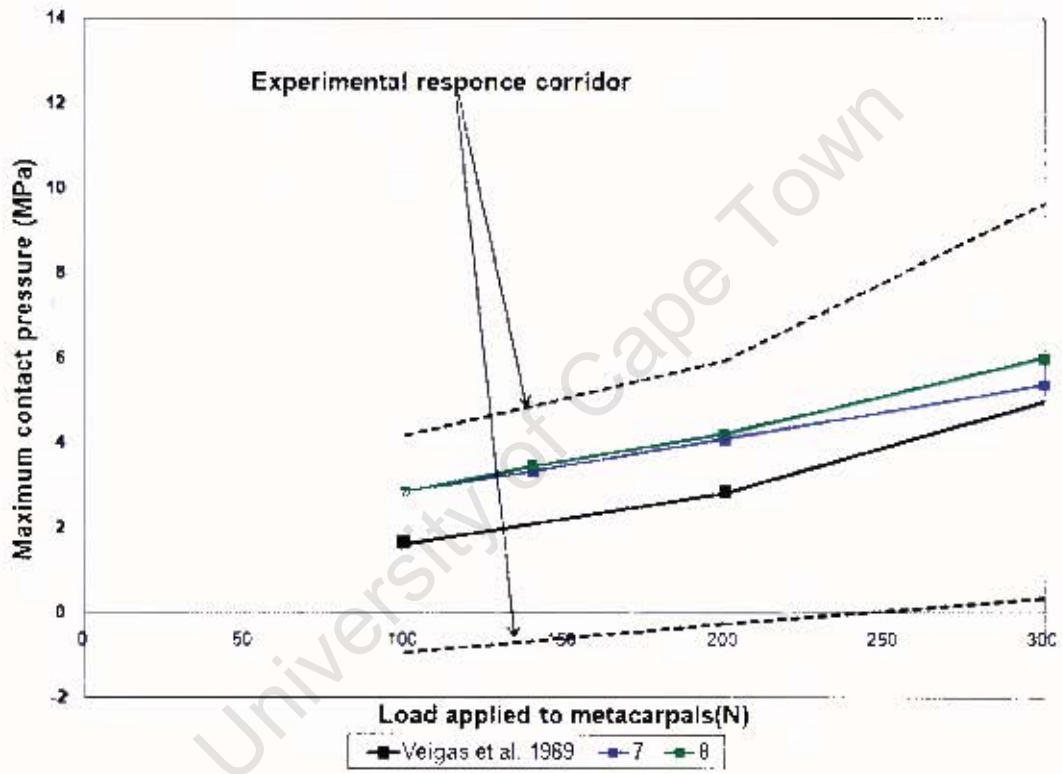

Figure 4.25: Maximum contact pressure versus load applied to the metacarpals, compared to experimental work from Veigas et al. [18, 87].

Figure 4.25 shows that the maximum contact pressure for Models 7 and 8 fit within the experimental corridor. The simulation result values follow the same trend as the experimental work, of an increasing contact pressure with increasing load. Both model results fall above the experimental average values at all loads. The possible reason for this occurrence is that the contact pressure-clearance relationship defined to represent cartilage in contact is based on how cartilage behaves at high loading rates. At these types of loading rates cartilage is stiffer than at equilibrium. The experimental results

were collected at equilibrium, hence the difference.

The maximum values of contact pressure for the radio-lunate and radio-scaphoid articulation were compared with the maximum values determined from experimental work conducted by Teurlings et al. [88]. The contact pressure on the radius articular surface was further validated by determining the contact pressure profile at an applied load of 300N along the midline of the radius. The path chosen is described in figure 4.26. The results of the study of Model 7 and 8 behaviours are described in table C.11 in Appendix C and figure 4.27. Figure 4.27 shows that the scaphoid maximum contact pressure falls within the experimental corridors. The lunate maximum contact pressure however is greater than the experimental corridors.

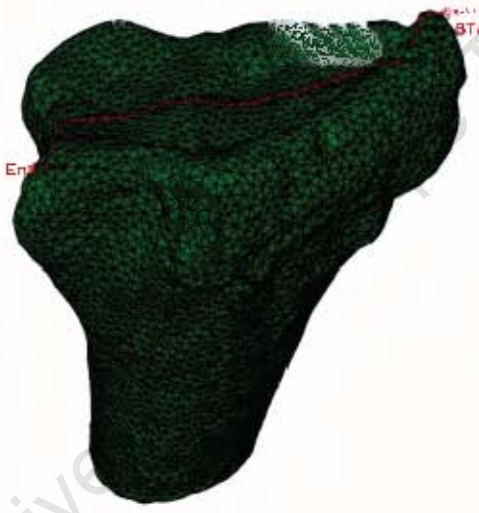

Figure 4.26: Path chosen along radius articular surface to represent the midline.

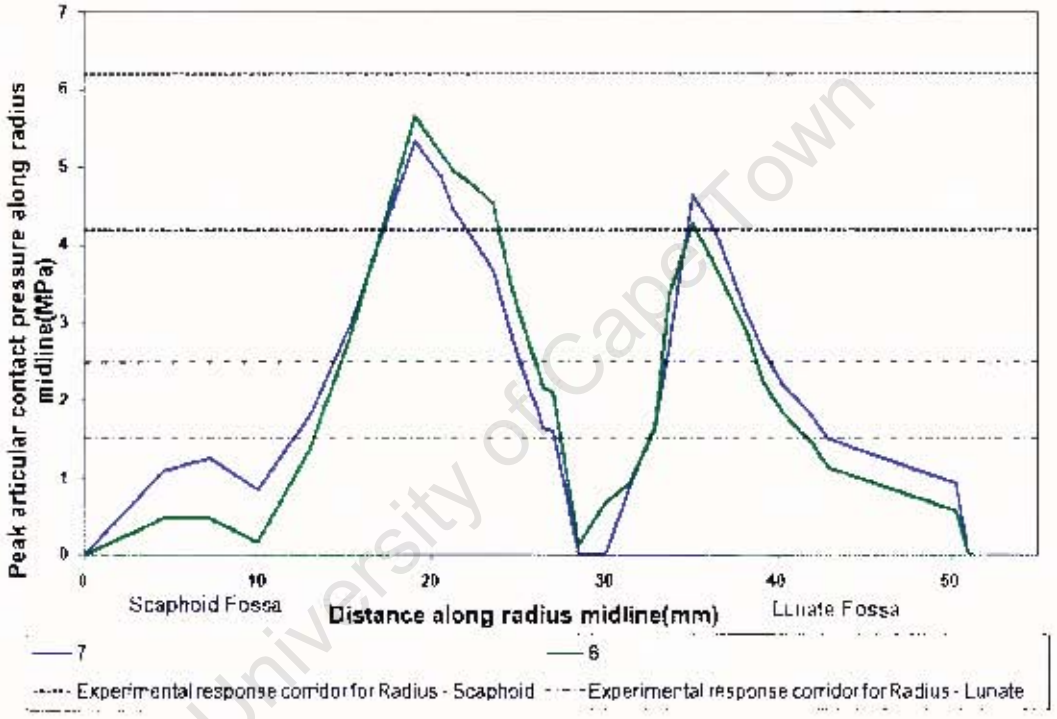

Figure 4.27: Peak articular contact pressure along the radius midline versus distance along the midline at a 300N load, compared to experimental work from Teurlings et al. [88].

The ratio of radio-scaphoid to radio-lunate maximum contact pressure is compared to experimental work from Blevens et al. [48] and 2-d RBSM results of Schuind et al. [32] and Horri et al. [33]. A comparison of the different models ratios to the experimental ratios is shown in figure 4.28. Figure 4.28 shows that both Models 7 and 8 fall within the experimental response corridor at a loads of 140 and 300N.

The scaphoid/lunate Contact Pressure ratio for both models decreases with increasing load. This decrease is consistent with the increase in scaphoid/lunate contact area ratio for Model 7 seen in table 4.10, due to contact area and pressure being directly proportional. This table also shows that Model 8's scaphoid/lunate contact area ratio remains constant with increasing load. Therefore the increase in contact pressure ratio associated with Model 8 is due to the pressure-clearance relationship. At a higher load (300N) Model 8's scaphoid undergoes a greater proximal displacement than at a load of 140N, causing a clearance that is smaller leading to an increase in contact pressure.

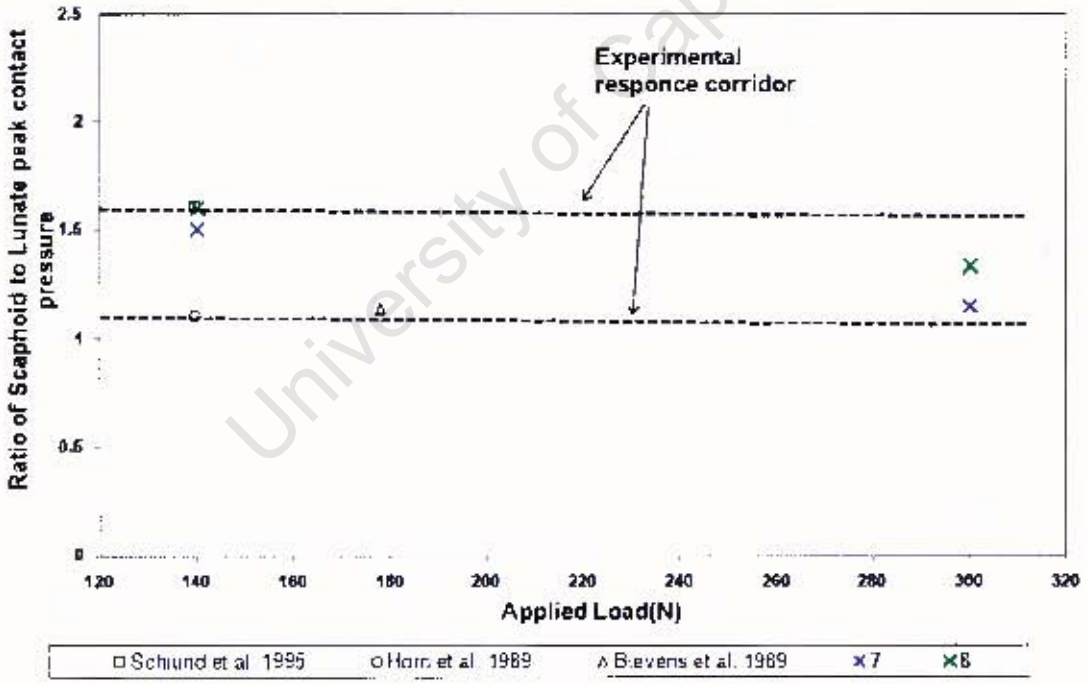

Figure 4.28: Ratio of Scaphoid to Lunate peak contact pressure versus applied load, compared to experimental work from Schuind et al. [32], Horri et al. [33] and Blevens et al. [48].

The contact pressure profiles are shown in figure 4.29. This figure contains a comparison of models 1, 7 and 8 at loads 140 and 300N. These profiles are the same for Models 7 and 8 at loads of 140N. The distribution of high and low pressure in Model 1 is consistent with the other models at this load. The maximum contact pressure on the scaphoid articulation is slightly less in model 1 than the other two models at this load. For the 300N load the maximum pressure for Model 8 is slightly higher than that for Model 7. A larger distribution of the maximum contact pressure is seen in Model 7 than Model 8 or Model 1. The distribution of contact pressure for the scaphoid contact in the ABGM is not symmetrical, between the palmar and dorsal aspects. This was noticed for both Models 7 and 8. The pressure profiles for the GSM and ABGM differer with regard to this, as the GSM is a half symmetry model with no distinction between dorsal and palmar sides.

The movement of the scaphoid and the lunate in Model 7 is unconstrained in all directions. This movement in Model 8 is unconstrained in the direction of the load but movement and rotation in the other directions depend on the stiffness of the centrally located connector elements within the carpal bones. The slight maximum contact pressure distribution differences between both these models could be due to slight differences in movement of the scaphoid and lunate.

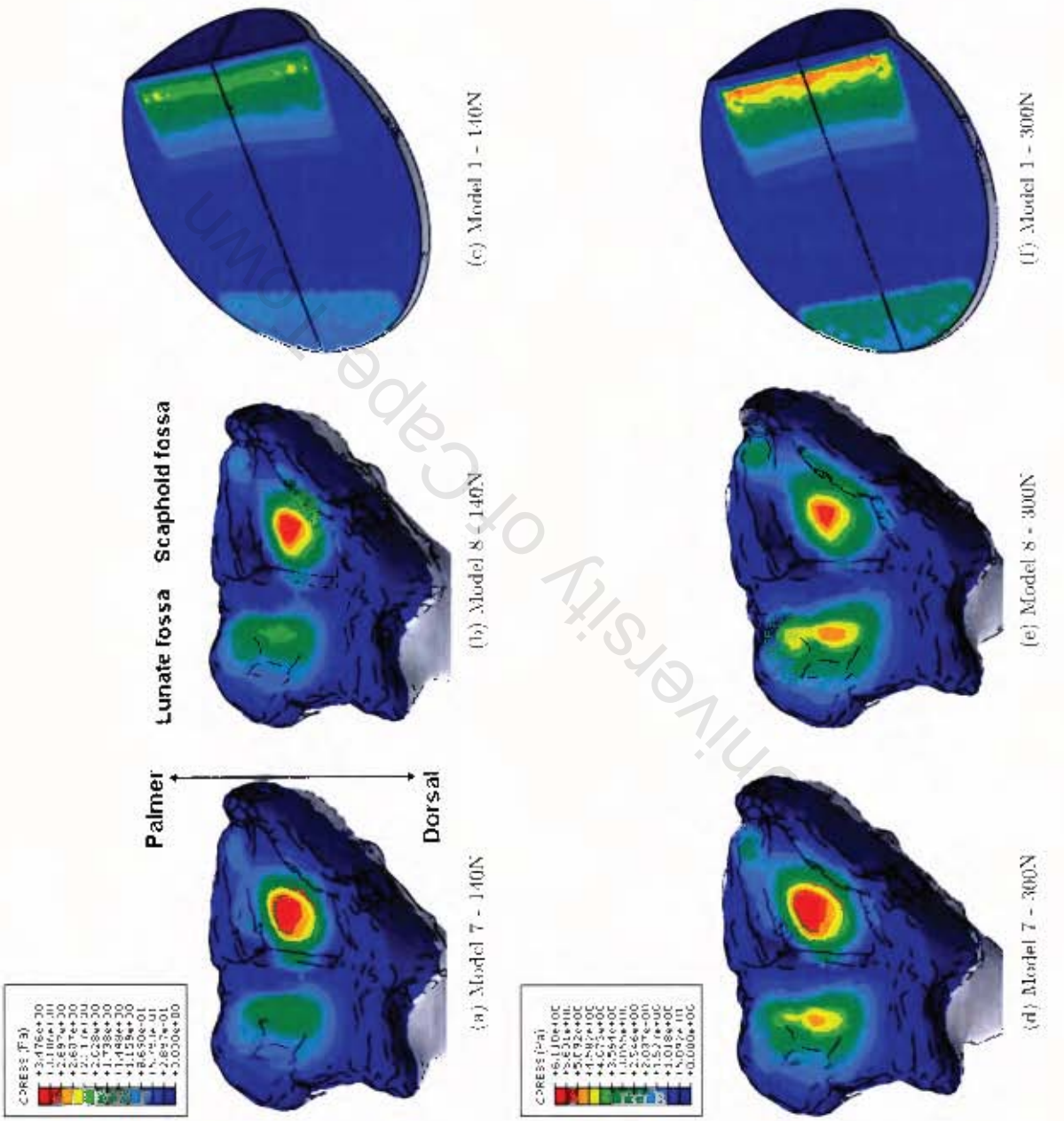

(a) Model 7 - 140N (b) Model 8 - 140N (c) Model 1 - 140N

(d) Model 7 - 300N (e) Model 8 - 300N (f) Model 1 - 300N

Figure 4.29: Contact pressure on the radius articular surface at an applied load of 140N and 300N.

Contact pressure in the mid-carpal articulation

The contact pressure distribution in the mid-carpal articulation has been compared qualitatively to that seen in the work of Majima et al. [34]. Models 7, 8 and the RBSM of Majima were loaded with 140N. Figure 4.30 shows these pressure distributions. The general locations of contact pressure in both Models 7 and 8 match that from the RBSM. Model 7 however experiences a greater area of maximum pressure on the triquetrum and lunate then Model 8. This is the case due to the bones of the distal carpal row in Model 7 being only allowed to move in the direction of the load. The carpal bones of Model 8 can undergo movement in all directions, the magnitude of this movement is controlled by the specified stiffness of the internal connector element. Due to this the contact area of the articular surfaces of Model 8 are slightly smaller than Model 7.

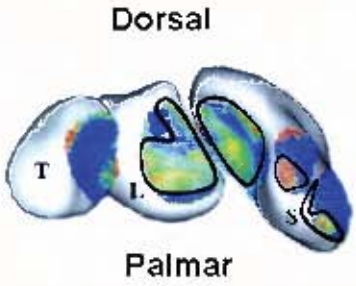

(a) Majima et al. [34] (red margins indicate regions of high contact pressure)

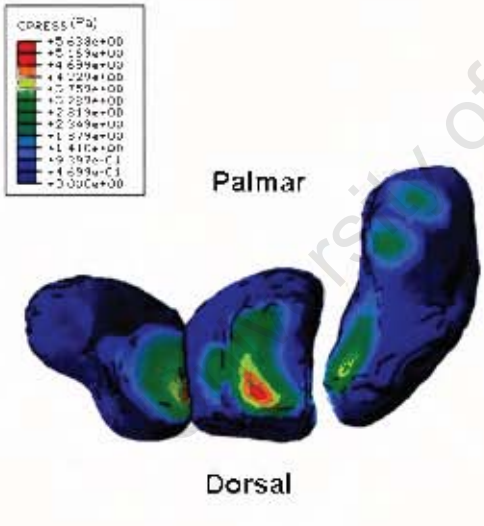

(b) Model 8

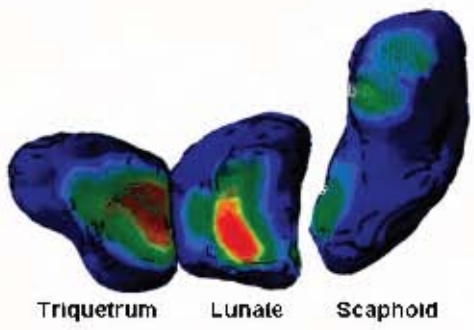

(c) Model 7

Figure 4.30: Contact pressure on the proximal articular surfaces of the mid-carpal joint at an applied load of 140N.

Validation criteria 3 - Ligament behaviour

The ligament behaviour was validated by a qualitative comparison with the behaviour of ligaments in the 2-d RBSM of Schuind et al. [32] at a load of 140N. The ligaments force transmissions as a percentage of the total load transmitted at 140N was determined, the results are presented in table 4.7 of Appendix C. Both the dorsal and palmar ligament behaviours are presented for Models 7 and 8. This validation work considers ligament tension to only be considered significant if it is above 5N. Table 4.11 contains the ligaments of the ABGM that carry significant tensile forces. Not all of the ligaments of the ABGM were modeled in the RBSM and vice versa. For both Model 7 and 8 the dorsal and palmar ligaments both carry significant tensile forces. This behaviour is consistent with the RBSM results.

The ligaments of the RBSM that carried significant loads were (in ascending order) the palmar Radio-lunate, palmar and dorsal Hamate-capitate, the palmar and dorsal Capitate-trapezoid. The ligament that carries the most significant load for both Model 7 and 8 is the Hamate-triquetrum ligament. The ligament that carries the second most load is the Lunate-hamate ligament. Both of these ligaments are related to the hamate so therefore the hamate must undergo a large amount of movement that needs to be restrained. This behaviour is inconsistent with the RBSM and GSM results, which both have the Radio-lunate ligament carrying the most significant load. Both of these 2-d models did not included the 3-d real bone geometry and constrained out of plane movements.

The proximal row of carpal bones of Model 7 had no constraint, and therefore could undergo random motion. The ligaments attached to these bones were the only restraint applied to them. Carpal bones of Model 8 were only constrained at a single node, this constraint was not enforced for motion in the direction of the applied load. These bones could undergo displacement and rotation in all directions, based on the stiffness value of connector used at this single node. Due to these carpal motions of both the models the ligaments carry significant tensile loads for a greater number of ligaments than the RBSM and GSM.

It is difficult to distinguish whether the ligaments of Model 7 or 8 carry more tensile forces. The most prominent difference is seen for the Triquetrum-hamate ligament. Whereby in Model 7 this ligament carries more than double the tensile load. Therefore this bone undergoes significant displacement in this model.

Ligament attachment		Model 7		Model 8	
		Ligament Tensile load (N)		Ligament Tensile load (N)	
Bone1	Bone2	Dorsal	Palmar	Dorsal	Palmar
Radius	Scaphoid	-	6.04	-	7.87
Lunate	Scaphoid	59.77	6.44	73.88	29.91
Lunate	Triquetrum	41.38	-	71.46	-
Capitate	Scaphoid	6.02	13.57	-	13.58
Capitate	Triquetrum	-	2.68	38.23	21.57
Capitate	Hamate	19.08	-	39.87	11.10
Capitate	Trapezium	-	-	-	-
Scaphoid	Trapezium	25.35	50.35	35.25	20.40
Scaphoid	Trapezoid	43.61	-	7.06	10.57
Triquetrum	Hamate	221.39	205.67	90.78	63.67
Lunate	Hamate	77.71	132.24	99.30	120.94
Lunate	Capitate	7.16	29.43	11.72	7.36
Capitate	Trapezoid	-	48.31	-	28.70
Trapezoid	Trapezium	-	5.54	37.15	16.37
Lunate	Radius	37.93	75.34	51.29	67.03

Table 4.11: Ligaments that carry significant tensile load when a 140N load is applied to the metacarpals for models 7 and 8.

Validation criteria 4 - Force transmission through the radio-carpal joint

The forth validation criteria was the percentage of total load transmitted through the mid-carpal and radio-carpal joints. The comparison between the stimulated and experimental force transmissions are presented in table 4.12. A load of 140N was chosen for the comparison as this is the load that was used for most of the experimental work. The load transmission between the radius-scaphoid and radius-lunate for a transmitted load of 140N is shown in figure 4.21. Table 4.12 shows that force transmitted through the radius to scaphoid and capitate to scaphoid and lunate articulations for both models falls within the experimental corridors. For the force transmitted through the radius to lunate articulation, only Model 8 falls within the experimental corridor. The force transmission through the scaphoid to trapezium and trapezoid articulation is smaller than the lowest boundary of the experimental corridor. The effect on load transmission ratios of the carpal constraint method used was that the constraint of a single node with carpal bones (Model 8) lead to a lower force transmission through the radio-lunate articulation.

Study	Distal Radio-carpal joint		Mid-carpal joint		
	Radio-scaphoid (%)	Radio-lunate (%)	Triquetrum to Scaphoid (%)	Capitate to Scaphoid &Lunate (%)	Scaphoid to Trapezoid &Trapezium (%)
Majima et al. [34]	52	42	-	-	-
Horri et al. [33]	52±9	37±6	-	59±7	36±6
Schuind et al. [32]	63±9	40±7	-	79±14	40±5
Veigas et al. [18]	60	40	-	-	-
Blevens et al. [48]	34	26	-	-	-
Experimental corridor	34-72	26-47	-	52-93	30-45
Models 7	50	50	6	76	18
Model 8	68	32	8	80	12

Table 4.12: Load transmission through the radio-carpal and mid-carpal joints.

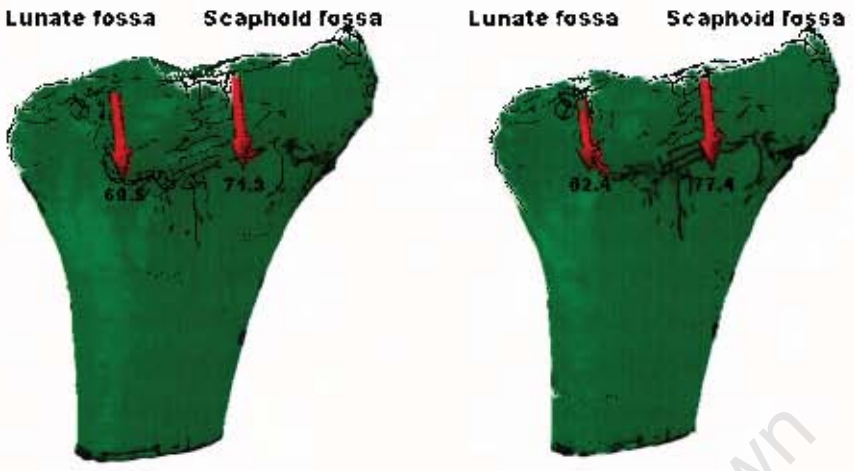

(a) Model 7 (b) Model 8

Figure 4.31: Vertical component of the load transmission through the radius-carpal joint at a 140N load.

Summary of validation criteria results for the Accurate Bone Geometry Model

The ABGM was constructed using the modelling parameters (BEFT and ligament stiffness definition B) used for GSM Model 1. The ABGM was constructed using data from a volunteer's CT scan (Appendix D), by validating this model the modelling parameters are further validated. The validation criteria used were the same as for the GSM. The first validation criteria considered was the contact area of scaphoid and lunate on the radius articular surface. Model 7 (distal carpal rows motion confined to only in the direction of the applied load) and 8 (single node in all the carpal bones translational and rotational motion in directions other than the applied load direction constrained using spring connectors) results fit well within the experimental corridors for the two different parameters of total contact area/joint area ratio (figure 4.22) and scaphoid/lunate contact area ratio (figure 4.23).

The second validation criteria considered was the maximum contact pressure on the radius articular surface. Models 7 and 8 fit within the experimental corridors for two parameters of the three used in this criterion. These two parameters were total maximum contact pressure with increasing load (figure 4.25) and ratio of scaphoid to lunate maximum pressure (figure 4.28). There were three parameters considered for this criterion. The third parameter was the individual maximum contact pressures of the radius-scaphoid and radius-lunate articulations, both models only fell within the boundaries for the radius-scaphoid (figure 4.27). Both models were greater than the maximum value boundaries for the radius-lunate. The contact pressure distribution in the mid-carpal joint was qualitatively compared to the work of Majima et al. [34]. The general locations of contact pressure match.

The third criterion was the a qualitative comparison as to which ligament carried the most tensile force in the model (table 4.11). This ligament that carried the most tensile load was the hamate-triquetrum ligament for both models. This was not the ligament that carried the largest tensile load in the validation work. The difference is thought to be due to the validation work being a 2-d model therefore significant out of plane movement that occurs realistically is restricted.

The final criterion was the force transmission percentages through the radio-carpal and mid-carpal joints (table 4.12). Model 7 and 8's radio-carpal force transmission percentages are within the experimental boundaries. The capitate-lunate and scaphoid percentages are also within the boundary. The scaphoid-trapezoid and trapezium force transmission for

both models is below the lower boundary of the experimental work.

Models 7 and 8 fell within or close to the most parameter boundaries of criteria one, two and four. Validation criteria three was decided to be ineffective as a comparative criterion. Even though both Models 7 and 8 are considered to be validated, Model 7 allows unconstrained movement of the scaphoid and lunate which occurs realistically [42].

4.2.3 Comparison between Geometrically Simplified and Accurate Bone Geometry Model results

The GSM and ABGM were developed to simulate wrist joint injury resulting from falls onto the outstretched hand. A Colles' fracture (fracture of the distal radius, section 2.8.3) was the injury most interested in, as this was noted to be the injury that had the highest occurrence after a fall. von Mises and Maximum principal stress can be used to predict the regions where radius bone failure may occur [37]. Therefore, a comparison between the GSM and ABGM results for these two output variables was conducted, to investigate how advantageous geometrical complexity was in predicting these variables. The GSM was developed as the run time and costs that would be associated with accruing a CT-scan for each individual subject for the ABGM, are high. The comparison between these two models was undertaken to identify how much the results of the GSM and the ABGM differed.

The GSM and ABGM were validated under physiological loads. The main validation criteria considered were maximum contact pressure and contact area on the radius articular surface (Veigas et al. [18, 87]). Validating these criteria shows that the models were undergoing contact interactions realistically. Models 1 (GSM) and 7 (ABGM) were chosen for the comparison study as these were models that behaved most like the experimental work (Veigas et al. [18, 87] average values). Table 4.13 contains the results of the comparative study between the two models at applied loads of 100 and 200N. The values in the table are the maximum values for the radius bone. A ratio of 1 would indicate an exact match.

The contact area and maximum radius Maximum principal stress values compare very well between the two models at both loads. The contact area difference at a load of 100N between the models and the experimental results (Veigas et al. [18, 87] average values) for both the GSM and ABGM, is due to cartilage being modelled as nearly incompressible and the experimental work's cartilage would have been at equilibrium, hence compressible.

A comparison of the Maximum principal stress in Model 1 with the result from Pietruszczak et al. [37] was carried out at a load of 700N (the minimum boundary of fracture loads). Figure 4.32 has this result, the GSM maximum Maximum principal stress are in similar locations on the medial side of the radius in the distal portion where the diameter changes and at the bottom near the supports. This is the location of a typical Colles' fracture (figure 2.39). This comparison was undertaken to see the difference in

Load(N)	100			200		
Model	M1/Exp	M7/Exp	M7/M1	M1/Exp	M7/Exp	M7/M1
Contact Pressure (Mpa)	1.10	1.77	1.62	1.37	1.44	1.05
Contact area/total joint area	2.17	2.00	0.92	1.82	1.68	0.93
von Mises Stress (Mpa)	-	-	1.35	-	-	1.21
Maximum principal stress (Mpa)	-	-	0.99	-	-	0.97

Table 4.13: A comparison of Model 1 and 7 radius results. Exp, is the average experimental value from Veigas et al. [18, 87]

Maximum principal stress between loading through the metacarpals (Model 1) and directly applying load to the radius (Pietruszczak et al. [37]). The GSM lead to a a lower maximum stress value (93MPa compared to 120MPa). Stress distributions for the ABGM at a load of 200N is shown in figures 4.35, 4.33, 4.34. The region of maximum in the radius, shown by the red circle in figure 4.33 is the same location as that in figure 4.32. The maximum von Misses stress (figure 4.34) located in the radius corresponds well with that of the radius in the GSM (figure 4.8). This is the lateral side of the radius, where the diameter of the radius decreases and maximum compression is seen.

There is satisfactory correlation between the location and magnitude of Contact, von Mises (maximum on lateral side of radius undergoing compression) and Maximum principal stress (maximum on medial side of radius undergoing tension) between the GSM and the ABGM. The GSM (Model 1) and the ABGM (Model 7) can predict transfer forces and undergo contact interactions in the wrist joint. Both can also give an indication of the location and load magnitude that would cause a Colles'fracture.

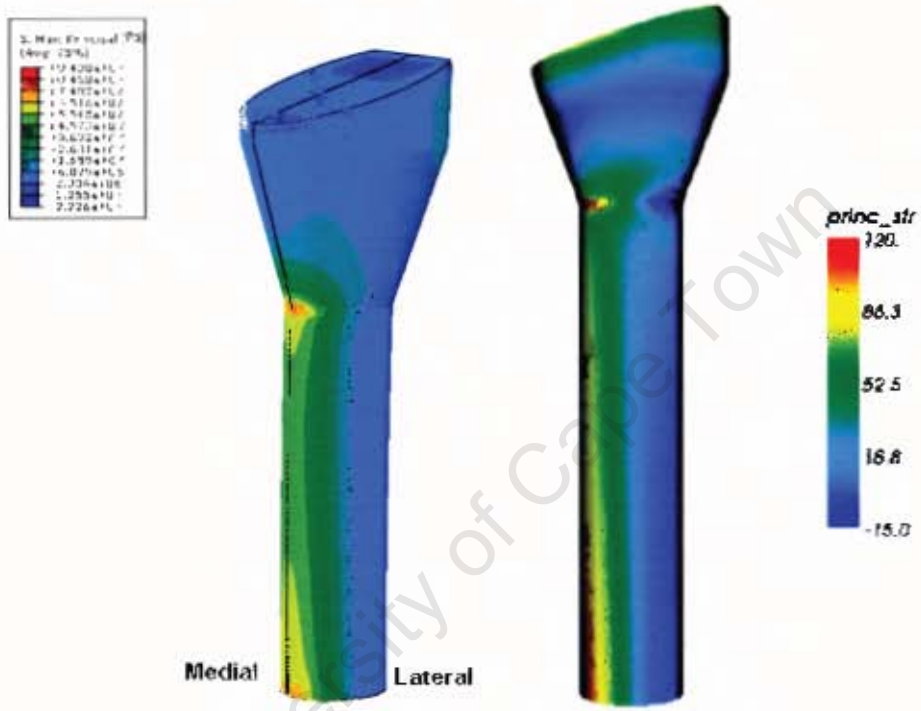

(a) Model 1 (b) Pietruszczak et al.

Figure 4.32: Comparison of Maximum principal Stress in the Model 1 and the results from the study of Pietruszczak et al. [37] at an applied load of 700N.

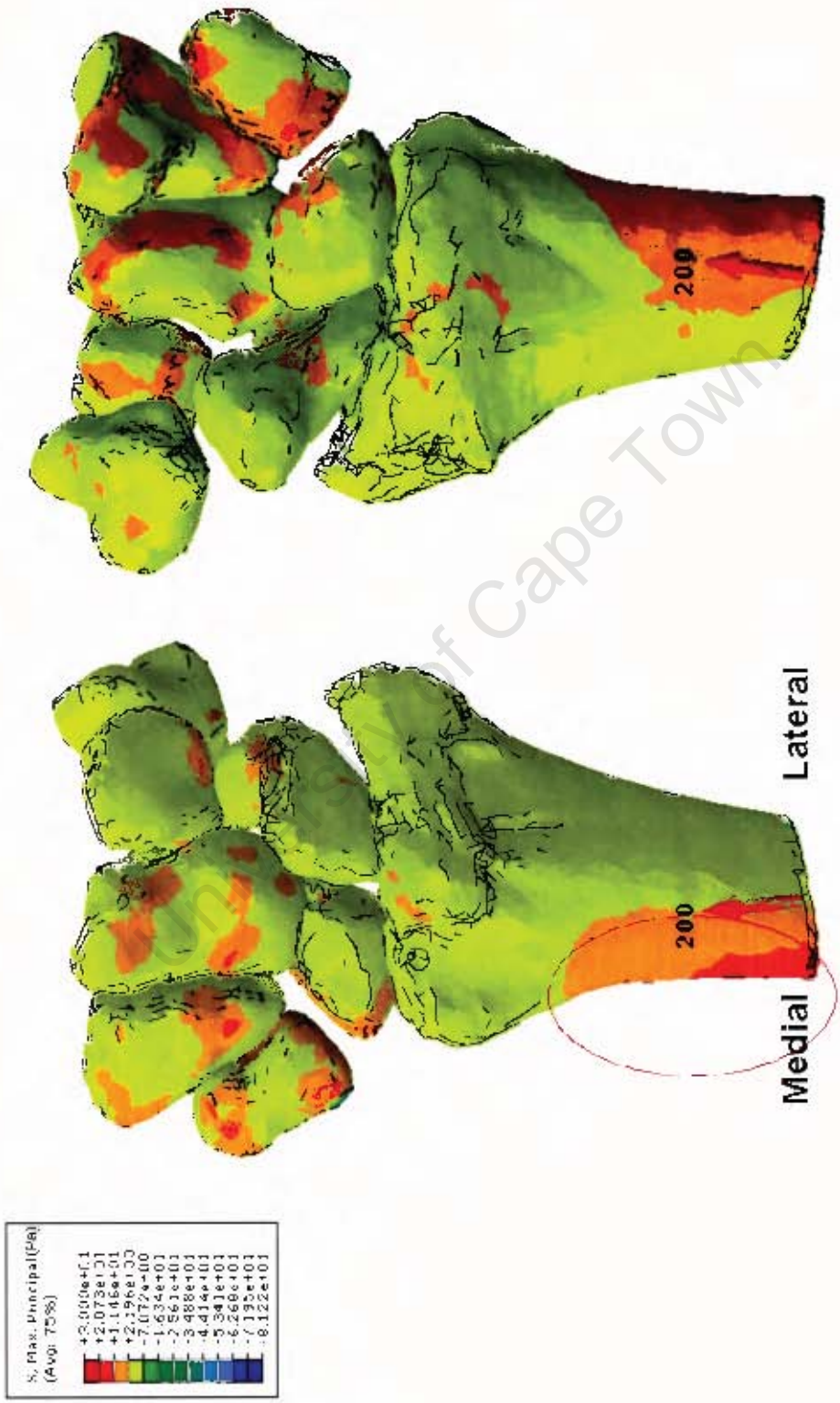

Figure 4.33: Maximum principal stress in Model 7 at an applied load of 200N.

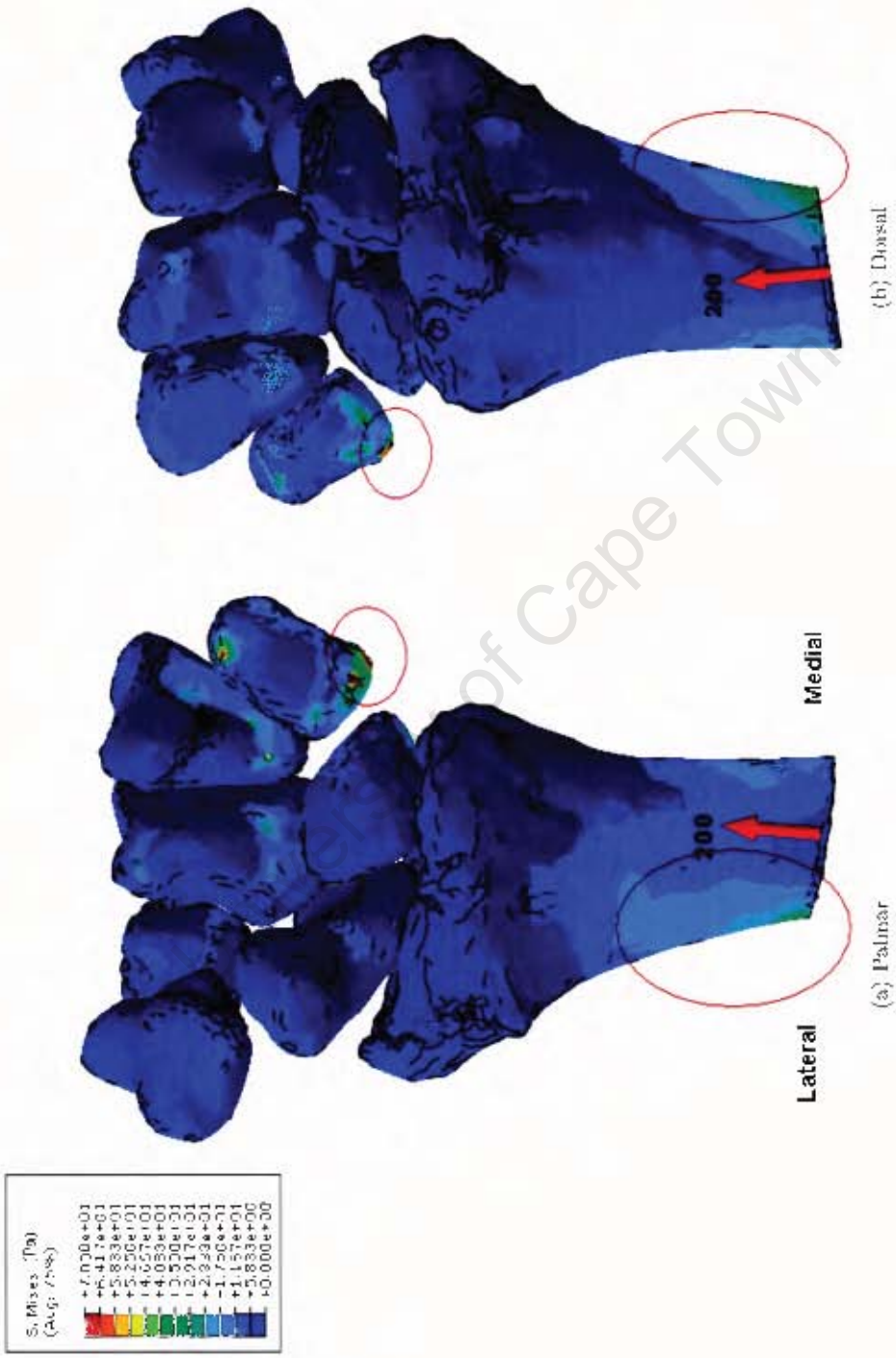

(a) Palmar (b) Dorsal

Figure 4.34: von Mises stress in Model 7 at an applied load of 200N.

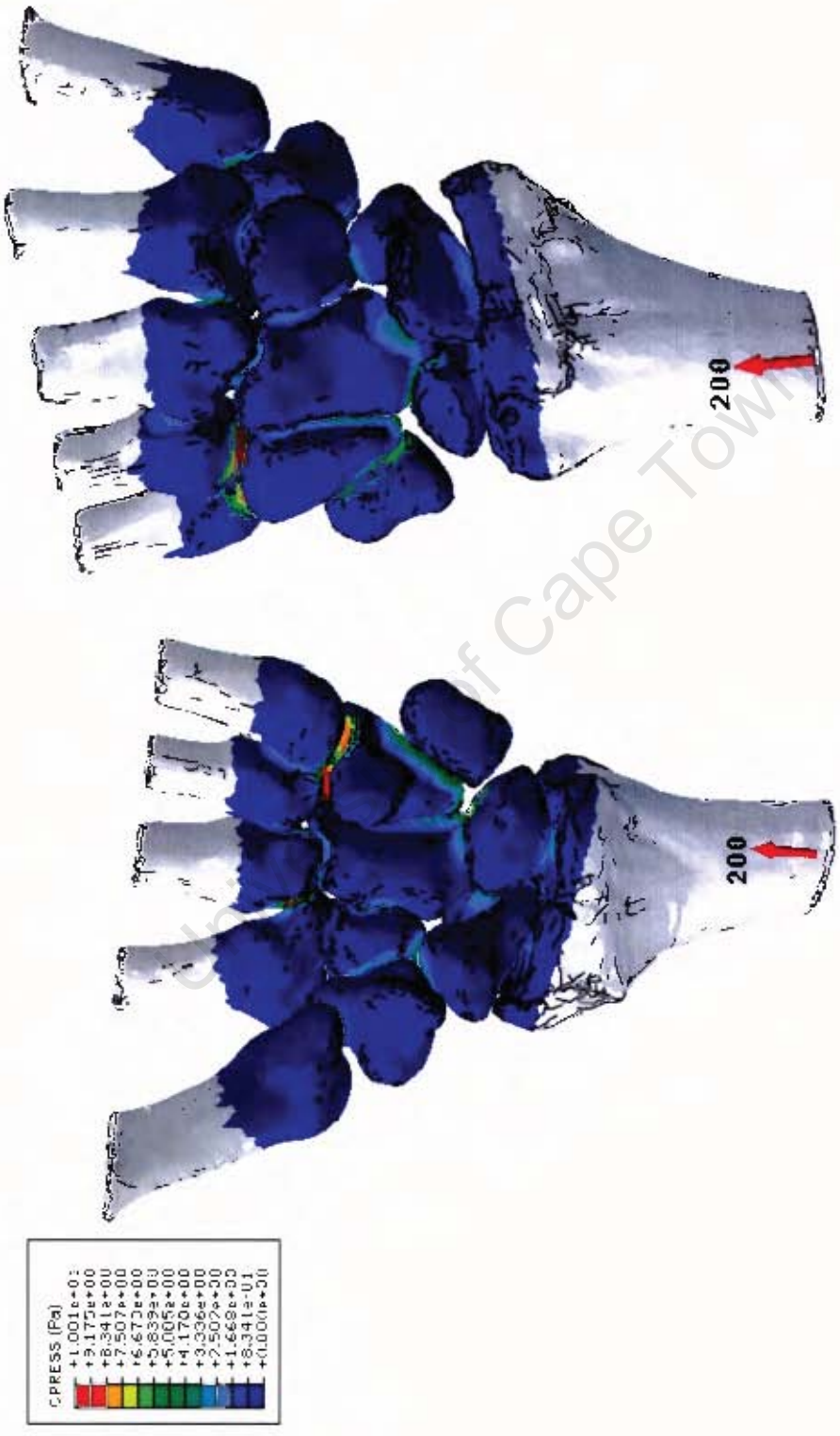

(a) Palmar (b) Dorsal

Figure 4.35: Contact pressure in Model 7 at an applied load of 200N.

Chapter 5

Summary

A Colles' fracture (fracture of the distal radius, section 2.8.3) has been determined statistically to be the most common type of injury to occur following a fall onto the outstretched hand [2, 3, 4, 5, 6, 7, 8, 2, 9, 10]. Forces applied to the hand during a fall are transmitted to the radius through the wrist joint. The bones involved in this force transmission pathway are the metacarpals, carpals and finally the radius.

The magnitude of force applied to the wrist after a fall have been studied experimentally (subjects falling onto force plates) [11, 12, 13, 14, 15, 16] and through the use of Rigid Body Spring Models [11, 14, 30, 31, 32, 33, 34]. The pressure and force transfer through the wrist joint has also been studied through various loading methods of cadaveric wrist joints [18, 19, 20, 21]. These studies have been used in the validation of finite element wrist joint models developed previously [22, 23, 24, 25, 26, 27, 28, 29].

The work conducted for this thesis involved developing two models to simulate the force transmission from the metacarpals, through the wrist joint, to the radius bone. These models also give insight into the contact stress distributions within the wrist joint. The finite element models developed were a geometrically simplified model (GSM) and a geometrically complex model (ABGM). The ABGM involved geometry and material properties acquired from a volunteer's CT scan (Appendix D).

Summary of the GSM results

The GSM involved an approximation of real bone geometry, with material properties that could be varied. The model was loaded and the results were compared to experimental work from the literature as a means of validating the model. Prior to the validation study, a material sensitivity study (cartilage, cortical and cancellous bone) was undertaken.

Summary of material sensitivity study results

This study considered the effects of changing the parameters of each individual material property (cartilage, cancellous and cortical bone) on the maximum stress and pressure outputs of the model (von Mises stress, Maximum principal stress, Contact stress and contact area). The material properties chosen for these validations were based on the range of values presented in the literature (table 4.2). Linear elastic material properties were defined for bone. Both hyperelastic and linear material properties were defined for cartilage. For studies that involved linear material properties the effects of changing the Young's modulus or Poisson's ratio of each individual property was studied whilst keeping the other model parameters constant. For studies that had a hyperelastic cartilage definition the effect of changing the Mooney-Rivlin constants was undertaken. The conclusions drawn from these material studies were as follows:

When linear elastic material properties were used for cartilage, an increase in Young's modulus (figure 4.3) of the cartilage lead to an increase in contact pressure and a slight decrease in the radio-carpal contact area. This increase had no effect on the location and magnitude of von Mises, Maximum principal stress. The location of these maximum stress values was consistent with the region of the radius bone were Colles' fracture typically occurs. A variation in Poisson's ratio of cartilage had no significant effect on the magnitude or location of any of the maximum stress, pressure or contact area variables.

The Mooney-Rivlin hyperelastic cartilage definition was used. The effect of varying the Mooney-Rivlin constants (figure 4.6) were carried out. An increase in the magnitude of both constants had the same effect as the increase in Young's Modulus of the cartilage. The only variable with a substantial increase was the contact pressure. The magnitude and location of the maximum stress, pressure and contact area variables remain relatively constant.

An increase in the Young's Modulus of cortical bone (figure 4.7) lead to an increase

in the magnitude of maximum von Mises stress. The location of maximum stress was consistent among the cartilage and the cortical bone studies. Where maximum von Mises and Maximum principal stress was located in the cortical bone region of the radius were typical Colles' fracture occurs. The maximum contact stress was located consistently on the radial articular surface.

An increase in the Young's modulus of cancellous bone (figure 4.9) lead to a decrease in magnitude of von Mises, Maximum. The location of maximum von Mises stress in these studies occurred on the scaphoid and the cortical bone region of the radius were typical Colles' fracture occurs at low values of Young's modulus. At higher values only the cortical bone region of the radius were typical Colles' fracture occurs. A decrease in Poisson's ratio of cancellous bone did not lead to a significant decrease in magnitude or location of any of the output values.

Summary of validation results

Six different versions of the GSM were studied. Variations in ligament stiffness and cartilage material property definitions and lunate constrainment methods were studied (table 4.4). The validation of the GSM was conducted by a comparison of the models results with experimental work conducted on cadavers and RBSMs (table 4.1). The cadaveric experimental work involved the measurement of contact pressure and area through the radio-carpal joint using pressure sensitive film. The validation criteria chosen for comparison were the contact pressure and area in the radio-carpal articulation, the ligament behaviour and the force transmission ratios in the radio-carpal and the mid-carpal articulations.

The first validation criteria considered was the contact area of the scaphoid and lunate bones on the radius articular surface (figures 4.11 and 4.11). Validation was carried out by comparison with experimental work from Veigas et al. [18, 87], Blevens et al. [48] and Tenser et al. [88]. The second validation criteria considered was the maximum contact pressure on the radius articular surface (figures 4.15, 4.17 and 4.18). Validation for this criterion was carried out with work from Veigas et al. [18, 87], Tenser et al. [88], Blevens et al. [48], Schuind et al. [32] and Horri et al. [33]. The third criterion was the force transmission through the wrist ligaments, compared with results from Schuind et al. [32] (table 4.7). The final criterion was the force transmission percentages through the radio-carpal and mid-carpal joints. The comparison was made with results from Majima et al. [34], Horri et al. [33], Schuind et al. [32], Veigas et al. [18] and Blevens et al. [48](table

4.8).

The parameters of Model 1 were chosen to be used in the ABGM. The reason was this model's results fell within or close to all four validation criteria boundaries. The parameters of Model 1 were; the ligament stiffness definition of Fischli et al. [84], linear elastic material property definition for cartilage and the lunate was supported using beam on elastic foundation theory (simulating the shock absorbing capabilities of the TFCC).

Summary of the ABGM results

The ABGM was constructed using the modelling parameters (ligament stiffness definition, cartilage definition and lunate confinement method) of Model 1. The ABGM bone geometry and material properties were determined from a volunteer's CT scan (Appendix D). The four validation criteria used were the same as for the GSM. The first validation criteria is shown in figures 4.22 and 4.23, the second shown in figures 4.25, 4.28 and 4.27, the third in table 4.11 and the final in table 4.12.

There were two ABGM models studied that differed in the method used for the constraint of the carpal bones (Table 4.9). Model 7's distal row's motion was constrained so that only movement in the direction of the load was allowed. Model 8 had only a single node in the center of each of the carpal bones constrained such that motion (in directions other than the load application direction) of that node was controlled by springs of defined stiffness(translational and rotational). Models 7 and 8 fell within validation criteria one, two and four boundaries. Validation criteria three was decided to be ineffective as a comparative criterion for the 3-d ABGM as it involved a 2-d model therefore significant out of plane bone movement was restricted. Even though both Models 7 and 8 are considered to be validated, Model 7 allows unconstrained movement of the scaphoid and lunate which occurs realistically [42].

Summary of comparison between the GSM and ABGM results

A comparison between the GSM and the ABGM was carried out to investigate how advantageous geometrical complexity was in predicting the model output variables (von Mises and Maximum principal stress in the radius) and the location of a Colles' fracture. The GSM and ABGM were validated under physiological loads. Validation criteria one

and two were the validation criteria used for the comparative study. These were the maximum contact pressure and contact area on the radius articular surface (Veigas et al. [18, 87]). Validating these criteria shows that the models were undergoing contact interactions realistically. Models 1 (GSM) and 7 (ABGM) were chosen for the comparison as these were models that behaved most like the experimental work (Veigas et al. [18, 87] average values). Table 4.13 contains the results of the comparative study between the two models.

von Mises and Maximum principal stress were output variables considered most important, as these indicate the regions where radius bone failure may occur [37]. A comparative ratio of one indicates that Models 1 and 7 behave exactly the same. Model 1 and 7 had comparative ratios close to one for contact pressure (validation criteria two), von Mises and Maximum principal stress. The contact area (validation criteria one) compared well between the two models and the experimental work at the greater load. At lower loads the contact area comparative ratio was two for both the GSM and ABGM (both FE-models results were almost double the experimental results), this is due to cartilage being modelled as nearly incompressible and the experimental work's cartilage would have been at equilibrium, hence compressible. Another reason could be due to the geometry differences between rounded contacting regions of real bones and the flat contacting regions of the GSM. Both these reasons would cause the experiential work to have a lower contact area than the model.

The conclusion drawn was that both Model 1(GSM) and 7 (ABGM) give good predictions of the location of Colles' fracture, undergo contact interactions realistically and compare satisfactory in their prediction of the magnitude of von Mises and Maximum principal stress. Therefore, the geometric complexity of the ABGM is advantageous in that the distribution of stress and pressure can be seen in a subject's actual bone geometry and material property distribution, allowing an exact indication of what applied load and load direction leads to the location region of the subject's bone that is experiencing a high stress. The GSM however can be used in cases where a CT scan is unattainable and the overall material properties of the subjects joint are known, allowing the prediction of the magnitude of maximum stress within the joint, for a given set of material properties.

Chapter 6

Recommendations

The models developed in this thesis can be used in a study of impact loading that would occur during a fall onto the outstretched hand scenario. Future studies should look at the contribution of muscle action to the biomechanics of the wrist. The load dissipation effects of the palmer soft tissue should also be incorporated into the model. The mechanism between a distal radius fracture and a scaphoid fracture is not well understood. These are the fractures to occur most frequently in statistical data gathered from falls onto an outstretched hand. This model could be used to look at the fracture mechanisms of these two bones. The incorporation of a isotropic failure theory or a complex bone material model to study these failure mechanisms could be of benefit.

The wrist joint in these models was created with the wrist in the neutral position which is not the normal position during a fall event. An improvement would be to model the wrist in an extended position as this is the more likely scenario during a fall. Future modeling should be conducted with a CT-scan with the wrist in the extended position to eliminate any doubts of the effect of wrist position on its ability to bear compressive forces. During an analysis of an actual fall event, a dynamic or quasi-static analysis should be employed and the notion of the rate-sensitivity of the material properties needs to be looked at. A dynamic analysis should be carried out due to the significant inertial forces experienced from the wrist's acceleration over a very short period of time. Strain rate dependent material and ligament behaviour should be incorporated into the model. Bone mineral density factors relating to falls should be studied with reference to the case of osteoporotic bone of postmenopausal women and young girls.

The bone geometry for an individual should be determined using both a CT-scan and an MRI-scan to determine accurate ligament attachment sites and the soft tissue geometry (cartilage and fascia) of the joint. The MRI-scan provides details of soft tissue properties. The purpose of improving the model to include all the biological tissue occurring in a real joint, is for more realistic stress to be predicted.

References

[1] Wrist anatomy. http://www.eorthopod.com/images/ContentImages/wrist/wrist_anatomy/wrist_anatomy_bones04.jpg, 21/03/2009.

[2] M. Kramheft and S. Bedtker. Epidemiology of distal forearm fractures in danish children. *Acta Orthopaedica*, 59(5):577–559, 1988.

[3] Childsafe. http://www.childsafe.org.za/stats.htm, 22/05/2009.

[4] A. Goulding, R. Cannan, S.M. Williams, E.J. Gold, R.W. Taylor, and N.J. Lewis-Barned. Bone mineral density in girls with forearm fractures. *Journal of Bone and Mineral Research*, 13(1):142–148, 1998.

[5] P.W. Thompson, J. Taylor, and A. Dawson. A annual incidence and seasonal variation of fractures of the distal radius in men and women 25 years in droset, uk. *International Journal of the Care if the Injured*, 35:462–466, 2004.

[6] K.M. DeGoede, J.A. Ashton-Miller, and A.B. Schultz. Fall–related upper body injuries in the older adult: a review of the biomechanical issues. *Journal of Biomechanics*, 36:1043–1053, 2003.

[7] C.M. Court-Brown and B. Caeser. Epidemiology of adult fractures: A review. *International Journal of the Care if the Injured*, 37:691–697, 2006.

[8] M.T. Vogt, J.A. Cauley, M.M. Tomaino, K. Stone, J.R. Williams, and J.H. Erndon. Distal radius fracture in olderwomen:a ten year follow-up study of descriptive characteristics and risk factors. the study of osteoporotic fractures. *Journal of the American Geriatrics Society*, 50:97–103, 2002.

[9] C. Hill, M. Riaz, A. Mozzam, and M.D. Brennen. A regional audit off hand and wrist injuries: A study of 4873 injuries. *Journal of Hand Surgery*, 23B(2):196–200, 1998.

[10] Ski-injury. http://www.ski-injury.com/specific-injuries/wrist, 15/02/2009.

[11] J. Chiu and S.N. Robonovitch. Prediction of upper extremity impact forces during falls on the outstretched hand. outstretched hand. *Journal of Biomechanics*, 31:1169–1176, 1998.

[12] K.M. Degoede, J.A. Ashton-Miller, A.B. Schultz, and N.B. Alexander. Biomechanical factors affecting the peak hand reaction force during the bimanual arrest of a moving mass. *Journal of Biomechanical Engineering*, 124:107–112, 2002.

[13] P.H. Chou, Y.L. Chou, C.J. Lin, F.C. Su, S.Z. Lou, C.F. Lin, and G.F. Haung. Effect of elbow flexion on the upper extremity impact forces during a fall. *Clinical Biomechanics*, 16:888–894, 2001.

[14] K.M. Degoege and J.A. Ashton-Miller. Fall arrest strategy affects peak hand impact force in a forward fall. *Journal of Biomechanics*, 35:843–848, 2002.

[15] K.J. Kim and J.A. Ashton-Miller. Biomechanics of fall arrest using the upper extremity: age differences. *Clinical Biomechanics*, 18:311–318, 2003.

[16] K.L. Troy and M.D. Grabiner. Symmetric ground impact of the hands after a trip-induced fall: Experimental kinematics and kinetics. *Clinical Biomechanics*, 22:1088–1095, 2007.

[17] M.E. Muller, C.E. Webber, and M.L. Bouxsein. 'predicting the failure load of the distal radius. *Osteoporos International*, 14:345–352, 2003.

[18] S.F. Viegas and R.M. Patterson. Load mechanics of the wrist. *Hand Clinics*, 13(1):109–128, 1997.

[19] H. Shaaban, G. Giakas, M. Bolyon, R. Williams, and L.R. Scheker. The distal radioulnar joint as a load-bearing mechanism - a biomechanical study. *Journal of Hand Surgery*, 29(A):85–95, 1994.

[20] F.W. Ekanstam, A.K. Palmer, and R.R. Glisson. The load on the radius and ulna in different positions of the wrist and forearm: A cadaver study. *Acta Orthopaedica*, 55:363–365, 1984.

[21] D.A. Rickli, P. Honigmann, R. Babst, A. Cristalli, M.M. Morlock, and T. Mittlmeier. Intra-articular pressure measurement in the radioulnocarpal joint using a novel sensor: in vitro and in vivo results. *The Journal of Hand Surgery*, 32(A):67–75, 2007.

[22] P. Ledoux, D. Lamblin, and R. Targowski. Modifications to the mechanical behaviour of the wrist after fracture of the scaphoid modeling by finite element analysis. *Acta Orthopaedica Belgica*, 67:236–241, 2001.

[23] T. Miyake, H. Hashizume, H. Inque, Q. Shi, and N. Nagayama. Malunited colles' fracture: Analysis of stress distribution. *Journal of Hand Surgery*, 19(B):737–742, 1994.

[24] M. Oda, H. Hashizume, T. Miyake, H. Ingue, and N. Nagayame. A stress distribution analysis of a ceramic lunate replacement for kienbock's disease. *Journal of Hand Surgery*, 25(B):492–498, 2000.

[25] S.D. Carrigan, R.A. Whiteside, D.R. Pichora, and C.F. Small. Development of a three-dimensional finite element model for carpal load transmission in a static neutral posture. *Annals of Biomedical Engineering*, 31:718–725, 2003.

[26] K.L. Troy and M.D. Grabiner. Off-axis loads cause failure of the distal radius at lower magnitudes than axial loads:a finite element analysis. *Journal of Biomechanics*, 40:1670–1675, 2007.

[27] X. Guo, Y. Fan, and Z.M. Li. Effects of dividing the transverse carpal ligaments on the mechanical behaviour of the carpal bones under axial compressive load: A finite element study. *Medical Engineering and Physics*, 31:188–194, 2009.

[28] D.D. Anderson, B.R. Deshpande, T.E. Daniel, and M.E. Baratz. A three-dimensional finite element model of the radio-carpal joint: distal radius fracture step-off and stress transfer. *The Iowa Orthopaedic Journal*, 25:108–117, 2005.

[29] M.K. Gislason, D.H. Nash, A. Kanellopoulos, M. Bransby-Zachary, T. Hems, B. Condon, and B. Stansfield. A three-dimensional finite element model of maximal grip loading in the human wrist. *Part H: Journal of Engineering in Medicine*, 223:Artical in Press, 2009.

[30] P.L. Davidson, D.J. Chalmers, and S.C. Stephenson. Prediction of the distal radius fracture in children, using a biomechanical impact model and a case-control data on playground free falls. *Journal of Biomechanics*, 39:503–509, 2006.

[31] K.M. Degoege and J.A. Ashton-Miller. Biomechanical simulations of forward fall arrests: effects of upper extremity arrest strategy, gender and aging-related declines in muscle strength. *Journal of Biomechanics*, 36:413–420, 2003.

[32] F. Schiund, W.P. Conney, R.L. Linscheid, K.N. An, and E.Y. Chao. Force and pressure transmission through the normal wrist. a theoretical two-dimensional study in the posteroanterior plane. *Journal of Biomechanics*, 28:587–591, 1995.

[33] E. Horii, M. Garcia-Elias, K.N. An, A.T. Bishop, W.P. Cooney, R.L. Linscheid, and E.Y. Chao. Effect on force transmission across the carpus in procedures used to treat kienböck's disease. *The Journal of Hand Surgery*, 15(A):393–400, 1990.

[34] M. Majima, E. Horii, H. Matsuki, H. Hirata, and E. Genda. Load transmission trough the wrist in the extended position. *The Journal of Hand Surgery*, 33(A):182–188, 2008.

[35] W. Pistoia, B. van Reitbergen, E.M. Lochmüller, C.A. Lill, F. Ecksein, and P. Rüegsegger. Estimating of distal radius fracture load with micro-finite element analysis models based on three-dimensional peripheral quantitative computed tomography images. *Bone*, 30(6):842–848, 2002.

[36] D. Ulrich, B. van Reitbergen, A. Laib, and P. Rüegsegger. Load transfer analysis of the distal radius from in-vivo high-resolution ct-imaging. *Journal of Biomechanics*, 32:821–828, 1999.

[37] S. Pietruszczak, K. Gdela, C.E. Webber, and D. Inglis. On the assessment of brittle-elastic cortical bone fracture in the distal radius. *Engineering Fracture Mechanics*, 74:1917–1927, 2007.

[38] D. Shier, J. Bulter, and R. Lewis. *Essentials of human anatomy and physiology: Sixth Edition.* WCB McGraw-Hill, 1998.

[39] R. Tubiana, J.M Thomine, and E. Mackin. *Examination on the hand and wrist.* Dunitz Ltd., 2nd edition, 1996.

[40] C. Perry. *The encyclopedic atlas of the human body: A visual guide to the human body.* Cistol Book Publishing Pty. (Ltd.), 2004.

[41] emedicine. `http://www.emedicine.com/plastic/images/1271089-1285060-1630.jpg`, 04/02/2009.

[42] R. Schmitt, S. Froehner, G. Coblenz, and G. Christopoulos. Carpal instability. *European Radiology*, 16:2161–2178, 2006.

[43] P.L. Williams, R. Warwick, M Dyson, and L.H. Bannister. *Gray's Anatomy.* Churchhill livingstone, 1989.

[44] O.J. Lewis, R.J. Hamshere, and T.M. Bucknill. The anatomy of the wrist joint. *Journal of Anatomy*, 106(3):359–552, 1970.

[45] J.P. Razemon and G.R. Fisk. *The Wrist.* Churchill Livingstone, 1988.

[46] Joints. `http://www.sports-db.com/home/information/joints.html`, 21/03/2009.

[47] A. Freivalds. *Biomechanics of the upper limbs: mechanics, modeling and musculoskeletal injuries.* CRC Press LLC, 2004.

[48] A.D. Blevens, T.R. Light, W.S. Jablonsky, D.G. Smith, A.G. Patwardhah, M.E. Guay, and T.S. Woo. radio-carpal articular contact characteristics with scaphoid instability. *The Journal of hand surgery*, 14A (5):782–790, 1989.

[49] P. Augat, H. Iida, Y. Jiang, E. Diao, and H.K. Genant. Distal radias fractures: Mechanisms of injury and strength prediction by bone mineral assessment. *The Journal of Orthopaedic Research*, 16:629–635, 1998.

[50] Z. Földhazy, A. Arndt, C. Milgrom, A. Finestone, and I. Ekenman. Exercise-induced strain and strain rate in the distal radius. *The Journal of bone and joint surgery*, 86(B.2):261–266, 2005.

[51] T. Laurian, L. Marinc, A. Tudor, and F. Parvu. Hip joint contact pressure distribution prior to triple osteotomy. 2008.

[52] R. Jost. *Finite element simulation of the human body in vehicle side impact.* PhD thesis, University of Cape Town, 2000.

[53] A. van der Westuizen. *The strain rate dependent mechanical properties and modelling of bovine cortical bone in compression.* PhD thesis, University of Cape Town, 2008.

[54] Z. Li, J-E. Kim, J.S. Davidson, S. Etheridge, J.E. Alonso, and A.W. Eberhardt. Biomechanical responce of the pubic symphysis in lateral pelvic impacts:a finite element study. *Journal of Biomechanics*, 40:2758–2766, 2007.

[55] G. Frykman. Fracture of the distal radius including sequelae-shoulder-hand -finger syndrome: disturbance in the distal radio ulnar joint and impairment of never function. a clinical and experiential study. *Acta Orthopaedica Scandinavia*, 108:1–153, 1967.

[56] J.H. Keyak and S.A. Rossi. Prediction of femoral fracture load using the finite element models: an examination of stress- and strain- based failure theories. *Journal of Biomechanics*, 33:209–214, 2000.

[57] R. Berkow, A.J. Fletcher, and M.H. Beers. *The merck manual.* Merck Research Laboritories, 16th edition, 1992.

[58] American academy of orthopaedic surgeons. `http://orthoinfo.aaos.org/figures/A00412F02.jpg`, 17/03/2009.

[59] B.M. Nigg and W. Herzog. *Biomechanics of the Musculo-skeletal System.* John Wiley and Sons Ltd., 3rd edition, 2007.

[60] Kellogg comunity college. `http://academic.kellogg.cc.mi.us/herbrandsonc/bio201$\_$McKinley/f6-4c$\_$gross$\_$anatomy$\_$of$\_\_$c.jpg`, 16/03/2009.

[61] T.M. Keaveny and W.C. Hayes. A 20-year perspective on the mechanical properties of trabecular bone. *Journal of Biomedical Engineering*, 115:534–542, 1993.

[62] J. Homminga, B.R. Mccreadie, Ciarelli T.E., H. Weinans, S.A. Goldsein, and R. Huiskes. Cancellous bone mechanical properties from normals and patients with hip fractures differ on the structural level, not on the bone hard tissue level. *Bone*, 30 (5):759–764, 2002.

[63] R. Krone and P. Schuster. An investigation on the importance of material anisotropy in finite-element modelling of the human femur. *In SAE Internaional 2006-01-0064*, 2006-01-0064, 2006.

[64] V. Ebacher, C. Tang, H. McKay, T.R. Oxland, P. Guy, and R. Wang. Strain redistribution and cracking behaviour of human bone during bending. *Bone*, 40 (1):12651275, 2007.

[65] D.C. Wirtz, N. Schiffers, T. Pandorf, K. Randermacher, D. Weichert, and R. Forst. Critical evaluation of known bone material properties to realize anisotropic fe-simulation of the proximal femur. *Journal of Biomechanics*, 33:1325–1330, 2000.

[66] J.Y. Rho, M.C. Hobatho, and R.B. Ashman. Relations of mechanical properties to density and ct numbers in human bone. *Medical Engineering & Physics* , 17:347–355, 1995.

[67] A.C. Ugural. *Advanced strength and applied elasticity.* Pearson Education, 4th edition, 2003.

[68] S. Higgins. Strain rate and density dependent behaviour of bovine cancellous bone in compression. Master's thesis, University of Cape Town, 2008.

[69] J.L. McElhaney. Dynamic response of bone and muscle tissue. *Journal of Applied Physiology*, 21 (4):1231–1236, 1966.

[70] K.L. Troy and M.D. Grabiner. Development and validation of a finite element model to simulate colles's fractures. In *52nd Annual Meeting of the Orthopaedic Research Society*. 2005.

[71] J.T-M. Cheung, M. Zhang, A. K-L. Leung, and Y-B. Fan. Three-dimensional finite element analysis of the foot during standing- a material sensitivity study. *Journal of Biomechanics*, 38:1045–1054, 2005.

[72] A.T.M Philips, P. Pankaj, C.R. Howie, A.S. Usmani, and A.H.R.W. Simpson. Finite element modelling of the pelvis:inclusion of muscular and ligamentous boundary conditions. *Medical Engineering and Physics*, 29:739–748, 2007.

[73] S. Majumder, A. Roychowdhury, and S. Pal. Effects of trochanteric soft tissue thickness and hip impact velocity on hip fracture in sideways fall through 3d finite element simulations. *Journal of Biomechanics*, 41:2834–2842, 2008.

[74] Q.H. Zhang and E.C. Teo. Finite element application in implant research for treatment of lumbar degenerative disc disease. *Medical Engineering and Physics*, 30:1246–1256, 2008.

[75] M.R. Bosisio, M. Talmant, W. Skalli, P. Laugier, and D. Mitton. Apparent young's modulus of human radius using inverse finite element method. *Journal of Biomechanics*, 40:2022–2028, 2007.

[76] A.J. Kerin, M.R. Wisnom, and M.A. Adams. The compression strength of articular cartilage. *IMechE*, 212H:273–280, 1998.

[77] C.G. Armstrong and V.C. Mow. Variations in the intrinsic mechanical properties of human articular cartilage with age, degeneration and water content. *The Journal of Bone and Joint Surgery*, 40 (1):12651275, 1982.

[78] S. Park, C.T. Hung, and G.A. Ateshian. Mechanical responce of bovine articular cartilage under dynamic unconfined compression loading at physiological stress levels. *Osteoarthritis and cartilage*, 12:65–73, 2004.

[79] J.Z. Wu, W. Herzog, and M. Epstein. Evaluation of the finite element software abaqus for biomechanical modelling of biphasic tissue. *Journal of Biomechanical*, 31:165–169, 1998.

[80] C.P. Brown, T.C. Nguyen, H.R. Moody, R.W. Crawford, and A. Oloyede. Assessment of common hyperelastic constitutive equations for describing normal and osteoarthrritic articular cartilage. *Part H: Journal of Engineering in Medicine*, 223:1–10, 2009.

[81] W. Pistoia, B. van Rietbergen, E.M. Lockmüller, C.A. Lill, F. Eckstein, and P. Ruegsegger. Estimation of the distal radius failure load with micro-finite element analysis models based on three-dimensional peripheral quantitative computer tomography images. *Bone*, 30:842–848, 2002.

[82] G. Li, O. Lopez, and H. Rubash. Variability of a three-dimensional finite element model constructed using magnetic resonance images of a knee for joint contact stress analysis. *Journal of Biomechanical Engineering*, 123:341–346, 2001.

[83] S.E. Nowalk, M.D.and Logan. Distinguishing biomenchanical properties of intrinsicand extrinsic human wrist ligaments. *Journal of Biomechanical Engineering*, 113:85–93, 1991.

[84] S. Fischli. Simulation of wrist kinematics on the basis of a rigid body spring model. Master's thesis, Queens University,Canada, 2007.

[85] J.J. Crisco, J.C. Coburn, D.C. Moore, and M.A. Upal. Carpal bone size and scaling in men versus women. *The Journal of Hand Surgery*, 30A:35–42, 2005.

[86] Dassault Systemes Simulia Corp, Providence, USA. *Abaqus analysis users manual*, 6.8 edition, 2008.

[87] S.F. Veigas, R. Patterson, P. Peterson, J. Roefs, A. Tencer, and S. Choi. The effect of various load paths and different loads transfer characteristics of the wrist. *The Journal of Hand Surgery*, 14A:458–465, 1989.

[88] L. Teurlings, G.L. Miller, and T.W. Wright. Pressure mapping of the radioulnar carpal joint: effects of ulna lengthening and wrist position. *The Journal of hand surgery*, 25B:346–349, 2000.

[89] E.J. Hearn. *Mechanics of materials. 2nd Edition.* Butterworth Heinemann, 2nd edition, 1996.

Appendix A

Wrist bone geometry

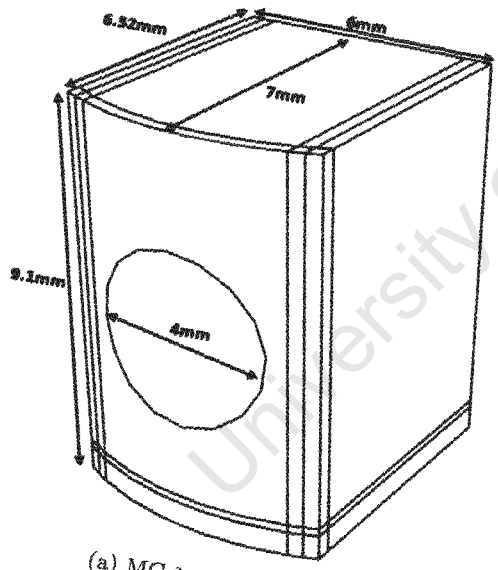

(a) MC 1, 2, 4, 5

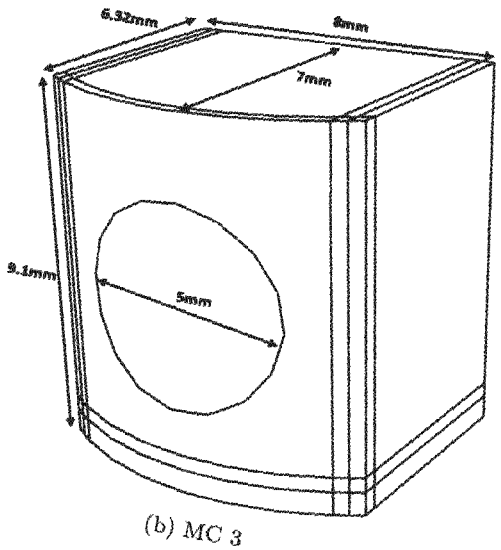

(b) MC 3

Figure A.1: Metacarpal geometry.

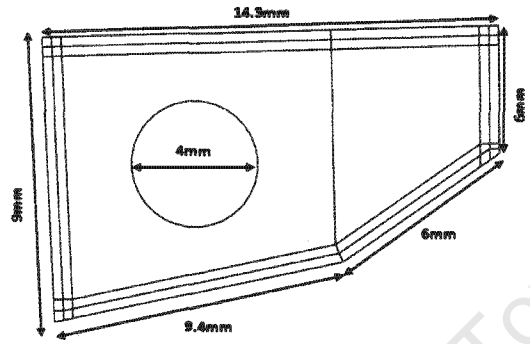

(a) Capitate

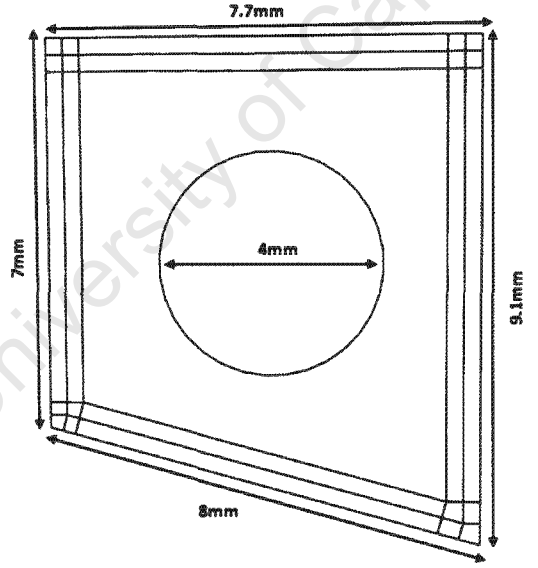

(b) Hamate

Figure A.2: Carpal geometry, thickness=7mm.

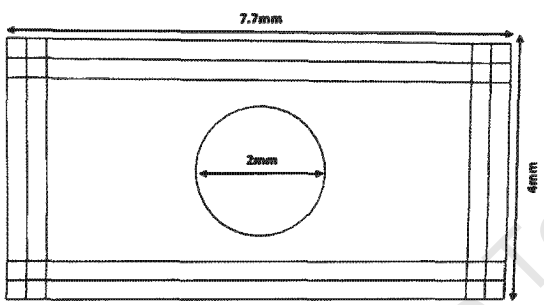

(a) Trapezium/Trapezoid

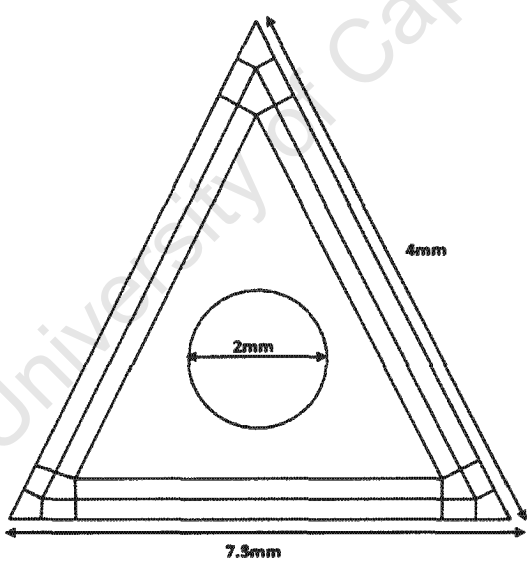

(b) Triquetrum

Figure A.3: Carpal geometry, thickness = 7mm.

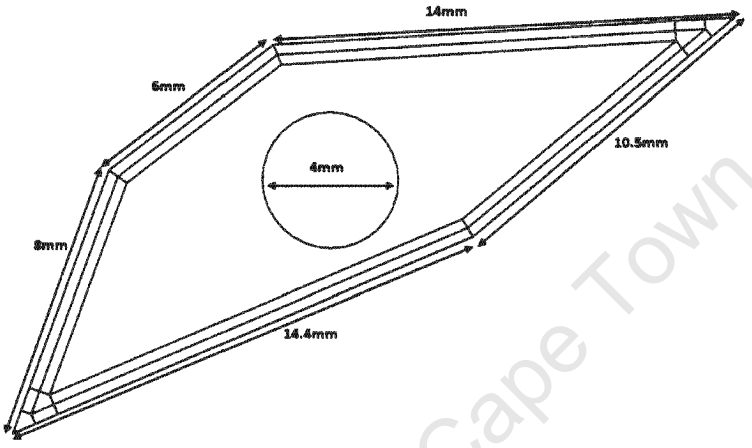

(a) Scaphoid

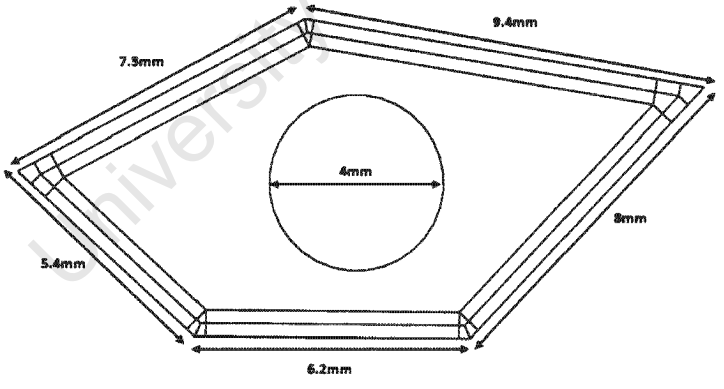

(b) Lunate

Figure A.4: Carpal geometry, thickness=7mm.

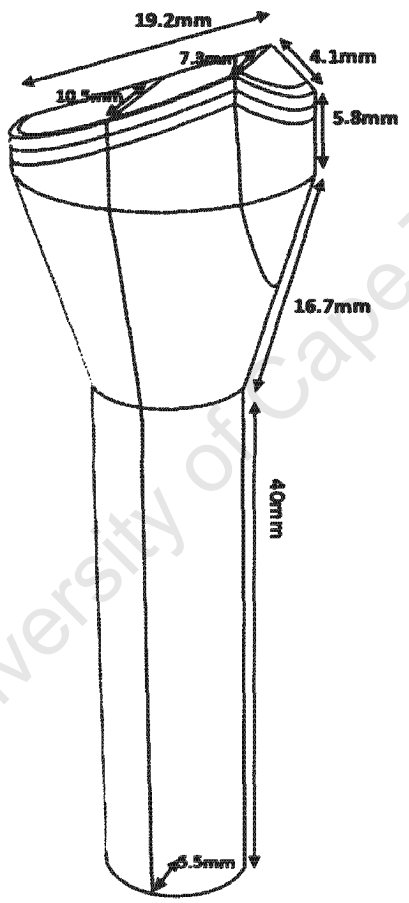

Figure A.5: Geometry of the radius.

Bone	Average volume[85] (mm^3)	Measured volume (mm^3)
Scaphoid	2390.1±673.6	2809
Lunate	1810.1±578.5	1608

Table A.1: Comparison of scaphoid and lunate volumes to average volume values from Crisco et al.[85].

Appendix B

Bone mesh

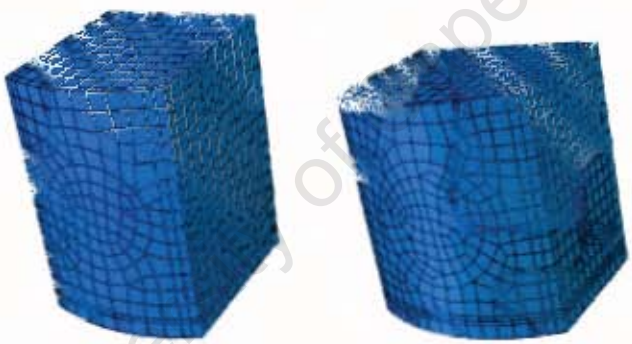

(a) MC 1, 2, 4, 5 (b) MC 3

Figure B.1: Meshed metacarpals.

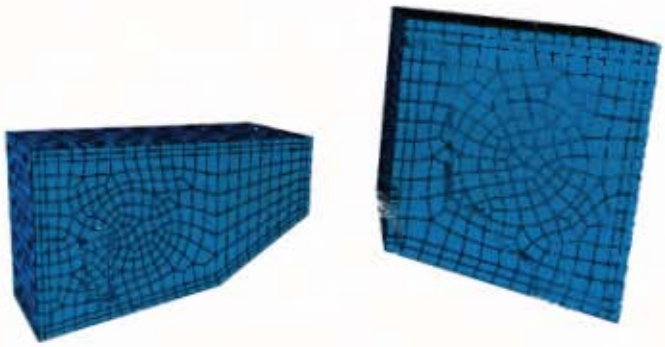

(a) Capitate (b) Hamate

Figure B.2: Meshed carpal bones.

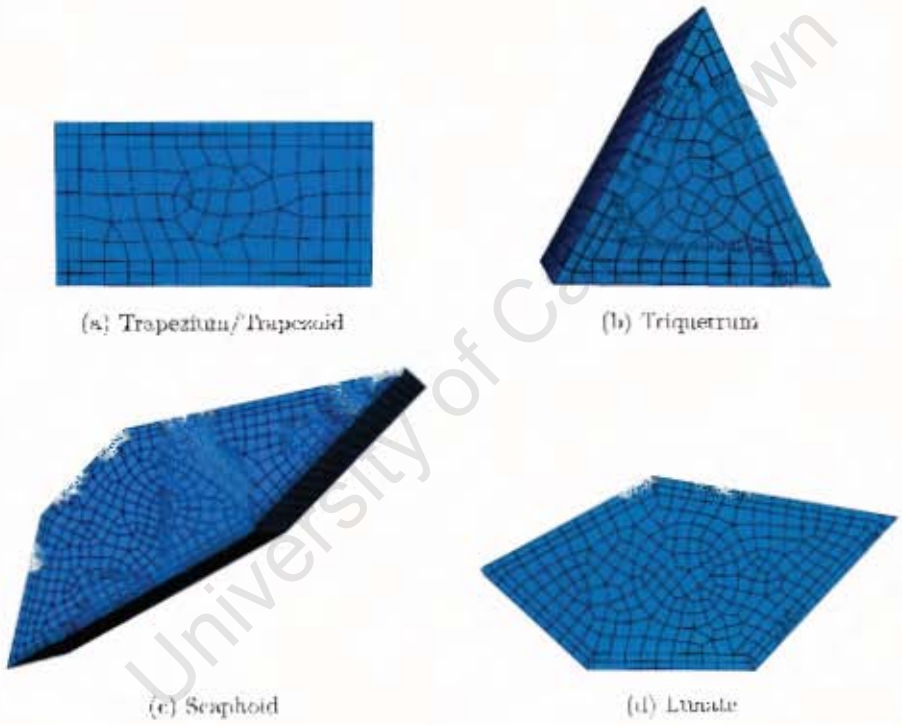

(a) Trapezium/Trapezoid (b) Triquerrum

(c) Scaphoid (d) Lunate

Figure B.3: Meshed carpal bones.

Figure B.4: Meshed Radius.

Appendix C

Simulation results

This appendix contains the simulation results of the GSM and the ABGM. The results are presented in the form of tables.

C.1 Material property parameter variation results

Name	Young's Modulus (MPa)	von Mises Stress (MPa)	Max Principal Stress (MPa)	Contact Pressure (MPa)	Contact Area (mm^2)
Cort-1	5.70	16.70	10.86	1.33	86.28
Cort-2	7.30	16.80	10.89	1.33	84.29
Cort-3	10.00	17.60	10.93	1.33	83.64
Cort-4	13.80	19.50	10.96	1.33	80.96
Cort-5	15.00	19.90	10.96	1.33	80.69
Cort-6	18.00	20.80	10.98	1.33	80.09
Cort-7	20.70	21.50	10.99	1.33	79.50
Cort-8	22.70	21.90	11.00	1.33	79.50

Table C.1: Cortical bone material parameters and model maximum stress values.

Name	Young's Modulus (MPa)	Poisson's Ratio	von Mises Stress (MPa)	Maximum Principal Stress (MPa)	Contact Pressure (MPa)	Contact Area (mm^2)
cart1	3.50	0.05	19.360	10.770	1.030	239.700
cart2	3.50	0.15	19.390	10.790	1.016	239.289
cart3	3.50	0.20	19.410	10.790	1.000	240.968
cart4	3.50	0.25	19.430	10.800	0.978	240.822
cart5	3.50	0.30	19.410	10.790	0.970	238.550
cart6	3.50	0.35	19.520	10.830	0.903	240.356
cart7	3.50	0.45	19.670	10.890	0.830	239.163
cart8	3.50	0.49	19.780	10.920	0.961	214.480
cart8	3.50	0.49	19.780	10.920	0.961	214.480
cart9	4.00	0.49	19.760	10.900	0.972	214.248
cart10	5.00	0.49	19.800	10.940	0.992	205.660
cart11	7.50	0.49	19.840	10.950	1.020	194.168
cart12	10.00	0.49	19.860	10.950	1.030	191.200
cart13	30.00	0.49	19.890	10.960	1.200	168.320
cart14	48.00	0.49	19.900	10.960	1.330	161.200
cart15	100.00	0.49	19.900	10.960	1.600	157.622
cart16	500.00	0.49	19.900	10.970	2.730	142.020

Table C.2: Cartilage linear elastic material parameters and model maximum stress values.

Name	C1 (MPa)	C2 (MPa)	von Mises Stress (MPa)	Maximum Principal Stress (MPa)	Contact Pressure (MPa)	Cartilage stress at 30% strain (MPa)
hyper1	4.1	0.41	60.210	30.700	5.000	12.565
hyper2	6.15	0.615	60.700	31.000	5.000	18.848
hyper3	10.25	1.025	61.090	31.240	5.335	31.413
hyper4	14.35	1.435	61.260	31.340	5.516	43.979
hyper5	45.1	4.51	61.570	31.530	7.111	138.219

Table C.3: Cartilage hyperelastic material parameters and model maximum stress values.

Name	Young's Modulus (MPa)	Poisson's Ratio	von Mises Stress (MPa)	Maximum Principal Stress (MPa)	Contact Pressure (MPa)	Contact Area (mm^2)
can-1	0.10	0.20	67.10	38.30	2.11	69.45
can-2	0.15	0.20	59.50	33.90	1.95	73.55
can-3	0.35	0.20	42.50	23.80	1.63	79.55
can-4	0.69	0.20	29.70	15.70	1.40	78.00
can-5	1.40	0.20	28.40	12.30	1.33	76.70
can-6	1.40	0.3	28.30	12.30	1.33	76.69

Table C.4: Cancellous bone material parameters and model maximum stress values.

C.2 Geometrically Simplified Model parameter variation results

Load (N)	Contact Pressure (MPa)					
Model	**1**	**2**	**3**	**4**	**5**	**6**
(N)	(Mpa)	(Mpa)	(Mpa)	(Mpa)	(Mpa)	(Mpa)
50	1.002	0.8828	0.8576	0.678	1.637	0.9733
100	1.775	1.793	1.465	1.304	2.612	1.811
140	2.618	2.317	2.273	1.692	3.751	2.631
200	3.891	3.191	2.935	2.362	6.164	3.464
300	5.252	4.73	4.755	3.589	8.71	5.016
400	6.677	6.323	6.06	4.912	10.09	6.66

Table C.5: Contact pressures at different loads applied to the metacarpals for models 1-6.

Applied Load (N)	Radio-lunate Displacement (mm) and Load (N)											
Model	**1**		**2**		**3**		**4**		**5**		**6**	
	(mm)	(N)	(mm)	(N)	(mm)	(N)	(mm)	(N)	(mm)	(N)	(mm)	(N)
50	0.18	3.27	0.06	4.84	0.20	3.66	0.07	5.29	0.14	1.84	0.23	4.65
100	0.29	7.19	0.13	9.46	0.32	8.25	0.14	10.57	0.21	4.13	0.34	9.21
140	0.38	11.23	0.19	13.92	0.39	12.07	0.20	14.70	0.29	6.88	0.42	13.57
200	0.49	17.34	0.27	20.29	0.50	18.36	0.28	21.20	0.39	11.57	0.53	19.70
300	0.62	24.86	0.38	28.26	0.68	28.63	0.43	32.09	0.51	18.55	0.66	27.16
400	0.73	32.00	0.48	35.71	0.84	39.82	0.57	43.07	0.62	25.24	0.76	34.24

Table C.6: Load and displacement values for the Radio-lunate ligament at different loads applied to the metacarpals for models 1-6.

Model	Maximum contact pressure on Radius		
	Scaphoid fossa (MPa)	Lunate fossa (MPa)	S/L
Load applied to the metacarpals=140N			
1	2.2	1.02	2.15
2	2.13	0.88	2.41
3	1.97	1.16	1.70
4	1.69	1.02	1.66
5	2.15	2.52	0.90
6	2.17	1.22	1.78
Load applied to the metacarpals=300N			
1	4.63	2.26	2.05
2	4.07	2.84	1.43
3	3.96	2.84	1.4
4	3.46	2.4	1.44
5	4.57	8.67	0.53
6	4.31	2.31	1.86

Table C.7: Maximum contact pressure values for the articular surface of the radius at different loads applied to the metacarpals for models 1-6.

Applied Load (N)	Contact area ratio's											
Model	**1**		**2**		**3**		**4**		**5**		**6**	
	S/L	Total/Joint	S/L	Total/Joint	S/L	Total/Joint	S/L	Total/Joint	S/L	Total/Joint	S/L	Total/Joint
50	2.36	0.39	2.19	0.39	1.91	0.34	2.59	0.44	2.21	0.23	1.63	0.30
100	2.54	0.39	2.33	0.40	1.91	0.34	2.59	0.44	2.24	0.25	1.83	0.31
140	2.74	0.40	2.45	0.41	2.00	0.33	2.64	0.43	2.16	0.28	2.03	0.32
200	2.91	0.40	2.63	0.41	2.12	0.34	2.71	0.43	2.03	0.28	2.23	0.33
300	3.20	0.41	2.77	0.41	2.23	0.33	2.85	0.44	2.04	0.30	2.52	0.34
400	3.41	0.41	3.01	0.42	2.50	0.34	3.09	0.44	2.24	0.31	2.77	0.34

Table C.8: Contact area ratios for scaphoid-radius and lunate-radius articulation on the radius articular surface at different loads applied to the metacarpals for models 1-6.

Applied Load (N)	Contact area ratio's											
Model	**1**		**2**		**3**		**4**		**5**		**6**	
Load	Scaphoid	Lunate	Scaphoid	Lunate	Scaphoid	Lunate	Scaphoid	Lunate	Scaphoid	Lunate	Scaphoid	Lunate
50	117.32	49.76	115.84	52.90	95.15	49.79	135.33	52.27	68.89	31.21	79.65	48.80
100	120.80	47.64	120.33	51.70	95.15	49.79	135.33	52.27	74.59	33.33	85.96	46.88
140	126.37	46.15	123.49	50.37	95.05	47.54	134.76	51.02	81.26	37.70	91.94	45.37
200	128.55	44.16	128.38	48.73	97.86	46.22	135.65	50.04	81.68	40.23	96.65	43.41
300	133.94	41.81	129.84	46.92	98.69	44.30	138.32	48.52	85.90	42.15	103.13	40.99
400	135.50	39.69	135.43	45.07	103.27	41.31	142.25	45.97	91.12	40.65	108.30	39.10

Table C.9: Contact area for scaphoid-radius and lunate-radius articulation on the radius articular surface at different loads applied to the metacarpals for models 1-6.

C.3 Accurate Bone Geometry Model variation results

Load (N)	Contact Pressure (MPa)	
Model	**7**	**8**
(N)	(Mpa)	(Mpa)
100	2.875	2.862
140	3.34	3.475
200	4.09	4.226
300	5.403	6.014

Table C.10: Contact pressures at different loads applied to the metacarpals for models 7 & 8.

Model	Maximum contact pressure on Radius		
	Scaphoid fossa (MPa)	Lunate fossa (MPa)	S/L
Load applied to the metacarpals=140N			
7	3.23	2.14	1.51
8	3.07	1.94	1.60
Load applied to the metacarpals=300N			
7	5.33	4.63	1.15
8	5.67	4.26	1.33

Table C.11: Maximum contact pressure on the radius articular surface at different loads applied to the metacarpals for models 7 & 8.

Applied Load (N)	Contact area ratio's			
Model	**7**		**8**	
	S/L	Total/Joint	S/L	Total/Joint
100	1.12	0.36	1.11	0.35
140	1.14	0.36	1.12	0.36
200	1.15	0.37	1.12	0.36
300	1.19	0.37	1.13	0.37

Table C.12: Contact area ratios for scaphoid-radius and lunate-radius articulation on the radius articular surface at different loads applied to the metacarpals for models 7 & 8.

Applied Load (N)	Contact area's			
Model	**1**		**2**	
Load	Scaphoid	Lunate	Scaphoid	Lunate
100	244.39	217.94	239.23	214.69
140	248.86	218.85	242.56	217.24
200	251.46	218.61	246.36	219.35
300	254.90	214.64	250.96	222.67

Table C.13: Contact area for scaphoid-radius and lunate-radius articulation on the radius articular surface at different loads applied to the metacarpals for models 7 and 8.

Ligament attachment		Model 7				Model 8				Ligament force at $\varepsilon = 3\%$
		Ligament Tensile load (N)		Percentage of 140N load applied (%)		Ligament Tensile load (N)		Percentage of 140N load applied (%)		
Bone1	Bone2	Dorsal	Palmer	Dorsal	Palmer	Dorsal	Palmer	Dorsal	Palmer	Both
Radius	Scaphoid	3.98	6.04	2.85	4.32	0.16	7.87	0.11	5.62	1.49
Lunate	Scaphoid	59.77	6.44	42.69	4.60	73.88	29.91	52.77	21.36	8.36
Lunate	Triquetrum	41.38	1.54	29.56	1.10	71.46	1.84	51.05	1.31	16.61
Capitate	Scaphoid	6.02	13.57	4.30	9.69	0.73	13.58	0.52	9.70	3.18
Capitate	Triquetrum	2.76	2.68	1.97	1.91	38.23	21.57	27.30	15.41	17.61
Capitate	Hamate	19.08	1.72	13.63	1.23	39.87	11.10	28.48	7.93	27.36
Capitate	Trapezium	0.42	0.33	0.30	0.24	2.59	3.70	1.85	2.64	40.06
Scaphoid	Trapezium	25.35	50.35	18.11	35.97	35.25	20.40	25.18	14.57	6.62
Scaphoid	Trapezoid	43.61	1.03	31.15	0.74	7.06	10.57	5.04	7.55	6.62
Triquetrum	Hamate	221.39	205.67	158.14	146.91	90.78	63.67	64.84	45.48	11.26
Lunate	Hamate	77.71	132.24	55.51	94.46	99.30	120.94	70.93	86.39	12.26
Lunate	Capitate	7.16	29.43	5.11	21.02	11.72	7.36	8.37	5.26	12.14
Capitate	Trapezoid	0.59	48.31	0.42	34.51	3.05	28.70	2.18	20.50	12.58
Trapezoid	Trapezium	1.11	5.54	0.80	3.96	37.15	16.37	26.53	11.69	9.11
Lunate	Radius	37.93	75.34	27.10	53.81	51.29	67.03	36.64	47.88	9.77

Table C.14: Ligament load when a 140N load is applied to the metacarpals for models 7 and 8.

C.4 Comparison between the Geometrically Simplified and the Accurate Bone Geometry Model results

Load(N)	100			200		
Model	Exp(avg)	M1	M7	Exp(avg)	M1	M7
Contact Pressure(Mpa)	1.62	1.78	2.88	2.84	3.89	4.09
Contact area/total joint area	0.18	0.39	0.36	0.22	0.40	0.37
von Mises Stress(Mpa)	-	28.57	38.67	-	59.71	72.05
Maximum Principal Stress(Mpa)	-	17.50	17.39	-	33.73	32.56
Minimum Principal Stress(Mpa)	-	1.50	5.20	-	2.91	9.78
Hydrostatic Stress(Mpa)	-	13.52	41.64	-	28.26	77.50

Table C.15: A comparison of Model 1 and 7 results. Exp(avg) is the average experimental value from Veigas et al. [18, 87]

Appendix D

Volunteer's CT scan details

Computer tomography (CT) images of the left wrist joint were acquired from the Department of Radiology at the Groote Schuur hospital. The scan was conducted on a forty year old mixed race male volunteer. The images present within the data set were from the distal portion of the radius to the proximal portions of the metacarpals. A slice of the volunteer's CT scan is shown in figure D.1.

Figure D.1: A slice of the CT scan used for image processing.